NSK Technical Journal

Motion & Control

No. 33 June 2022

ISSN1342-3630

NSK

MOTION & CONTROL No. 33
NSK Technical Journal
Printed and Published: June 2022
ISSN1342-3630
Publisher: NSK Ltd., Ohsaki, Shinagawa, Tokyo, JAPAN
Public Relations Department
TEL +81-3-3779-7050
FAX +81-3-3779-7431
Editor: Nobuaki MITAMURA
Managing Editor: Aya OKAMOTO
Design, Typesetting & Printing: Kuge Printing Co., Ltd.

NSK Technical Journal
Motion & Control
No. 33
June 2022

NSK

Contents

Technical Papers

New Products

Ball Screw Technologies to Control Machine Tool Quadrant Glitches

Hirose Toshiro
Industrial Machinery Technology Center, Linear Technology Center, BS Department
Ueda Masahiro
NSK Deutschland GmbH
Oshikawa Keigo
Industrial Machinery Technology Center, Linear Technology Center, Research Department

Abstract

In the machine tool industry, efficiency, automation, and precision have become trends against the backdrop of labor shortages and diversifying processing needs. Furthermore, in recent years, environmental initiatives have become an important issue.

In this article, we will explore recent patterns in machine tool technologies based on trends at machine tool exhibitions. Then we will shift our focus to the motion errors called quadrant glitches (reversal spikes), which cause streaks on the workpiece surface, and the technologies to control these glitches. Machine tools with ball screws featuring this technology achieve higher quality surface finishes and increase productivity by reducing the time required for surface finishing.

1. Foreword

In recent years, the machine tool industry has been changing due to factors such as the global labor shortage, changing working environments, and shifts in the automobile industry as symbolized by CASE and MaaS, as well as the digitization accelerated by the advancement of 5G, IoT, and AI. Furthermore, there is increased concern about environmental issues, so manufacturing while considering the global environment has become widespread, with aims to achieve a more sustainable society.

Against this backdrop, we are required to promote innovation in the manufacturing industry while flexibly responding to significant changes in the environment. We also need to develop ball screws, which are important machine element parts of machine tools, by pursuing further added value.

This article describes the technological trends of machine tools in recent years and introduces the technology for suppressing quadrant glitches, which we have developed in order to improve the functionality of ball screws.

2. Technological Trends of Machine Tools

Since 1996, NSK has been investigating machine tools exhibited at the Japan International Machine Tool Fair (JIMTOF). Here, according to the previous investigation results of the JIMTOF exhibited machines, we will describe the latest technological trends of feed drive systems and the functions they require.

2.1 Trends of the feed drive systems in machine tools

Figure 1 shows a comparison of the number of units with the rapid traverse speed of the machining center exhibited at JIMTOF. Partly due to the influence of an online event in 2020, the number of units investigated was 84. Compared to 2018, it has decreased to 70%. Figure 2 shows the number of units in Figure 1 converted into percentages. It shows that, although there was a slight increase of 60 to 80 m/min in 2020, there was no change in general, and the speed reached a plateau at 60 to 80 m/min.

Figure 3 shows the results of investigating a guideway type of machining center. Since 1996, when the investigation started, the rate of adoption of rollers has been increasing year by year, reaching 60% in 2020.

Rollers are characterized by high load capacity and high rigidity, suggesting that such needs are increasing in the guidance of machining centers.

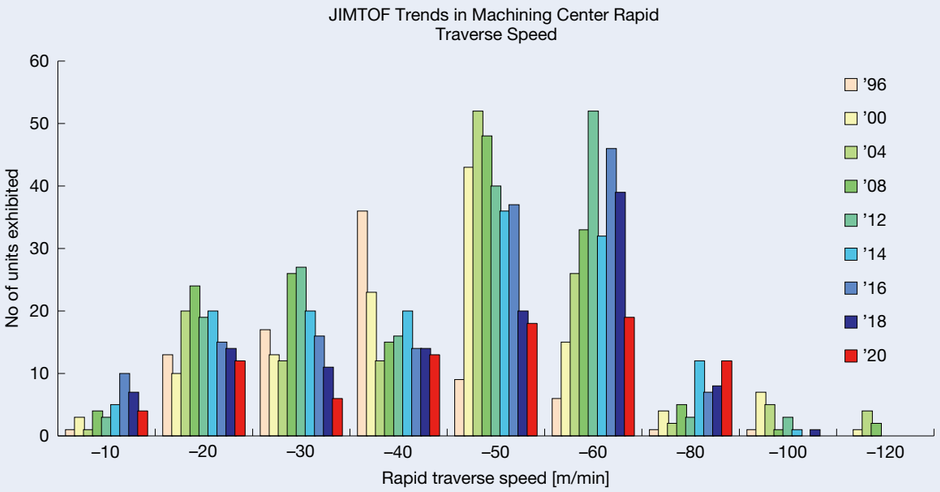

Fig. 1 JIMTOF trends in machining center rapid traverse speed

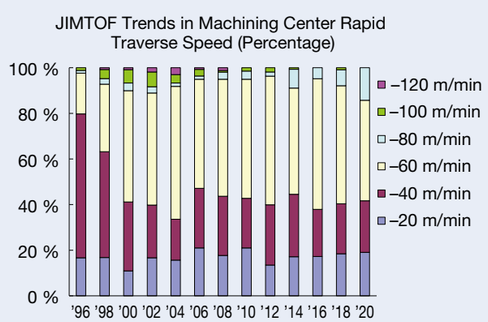

Fig. 2 JIMTOF trends in machining center rapid traverse speed (percentage)

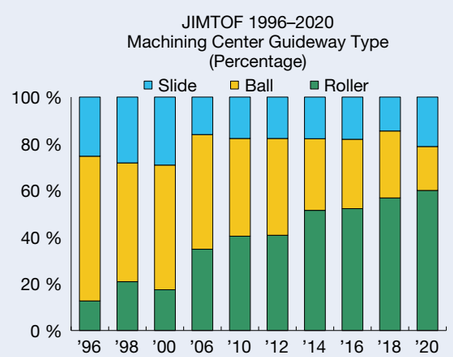

Fig. 3 JIMTOF trends in machining center guideway type (percentage)

2.2 Functions required for the feed drive systems of machine tools

Figure 4 shows the appeal points read from the website and catalog for the machine tools exhibited at JIMTOF2020 Online. Based on recent changes in the manufacturing industry, represented by the SDGs, CASE, 5G communications, etc., we have classified the appeal points into four categories from NSK's unique perspective.

(1) Efficiency Improvement mainly focuses on shortening the lead time during machining, machining difficult-to-cut materials, and improving the efficiency of high-mix low-volume production. (2) Automation includes simplicity that does not rely solely on labor saving or the intuition or expertise of skilled workers. (3) Accuracy Improvement includes stable machining accuracy and high-quality machined surfaces. And (4) Digital Transformation includes sensing technology and AI/digital twin technology. In addition, a concept exhibition on environmental property was held.

To realize these four appeal points of recent machine tools, the feed drive systems are required to have five functions: A. heavy cutting, B. composite machining/speeding up, C. long-term stable operation, D. high-quality machined surfaces, and E. monitoring and diagnosis as shown in Figure 5. Furthermore, when these functions are applied to ball screws, an element of feed drive systems, improved load capacity (A/B), size reduction (B), high speed and low noise (B), life extension (C), little to no maintenance (C), stabilization and reduction of quadrant glitches (D), low heat generation (D), and condition monitoring (E) are necessary.

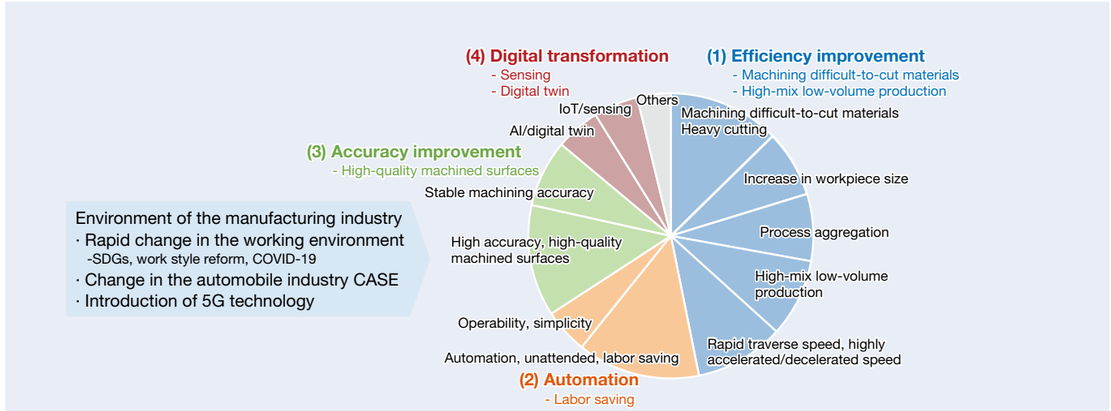

Fig. 4 Selling points for machine tools

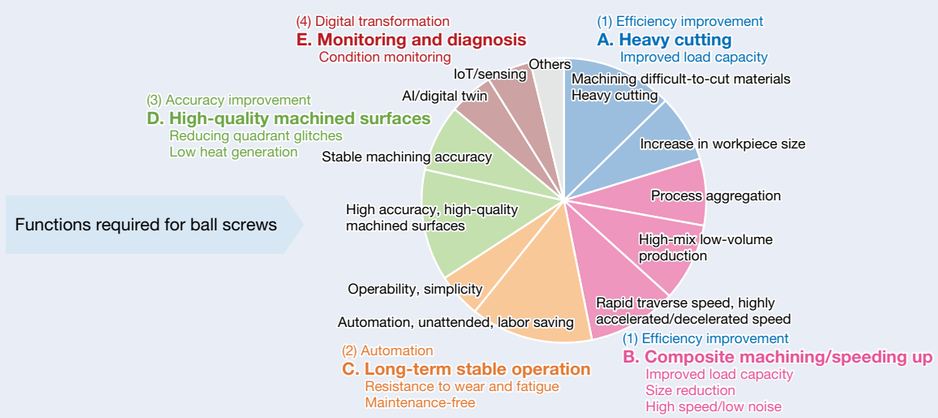

Fig. 5 Five functions required for precision feed drive systems and ball screws

NSK has developed many of the ball screws on the market with the aim of achieving these diversifying functional requirements. Figure 6 shows part of this. As a response to B. composite machining/speeding up, we provide high-speed low-noise ball screws that are compact and make little noise even during high-speed operation, while as a response to A. heavy cutting and D. high-quality machined surfaces, we provide nut cooling ball screws that suppress temperature rise and achieve high accuracy. Also, as a response to D. high-quality machined surfaces, we provide high-performance precision ball screws to which quadrant glitches stabilization technology (described later in Section 3.1) are applied, and we offer high-durability precision ball screws that achieve C. long-term stable operation by suppressing wear under harsh continuous operating conditions.

The next chapter explains the latest technology for ball screws, which suppresses motion errors called quadrant glitches and improves the quality of the machined surface.

3. Technology for Ball Screws that Suppresses Quadrant Glitches

Generally, machining centers for machining molds and electrical discharge machines are required to have a technology for machining high-precision and high-quality surface shapes. Since high-motion accuracy is necessary for these feed drive systems, high precision ball screws are often used. For example, we perform end mill tool circular interpolation machining by arranging ball screws on two orthogonal axes to perform circular interpolation motion as shown in Figure 7. When quadrants of the circular motion trajectory are switched in the circular interpolation motion, the drive direction of one of the two ball screws arranged on the two orthogonal axes is reversed. At this time, the friction characteristics of ball screws change abruptly, so even if the position is controlled by sequentially feeding back signals from a linear scale or the like, circular motion trajectory errors called “quadrant glitches” occur when quadrants of circular interpolation motion are switched[1]. Due to this quadrant protrusion, a streak-like pattern appears on the machined surface and causes deterioration of the quality of the machined surface of a mold. Therefore, machining centers and the like generally perform correction of quadrant glitches by preparing the function of a control compensator that can create a signal to correct quadrant glitches when identifying a system[2].

However, the friction characteristics of ball screws used in the feed drive systems change and fluctuate depending on the specifications and position of the nut because the screw shaft is long. This makes it difficult to set the control parameters when identifying the system, which has been a problem in making sufficient corrections. In response, NSK has developed a technology to make the height of quadrant glitches uniform by suppressing the fluctuation in the friction torque of ball screws at the nut position on the screw shaft[2]. In addition, we developed a new technology that eliminates the generation of quadrant glitches on the second peak, which was previously hard to correct even with a control compensator, and reduces the height of quadrant glitches on the first peak. We will introduce this technology along with a conventional homogenization technology.

Fig. 6 NSK ball screws for machine tools

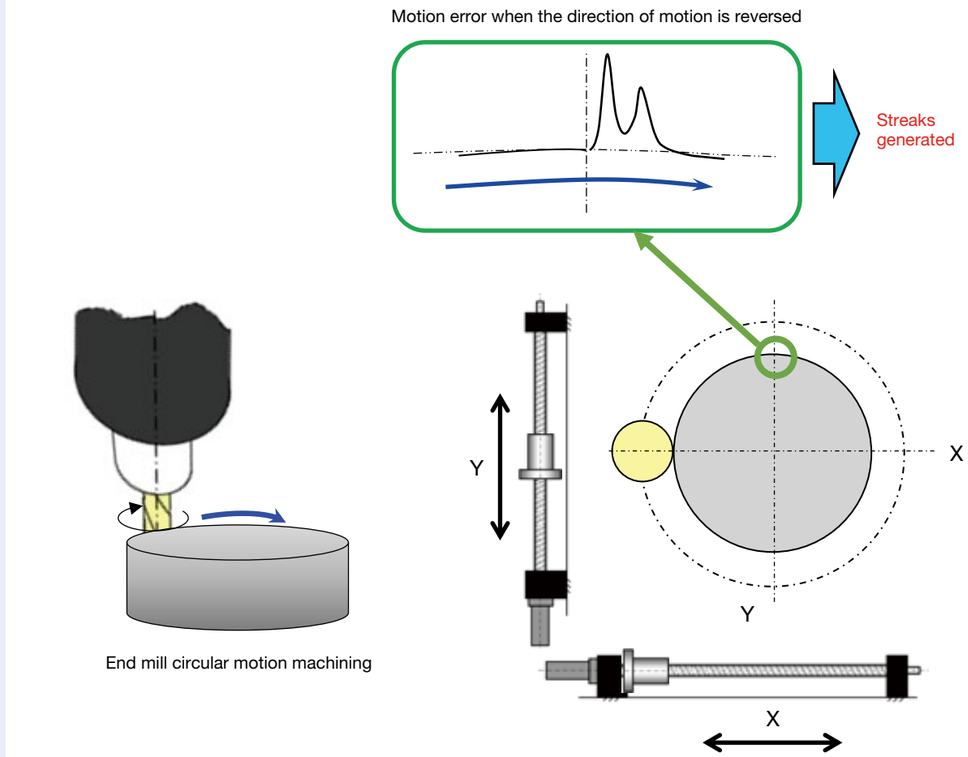

Fig. 7 Occurrence of quadrant glitches in circular interpolation motion with two orthogonally oriented axes

3.1 Quadrant glitches homogenization technology

Even in ball screws used for high-precision machine tools such as machining centers and electric discharge machines, the friction torque fluctuates slightly depending on the nut position due to slight machining errors on long screw shafts. Therefore, according to the requirement for machining accuracy of machine tools, a fluctuation range standard is strictly set depending on the accuracy grade of ball screws and length of screw shafts. In order to support machine tools that achieve machining accuracy from submicron to several tens of nanometers, which exceeds the conventional machining accuracy, a slight fluctuation in the friction torque of ball screws was a technical issue for us.

In the homogenization technology for the friction torque, development of NSK's original production technology has reduced a fluctuation range of the friction torque by up to 30% compared to the conventional specifications with the same accuracy grade and stroke length.

Figure 8 shows the results of comparing the occurrence heights of quadrant glitches between the conventional specifications and the specifications with quadrant glitches homogenization technology. The ball screw has a shaft diameter of 40 mm and lead of 12 mm. Here, at each stroke position of –50 mm, 0 mm, and 50 mm, a circular interpolation motion with a feed rate of 480 mm/min and an arc radius of 10 mm was given as a command value. In the circular interpolation motion, the motion direction is reversed twice per lap. Therefore, looking at Figure 8, motion errors called quadrant glitches occur at two locations under all conditions. In addition, Figure 8 shows that the peak height of quadrant glitches changes depending on the stroke position in a conventional ball screw, whereas the peak height of quadrant glitches does not change at any stroke position in a ball screw with technology that reduces quadrant glitches. This allows for uniform corrections regardless of the stroke position where the system is identified, and an effect of obtaining high contour accuracy in the circular interpolation motion can be expected.

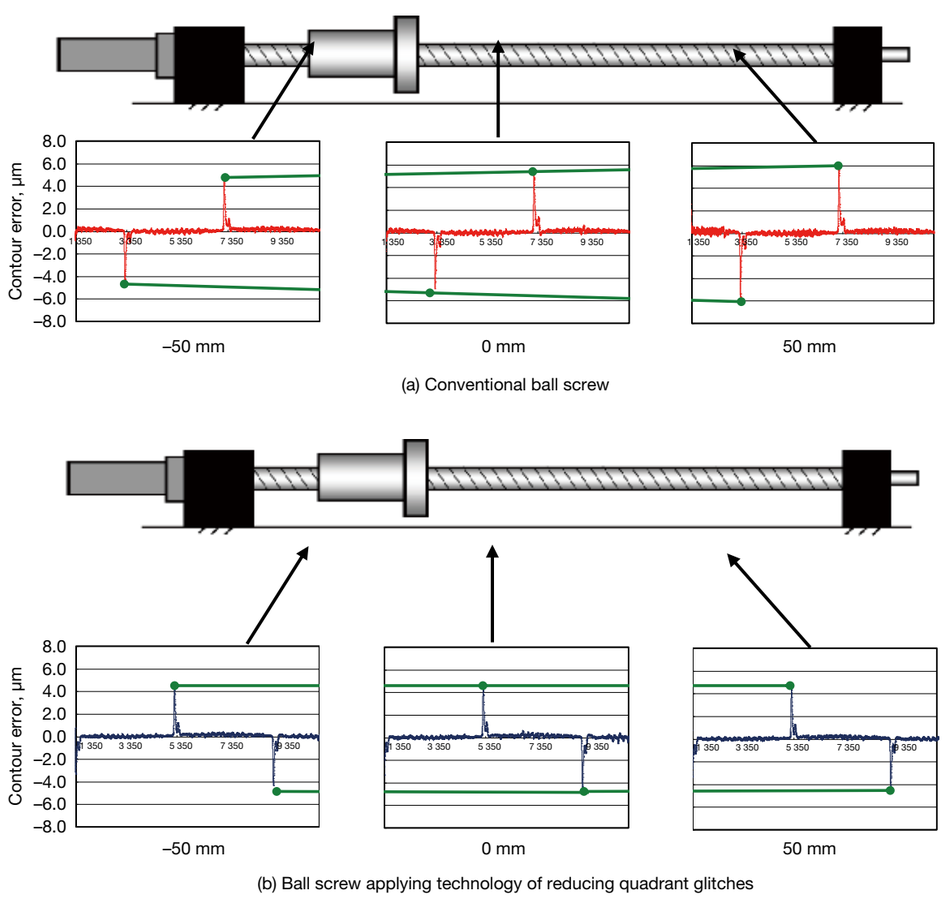

(a) Conventional ball screw

(b) Ball screw applying technology of reducing quadrant glitches

Fig. 8 Circular interpolation errors by time

3.2 Technology for reducing quadrant glitches

Next, we will introduce the shapes of quadrant glitches caused by the preload system of ball screws and the technology for reducing the glitches. The gothic arc shape is generally adopted for the groove shape of ball screws, and the preload system is roughly divided into two types.

The first type is an oversized ball preload system, in which a steel ball the size of several microns larger than a gothic arc groove space provided in the screw shaft and nut is inserted, and the steel ball and the gothic arc groove come into contact at four points. The second type is an offset preload system, in which a steel ball and a gothic arc groove come into contact at two points by relatively offsetting the screw groove position of the shaft and nut in the axial direction. Previous studies have revealed that these two preload systems change the shape of quadrant glitches. Specifically, it is known that the oversized ball preload system generates one peak in quadrant glitches, whereas the offset preload system generates two peaks[3, 4]. The height of quadrant glitches generated in the oversized ball preload system and that of the first peak in quadrant glitches generated in the offset preload system can be made uniform by using the above-mentioned technique.

However, it is difficult to make the second peak of quadrant glitches uniform in the offset preload system by suppressing the fluctuation of the friction torque. This is because the appearance changes greatly depending on the specifications of ball screws and the operating conditions. On the other hand, high-precision machining centers and electrical discharge machines such as die machining often adopt the offset preload system. This enables the application of a higher preload than in the oversized ball preload system because they have a problem of quadrant glitches and therefore require high rigidity. To suppress quadrant glitches, it is necessary to take measures for the second peak in an offset preload system. NSK has therefore developed a technology that does not generate a second peak without performing special numerical control by optimizing the internal specifications of the offset preload ball screws.

Generally, in the offset preload system, a region is generated in ball screws where the torque temporarily decreases when the direction of motion is reversed. The region is not generated in the oversized ball preload system but is a property peculiar to the offset preload system, and it impacts the generation of the second peak of quadrant glitches[3]. By reviewing the internal specifications of ball screws, we developed a technology that does not generate a region where the torque decreases when the direction of motion is reversed. This technology, which eliminates the region where the torque decreases in the offset preload system, was first developed by NSK.

Figure 9 shows the circular interpolation motion errors with respect to the command values of conventional ball screws and those applying technology for reducing quadrant glitches, respectively, in the style of a roundness graph. Each ball screw has a shaft diameter of 36 mm and lead of 16 mm. They apply an offset preload system in which a preload is applied so the axial rigidity is equivalent, and the circular interpolation motion has a command value with a feed rate of 300 mm/min and an arc radius of 10 mm. With conventional ball screws, quadrant glitches have two peaks, whereas with ball screws applying technology for reducing quadrant glitches, no second peak is observed, and we can see that there is only one peak.

The smaller the change in acceleration caused by the impact of frictional force during drive reversal, the smaller the peak height of quadrant glitches[5, 6]. This is the same mechanism not only for the first peak but also for the second. Therefore, for the above-mentioned circular interpolation motion, the motion error was measured by changing the feed rate to 600 mm/min while keeping the arc radius as it is. Figure 10 shows the results. The first peak of quadrant glitches is higher than in Figure 9 under both specifications, whereas the second peak does not appear in the ball screws applying technology for reducing quadrant glitches. In other words, this technology is capable of suppressing the second peak even for changes in acceleration that are deemed to impact the first peak.

From the above, by combining the quadrant glitches homogenization technology and newly developed technology for reducing the glitches, it becomes possible to suppress the occurrence of the second peak and stabilize the height of the first. This makes it possible to suppress the quadrant glitches regardless of at which stroke position the correction parameter is identified. We believe that the adoption of this technology will improve the quality of machined surfaces and contribute to the improvement of productivity and energy saving.

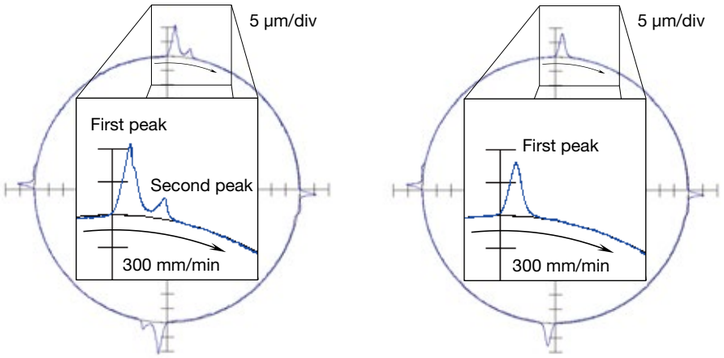

(a) Conventional ball screw

(b) Ball screw applying technology of reducing quadrant glitches

Fig. 9 Circular interpolation motion errors (speed: 300 mm/min)

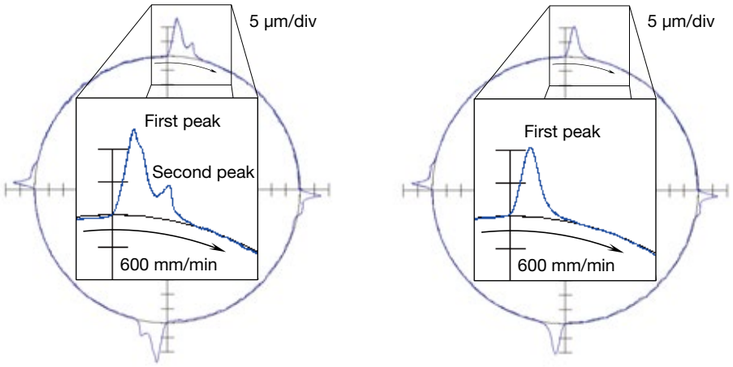

(a) Conventional ball screw

(b) Ball screw applying technology of reducing quadrant glitches

Fig. 10 Circular interpolation motion errors (speed: 600 mm/min)

4. Afterword

In this article, we have introduced the latest technology trends of machine tools based on the investigation results of the JIMTOF exhibited machines. In addition, as a new ball screw technology responding to this, we have introduced a technology to reduce quadrant glitches in machine tools by stabilizing the friction of ball screws.

The technology for controlling the friction of ball screws will be an important factor in advancing the development of environmentally friendly products in the future. NSK will continue to work on improving friction characteristics and develop products that contribute to society.

References

1) Atsushi Matsubara, “Design and Control of Precision Positioning and Feed Drive system,” (2008) 188, Morikita Publishing Co., Ltd.
2) Satoru Arai, “Strategy for Frictional Behavior Control in Ball Screws,” *NSK Technical Journal*, 688 (2016), pp. 45–51.
3) Minoru Hamamura, Jun Fujita, Kazuo Miyaguchi, Yasumi Watanabe, Yoshiaki Kakino, and Atsushi Matsubara, “A study on the friction torque variation of a ball screw at motion direction change—Relationship among friction torque variation of a ball screw at motion direction change of contouring error,” *Journal of the Japan Society for Precision Engineering*, 69-5 (2003), pp. 726–730.
4) Takuro Higuchi, Hiromichi Kunisada, Yoshinori Kunii, Ryuta Sato, and Masaomi Tsutsumi, “Compensation of Quadrant Glitches with Two Peaks in Circular Motions of Machining Centers,” Transactions of the Japan Society of Mechanical Engineers. C, 78-788 (2012-4), pp. 186–195.
5) Ryuta Sato, “Generation Mechanism of Quadrant Glitches on Circular Trajectories,” 2016 Japan Society for Precision Engineering Spring Conference, G01 (2016) 473.
6) Ryuta Sato, “Machined Surface Simulation Techniques Considering the Motion Errors of NC Machine Tools,” *Journal of the Japan Society for Precision Engineering*, 83-3 (2017) p. 204.

Hirose Toshiro

Ueda Masahiro

Oshikawa Keigo

Technical Trends in Bearings for Papermaking Machines

Tsuyoshi Nomura
Industrial Machinery Bearing Technology Center
Wind Turbine and Heavy Industries Technology Department

Abstract

In recent years, the paper manufacturing industry has made increased environmental efforts in areas such as sustainable forestry and paper recycling. In addition, the industry faces increasing pressure to realize a carbon neutral society (reduced CO_2 emissions) and enact measures against global warming. Furthermore, developments such as cellulose nanofibers (CNFs), paper substitutes for plastic, and biomass materials are being promoted as environmentally friendly options for the future.

Demand for paper continues to shift, with increasing demand for packaging paper in lower-income countries and decreasing demand for newspaper and print media as electronic media spreads. Paper manufacturers must alter their production systems to handle these shifts.

Bearings require higher reliability, longer life, and reusability to meet both needs for stable, responsive operation that improves productivity while also reducing CO_2 emissions.

This report explores the problems faced by bearings in the field and the latest technical trends in machines commonly used in the papermaking industry.

1. Foreword

For the paper manufacturing industry, recycling is fundamental in that it applies to both paper and forests (by planting trees), and thus major industry players are actively pursuing global warming countermeasures (reduced CO_2 emissions) toward the realization of a carbon neutral society. As they look toward the future, paper manufacturers are developing eco-friendly materials such as cellulose nanofibers (CNFs)*1, paper materials that substitute for plastics, and biomass plastic materials*2.

The annual production of paper and paperboard worldwide in 2019 was about 420 million tons, with China being the largest producer at about 100 million tons (about 25% of the global total). Meanwhile, the paper and paperboard production shares of the United States, Europe, and Japan, which have in the past driven the market, are declining for reasons including decreases in their labor forces due to declining birthrates and aging populations, the spread of electronic media due to the development of digital technology, and the shift toward paperless offices due to the expansion of teleworking. Along with these factors, demand for types of paper used for newspapers and print is decreasing, while demand for packaged paper is increasing due to the expansion of electronic transactions. Demand for sanitary paper is also increasing in emerging and developing countries. Paper manufacturers are adapting their production systems to respond to all of these trends.

At papermaking sites, improving productivity through stable equipment operation is critical. These facilities are therefore expanding their preventive maintenance measures by monitoring the condition of bearings for each piece of equipment, and they demand that bearings demonstrate high reliability and high speed. Furthermore, in order to reduce CO_2 emissions and maintenance costs, there is strong demand for bearings to last longer and be reusable.

Discussed in this article are the problems associated with bearings currently used in each section of paper machines at papermaking sites and notes on technological trends.

*1 Next-generation food-derived material
*2 Plastics made from biological resources

2. Papermaking Process and Bearings

Figure 1 shows the structure of a typical paper machine. Each process starts with a headbox and finishes with the reel section. Details are below.

1. Headbox: Raw materials for paper are ejected uniformly and evenly.
2. Wire section: The raw materials of the ejected paper are spread thinly on a wire (metal or plastic), forming the paper layer, and then dehydrated using suction. Through this process, the water content of the paper is about 80%.
3. Press section: Dehydration and water extraction are performed on the wet paper using pressure to squeeze out water. This also flattens the paper surface and increases its density. Through this process, the moisture content of the paper decreases to 40–60%.
4. Dryer section: Dozens of rotating hollow rolls (or one large-diameter roll) are heated at a high temperature using steam. The wet paper is then kept in the rolls (or roll) to dry. Through this process, the water content of the paper decreases to 5–10%.
5. Calendar section: Heat and pressure are applied between rolls, creating a smooth, uniform thickness and glossy appearance.
6. Reel section: A piece of paper with a width of about 10 meters and a length of several thousand to tens of thousands of meters are wound up at the same time.

About 350 rolls are arranged in the paper machine equipment, with spherical roller bearings being used mainly as support. The bearing size, lubrication method, and usage environment differ for each section, as do the functions required for the bearing. Table 1 summarizes the details of each part. Below is an explanation of the technical issues related to spherical roller bearings for paper machine rolls and notes regarding recent trends.

Issues with spherical roller bearings for paper machine rolls:
- Overall functionality of spherical roller bearings (for rolls used in all sections)
- Size expansion of bearings that prevents inner-ring cracking (for rolls in the press, dryer, and calendar sections)
- Size expansion of bearings that prevents smearing (for rolls in the press section)
- Low vibration and low heat generation of bearings in high-speed paper machines

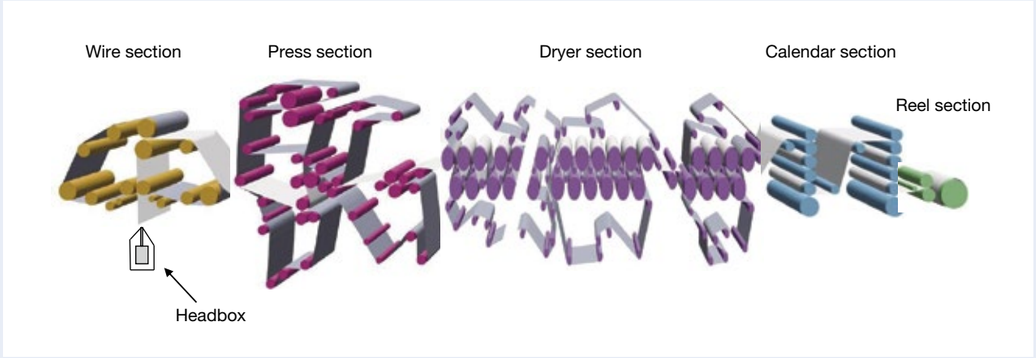

Fig. 1 Papermaking process

Table 1 Spherical roller bearings for papermaking lines

Papermaking process	Bearings and lubrication	Usage environment	Technical requirement
Wire section (dehydration section)	Bearing: S-SRB, L-SRB, G-SRB Lubrication: Grease, oil (circulating lubrication)	Environment around roller bearing: Water	- Long-lasting - Prevents smearing under light loads - Prevents inner-ring cracking caused by excessive push-in amounts at inner ring - Higher speed
Press section (compressed/ dewatering section)	Bearing: S-SRB, L-SRB, G-SRB Lubrication: Grease, oil (circulating lubrication)	Environment around roller bearing: Water Light load (suction roll inner portion)	
Dryer section (drying section)	Multi-cylinder dryer: S-SRB, L-SRB Yankee dryer: G-SRB Lubrication: Oil (circulating lubrication)	High temperature (heating medium passes through the hollow shaft)	- Long-lasting - Prevents inner-ring creep caused by secular dimensional changes - Prevents inner-ring cracking due to increased mating stresses caused by thermal expansion and excessive push-in amounts at inner ring
Calendar section (glossy section)	Bearing: S-SRB, L-SRB, G-SRB Lubrication: Oil (circulating lubrication)		
Reel section (reel replacement section)	Bearing: S-SRB, L-SRB Lubrication: Grease, oil (oil bath lubrication or circulating lubrication)	—	Long-lasting
Winder (rewinding)	Bearing: S-SRB, L-SRB Lubrication: Grease, oil (oil bath lubrication or circulating lubrication)	—	Long-lasting

"SRB" means Spherical Roller Bearings.
Bearing outer diameter S-: less than 400mm L-: 400-600mm G-: 600mm or more

3. Higher Functionality of Spherical Roller Bearings

In response to the needs of industrial machinery, NSK developed and launched a high-performance standard series of spherical roller bearings (Figure 2) in 2004. This bearing also meets the demand for bearings of higher functionality that support paper machine rolls. At the start of development, we supported only an outer diameter of 260 mm or less, but in recent years, in response to the need for higher functionality in large bearings due to increases in equipment size, we have developed bearings that can support an outer diameter of up to 600 mm (Figure 3).

This bearing was developed based on research on the mechanism leading to surface damage particular to spherical roller bearings and its countermeasure technology, and its features are detailed below and in Figure 4. This product has a broad lineup and is widely used for roll support in each paper machine process, and we believe it will continue to meet the high reliability requirements of paper machines.

Features:

1) The new bearing allows for optimal friction of the outer ring and rollers and reduces slippage of the inner ring and rollers, thus offering twice the life of conventional bearings.
2) The design of the guide ring of the large spherical rolling bearing has been optimized to suppress tilting in the rollers, creating 30% less heat generation compared to conventional bearings.
3) Heat treatment has been applied for dimensional stability in a wide range of temperatures (up to 200°C).

Fig. 2 High-performance standard series of spherical roller bearings

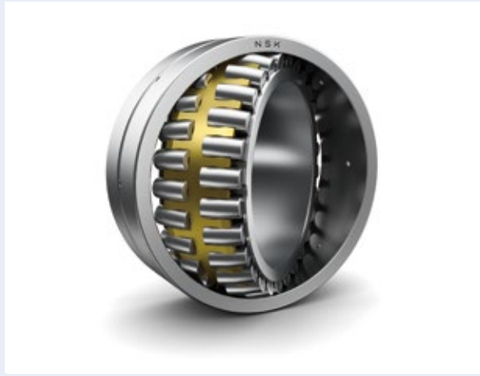

Fig. 3 High-performance standard series of large spherical roller bearings

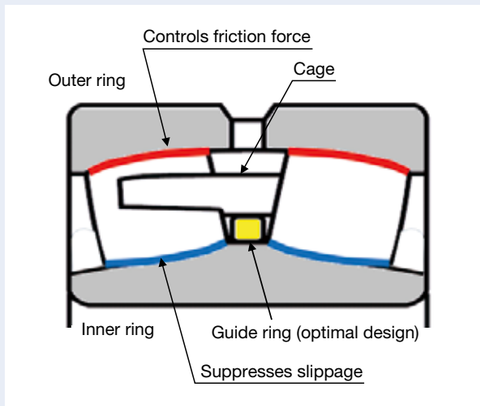

Fig. 4 Characteristics of the new bearing

4. Size Expansion of Special Bearings for Different Applications

4.1 Bearings that prevent inner ring cracking (large TL bearing)

Figure 5 shows an example of the structure of a bearing for a roll mounted in the paper machine dryer section (hereinafter referred to as the “dryer roll”). In this structure, a spherical roller bearing at the inner diameter’s tapered bore is set by pushing it into the shaft via a sleeve. It is used by adjusting the optimum bearing residual clearance and interference according to the push-in amount.

The push-in causes expansion of the inner ring of the bearing, resulting in tensile stress (hoop stress). Also, since a high-temperature medium (steam) passes through the hollow shaft of the dryer roll, the shaft expands during operation, causing inner ring hoop stress to increase further. Under such conditions, inner ring cracking (Figure 6) may occur. Due to the high temperature, early flaking due to insufficient lubrication, oil film formation, and secular changes in the bearing due to long-term use have resulted in cases of creep damage between the inner ring and shaft. Similar cases have been confirmed for the roll in the calendar section (hereinafter referred to as the “calendar roll”) because the heat medium (oil) passes through a hollow shaft. Importantly, cracks in the inner ring are likely to cause serious accidents that may lead to production suspension, so it is necessary to improve the reliability of equipment by taking measures regarding the bearings.

Fig. 6 Inner ring fracture (spherical roller bearings)

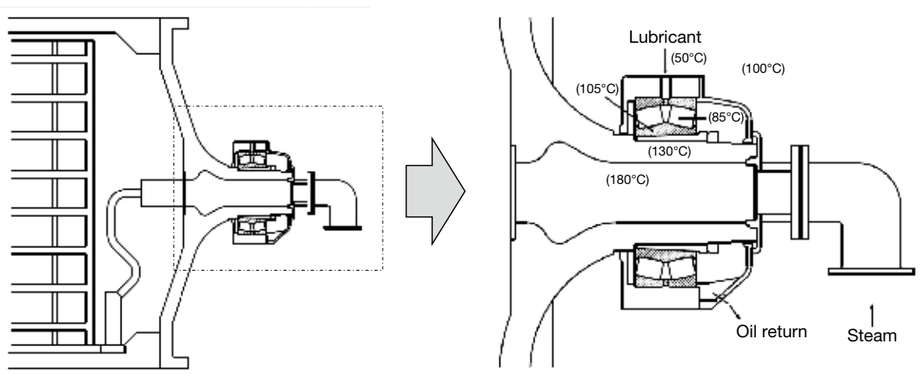

Fig. 5 Example of bearing mounting structure for the dryer roll

To solve the previously described problems, we have developed the TL (Tough & Long Life) bearing. By applying special carburizing treatment to the material, this new, advanced bearing has high inner-ring cracking resistance and excellent dimensional stability at high temperatures. There are two types of dryer rolls—multi-cylinder dryers and Yankee dryers (Table 2)—and it has been confirmed that TL bearings are effective with both of them.

In the past, NSK’s TL bearings supported an outer diameter of less than 650 mm. In recent years, however, in response to requests for a larger bearing to support large rolls in the press sections of both Yankee dryer rolls and calendar rolls, we have developed a large bearing that can support an outer diameter of up to 1 000 mm. This large TL bearing has been on the market since 2018, and we believe that it is meeting the demand for improving the reliability of large paper machines in line with current trends in paper demand, particularly in Asia.

4.2 Bearings that prevent smearing (large NSK DLC bearings)

The spherical roller bearings used to support the rolls of each section of the paper machine may cause a type of damage called “smearing” (Figure 7). This means that a small seizure is caused by slippage between the rolling element and raceway ring as well as poor lubrication under light load conditions. Smearing may develop into

Fig. 7 Smearing damage (rolling surface of rollers)

Table 2 Multi-cylinder dryer and Yankee dryer

Type	Overview	Dryer roll layout
Multi-cylinder dryer	Used for paper in general. Dozens of rolls with a diameter of about 1.5 m are placed to evaporate the water and dry the material. Bearing outer diameter: less than about 600 mm	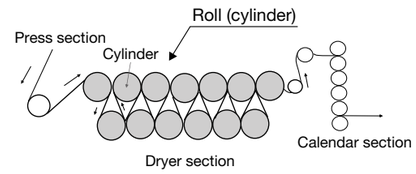
Yankee dryer	Mainly used for tissue and toilet paper. It has a diameter of about 3 to 6 m and is dried with a single Yankee dryer. Bearing outer diameter (approximate): 600–1 200 mm	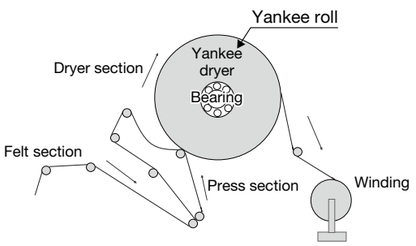

flaking or cracking, leading to a sudden shutdown of production equipment. A typical area where smearing occurs is the suction roll inside the bearing at the press section (Figure 8). This inside bearing has an outer diameter of 260 mm or less and is used for lubrication (oil or grease). Although the bearing supports the suction box, it is likely to cause smearing due to poor lubrication resulting from water intrusion into the bearing. To prevent this, NSK has developed an NSK DLC (Diamond Like Carbon) coating, which features significantly improved adhesion and durability using our unique, proprietary coating technology (Figure 9).

In recent years, smearing has been confirmed on large spherical roller bearings (outer diameter of up to 1 000 mm) used for outer ring rotation in press rolls. To meet the demand for preventative measures, we are developing a large spherical roller bearing (large NSK DLC bearing) with NSK DLC coating, which prevents smearing.

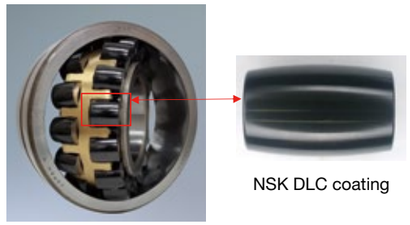

Fig. 9 Spherical roller bearing with NSK-DLC coating

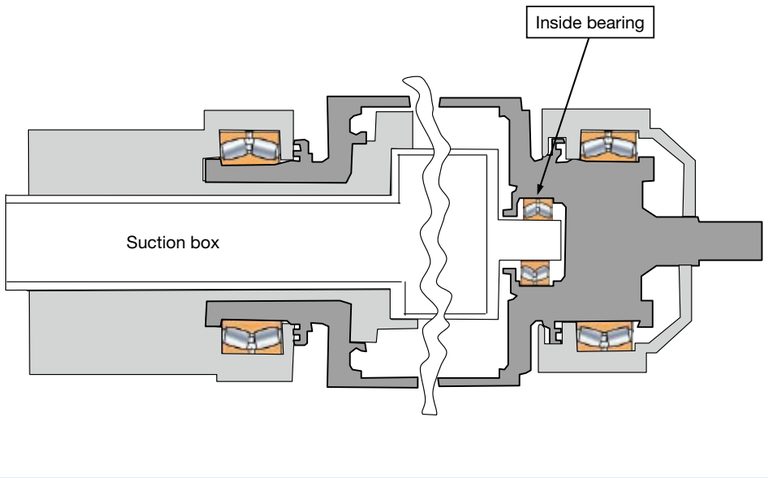

Fig. 8 Structure of the press part and suction roll

5. Response to Higher Speeds

The papermaking speed (production speed of papermaking equipment) of a typical paper machine is about 1 500 m/min, but paper manufacturers have been increasing the speed in order to improve production efficiency. Also, in recent years, more equipment with a papermaking speed of the 2 000 m/min class has been put into operation. The main problems with high-speed rotation are bearing vibration and heat generation. Vibration has a large impact on product quality, and excessive heat generation may cause production-line seizure. For these reasons, appropriate countermeasures for bearings are in high demand. To meet the need for high speed functionality, NSK has developed a bearing that can support 2 500 m/min, and we have substantially improved the components' accuracy in order to suppress vibration and heat generation under high-speed rotation.

6. Afterword

We have outlined recent trends in bearing technology used in papermaking machines (paper machine rolls).

Until now, NSK has focused on improving the productivity of paper manufacturing user equipment and has developed highly reliable and long-life bearings to address mainly the technical issues related to bearings used in paper machine rolls. In the future, we will work to meet reuse needs by applying bearing diagnostic technology and focusing on CO_2 reduction in bearing manufacturing to help realize a carbon neutral society.

References

1) *NSK Technical Journal*, No. 680 (2006), pp. 6–12.
2) *NSK Technical Journal*, No. 682 (2007), pp. 8–13.
3) *The Tribology*, Shinjusha No. 212 (2005), pp. 10–12.
4) *NSK Technical Journal*, No. 658 (1994), pp. 1–10.
5) *The Tribology*, Shinjusha No. 363 (2017), pp. 12–14.

Tsuyoshi Nomura

Development of High-Speed Ball Bearings for Hybrid Electric Vehicles (HEVs) and Electric Vehicles (EVs)

Eisaku Suzuki, Yasuhiro Iwanaga, and Yoshimune Shimokawa
Automotive Technology Development Center, Automotive Bearing Technology Center, Powertrain Bearing Technology Department

Abstract

In recent years, motivated by environmental concerns such as global warming, the automotive industry is rapidly moving to help achieve a carbon neutral society by expanding the development and production of hybrid electric vehicles (HEVs) and electric vehicles (EVs). Accordingly, with the goal of improving the fuel economy of HEVs and EVs and increasing cruising range, bearings used in drive motors are subjected to increasingly higher speeds and performance demands.

However, bearings under high-speed operation can suffer from grease deterioration due to high temperatures, resulting in bearing seizure. High speeds can also lead to the bearing cage becoming deformed by centrifugal forces, resulting in heat generation and cage damage through contact with the outer ring and seals.

NSK enables operation at 1.4 million dmN for Gen 2 bearings and at 1.8 million dmN for Gen 3 bearings through proprietary greases, lightweight designs, and new high-rigidity materials. In this article, we will introduce high-speed technologies and evaluate grease-lubricated ball bearings for HEV and EV motors.

1. Foreword

Given the increased awareness of environmental issues such as global warming, carbon neutrality has become a high priority for consumers, and hybrid electric vehicles (HEVs) and electric vehicles (EVs) with smaller environmental loads are expected to be widely used. Since one critical issue in the development of EVs is extending their travel range, developers must improve fuel economy and power while also designing vehicles with enough space to mount long-lasting batteries. To do this, drive motors for HEVs and EVs must be smaller and lighter than they are today[1].

Since the output of a motor is determined by the product of torque and rotation speed, if rotation speed is increased, then torque is reduced, thus the rotor and peripheral parts can be made smaller, requiring drive motors with higher speed rotation for HEVs and EVs. Recently, developers have introduced an EV unit featuring a drive motor with a rotation speed higher than 30 000 rpm[2], so rolling bearings that support such drive motors must be able to rotate at 30 000 rpm or higher.

Developers use dmN as the index to measure the high-speed rotation of bearings. As shown in Figure 1, the dmN value is the product of the pitch circle diameter (dm) and bearing's rotation speed (N). In drive motors for HEVs and EVs, bearings with an inner diameter of 30 mm to 35 mm (pitch circle diameter of 45 mm to 50 mm) are most common. Therefore, to achieve high-speed rotation of 30 000 rpm or more, developers must use rolling bearings that can rotate with at least 1.4 million dmN.

2. Challenges in High-Speed Rotation

Generally, developers use deep groove ball bearings in drive motors for HEVs and EVs. When the ball bearings rotate at a high speed, the temperature inside the bearing rises due to heat generated by slippage, resulting in insufficient oil film formation between the steel ball and raceway ring, leading to seizure. In addition, the cage is deformed as centrifugal force increases, and there are problems such as excessive heat generation and damage to the cage due to the balls being restrained and coming into contact with the outer ring and seal. Therefore, in order to achieve high-speed rotation of ball bearings, we must develop a lubrication method that reduces heat and a cage that reduces deformation.

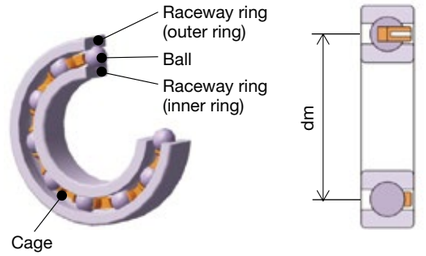

dmN = pitch circle diameter (dm) × max. rotation speed (N)

Fig.1 High speed rotation index

3. High-Speed Rotation Technology for Deep Groove Ball Bearings

3.1 Grease optimization

Lubrication methods for rolling bearings are classified into either oil lubrication or grease lubrication. For high-speed rotation, oil lubrication is best because it easily releases heat inside the bearing to the outside. Using oil lubrication, we can reach 1.4 million dmN or more with existing technology (high-speed specification Gen 1 described later). While it is difficult to achieve 1.4 million dmN or more with grease lubrication using existing technology, we must develop high-speed bearings for HEV and EV motors that are used for grease lubrication.

The driving environment of automobiles ranges from extremely low to extremely high temperatures, and suppressing heat generation across such a wide temperature range requires grease for drive motor bearings. NSK has developed EA9 grease, which has improved high-speed performance over a wide range of temperatures. By using poly-α-olefin, a base oil with strong heat resistance, we can limit grease deterioration and ensure durability. The base oil includes a suitable amount of urea-based thickener, which has excellent high-speed and high-temperature properties, thus optimizing oil separation (exudation of base oil from the thickener) and improving seizure resistance by increasing grease fluidity and reducing agitation resistance over a wide range of temperatures. As shown in Figure 2, the use of EA9 grease reduces heat generation in both extremely low- and high-temperature environments, thereby improving high-speed rotation performance (Figure 2).

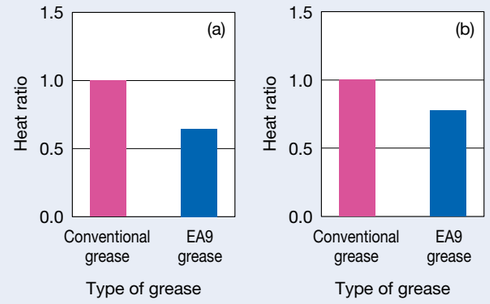

Fig. 2 Comparison of heat generation with EA9 grease[1]
(a) –30°C (b) 80°C

3.2 Cage-shape optimization

For deep groove ball bearings for HEVs and EVs, we use iron cages and crown-type resin cages (hereinafter referred to as “resin cages”) (Figure 3). Since resin cages are lighter than those made of iron, the centrifugal force at high-speed rotation is comparatively small, as is the friction coefficient between the steel ball and the cage pocket. This reduces heat generation between the ball and cage at the contact point.

As shown in Figure 4, we have confirmed that a resin cage generates less heat than those made of iron, and the former can improve high-speed rotation performance. Historically, high-speed rotation bearings use resin cages (high-speed specification Gen 1). In order to limit reductions in the strength and rigidity of cage material due to the temperature rise during high-speed rotation, the cage must be made with highly heat-resistant resin material.

As mentioned above, when a resin cage is used at high-speed rotation, there can be problems such as claw tip deformation on the circumference due to the impact of centrifugal force, which causes interference with the outer ring and seal, and damage caused by excessive stress generated on the pocket bottom. When designing a resin cage, we analyze the strength of the cage while considering the centrifugal force and optimizing the thickness of the pocket bottom according to the usage conditions in order to avoid contact or breakage with other parts due to deformation of the cage (Figure 5). However, when the thickness of the pocket bottom increases, the axial dimensions of the cage and bearing expand, and problems occur due to the axial length and weight of the motor increasing.

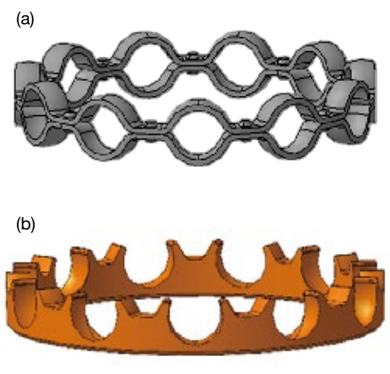

Fig. 3 Difference between the steel cage and plastic cage
(a) Steel cage (b) Plastic cage

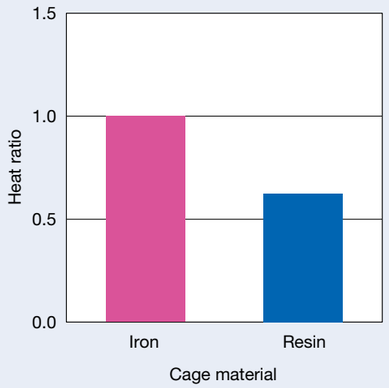

Fig. 4 Comparison of heat generation by cage material[1)]

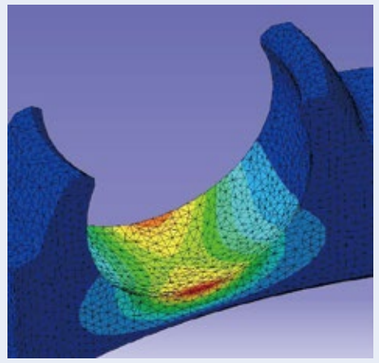

Fig. 5 Example of cage strength analysis technology[1)]

To address this, we have reviewed the concept of resin cage design since the announcement of high-speed specification Gen 2. With the goal of reducing cage weight to reduce centrifugal force, we reconsidered the cage shape instead of making the cage highly rigid (thick) to withstand the centrifugal force. Figure 6 shows the cage shape for high-speed specifications Gen 2 and 3.

To reduce cage weight, we decreased the thickness of the peripheral section of the claw tip, making it thinner than the claw root in order to reduce the centrifugal force. Also, we significantly reduced the thickness of the claw root most affected by deformation and changed the shape so the annular part can connect smoothly to the claw in an arc. This resulted in a bout a 50% reduction in claw deformation compared to high-speed specification Gen 1 (Figure 7).

In designing the cage shape of high-speed specification Gen 2, we achieved weight reduction owing to the experience and insights of our designers. In designing high-speed specification Gen 3, we determined the cage shape by calculating topology optimization. In addition, by reducing the number of prototypes and experimenting as much as possible using a range of analytic technology, we succeeded in developing Gen 3 within about one year after developing Gen 2.

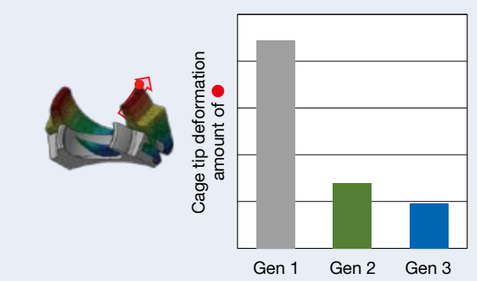

Fig. 7 Deformation results for the cage tip

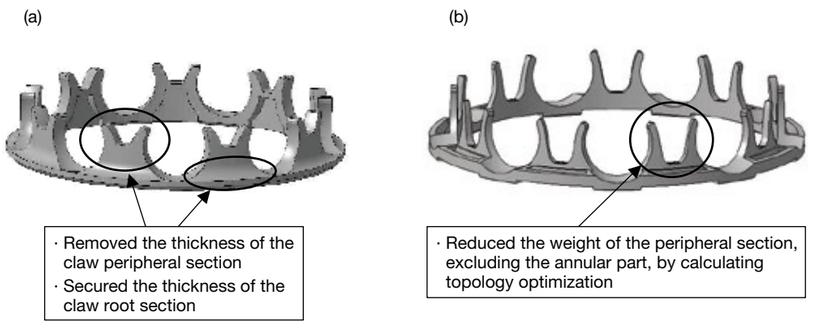

Fig. 6 Characteristics of Gen 2 and 3 shapes
(a) Gen 2 (b) Gen 3

Topology optimization calculation is a design method that sets a shape as a design variable and strength or rigidity as an objective function and deletes parts not related to the objective in the design space in order to achieve optimization (lightweighting)[3]. NSK is the first company in the world to apply calculations for topology optimization to bearing design and succeed in putting it into practical use. Figure 8 shows the design flow of the Gen 3 cage. As shown in Figure 8 (b), the shape derived solely through calculations for topology optimization does not take the manufacturing aspect into consideration, which may cause defective resin molding during manufacturing and cage damage during assembly. Therefore, based on the shape obtained by calculations for topology optimization, we conducted fluid analysis of the resin during resin injection and stress analysis during assembly, thereby improving the shape to a manufacturable specification. The high-speed specification Gen 3 reduces weight by about 70% compared to Gen 1 by reducing the weight of the peripheral section of the cage (besides the annular part) and reducing centrifugal force.

3.3 High-rigidity resin material

The resin cage material used at high-speed rotation must have high rigidity in order to limit deformation due to the influence of centrifugal force. Therefore, in high-speed Gen 2 and later specifications, we added reinforcing fiber to PA (polyamide), which is the cage material, switching from glass in Gen 1 to carbon. By changing the fiber to carbon, rigidity increases and gravity decreases. As shown in Figure 9, the resin material has about 30% less deformation compared to conventional glass-fiber resin, which limits deformation due to the impact of centrifugal force during high-speed rotation. This material also improves dimensional stability since it has low water absorption and limited dimensional change.

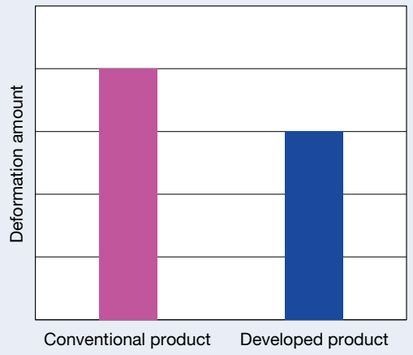

Fig. 9 Deformation of plastic material

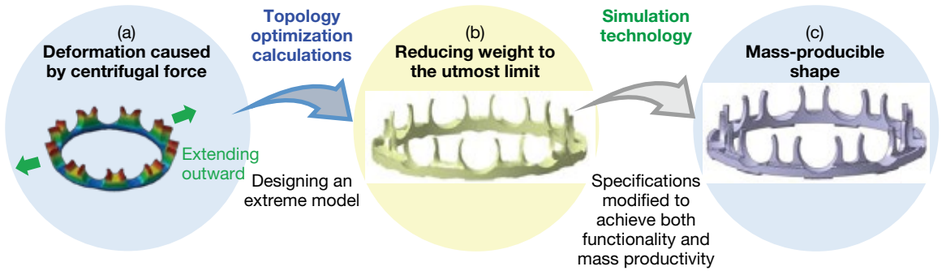

Fig. 8 New design method for Gen 3 cages
(a) Deformation (b) Working shape (c) Final shape

4. Evaluation Test Results

As mentioned above, the high-speed ball bearings Gen 2 and 3 for drive motors for HEVs and EVs are able to rotate at a high speed due to (1) the application of NSK original grease EA9, (2) a lightweight shape that reduces centrifugal force, and (3) a resin case made of high-rigidity material. Here we show the results of evaluating the high-speed rotation performance of the high-speed specifications for Gen 2 and 3.

4.1 Visualization of cage deformation

In Figure 7, our analysis showed the effects of limiting cage tip deformation in Gen 2 and 3 during high-speed rotation, and these effects were confirmed through actual measurement. We attached the cage to the shaft and rotated it at a high speed, then we documented the deformation behavior with a high-speed camera to measure the amount of cage deformation.

Figure 10 shows the results of observing the cage deformation from Gen 1 through 3 during high-speed rotation. In the test, the cage rotation speed was equivalent to two million when converted to the dmN of the bearing, and the temperature was 120°C. Figure 10 (a) shows the observation results of Gen 1, (b) shows those of Gen 2, and (c) shows those of Gen 3. The dotted line in the figure shows the position of the cage's outer diameter surface when the cage is not in rotation. The amount of deformation was measured by reading from the image the amount of deformation in the radial direction from the initial position. As a result, the deformation of Gen 1 was confirmed to be 1.77 mm, the deformation of Gen 2 was confirmed to be only about 0.35 mm, and the deformation amount of Gen 3 was almost unreadable. From the results shown in Figure 10, we confirmed that the deformation of Gen 2 and 3 cages during high-speed rotation caused by centrifugal force was limited due to the reduced weight and application of high-rigidity material.

4.2 High-speed rotation

We conducted a high-speed rotation durability test to confirm the high-speed rotation performance of Gen 2 and 3, and Figure 11 shows the structure of the testing machine. Four bearings support the shaft, with the two at the ends as test bearings and the two in the center as support bearings. The support bearings use oil lubrication. Test conditions were such that the radial load was 10% of the basic dynamic load rating of the bearing, and the test temperature was adjusted with a heater so the outer ring's outer diameter temperature reaches 120°C. The test's censoring time was 20 hours.

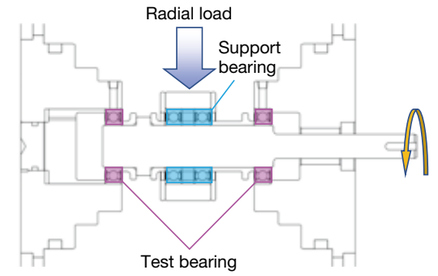

Fig. 11 High-speed rotation tester

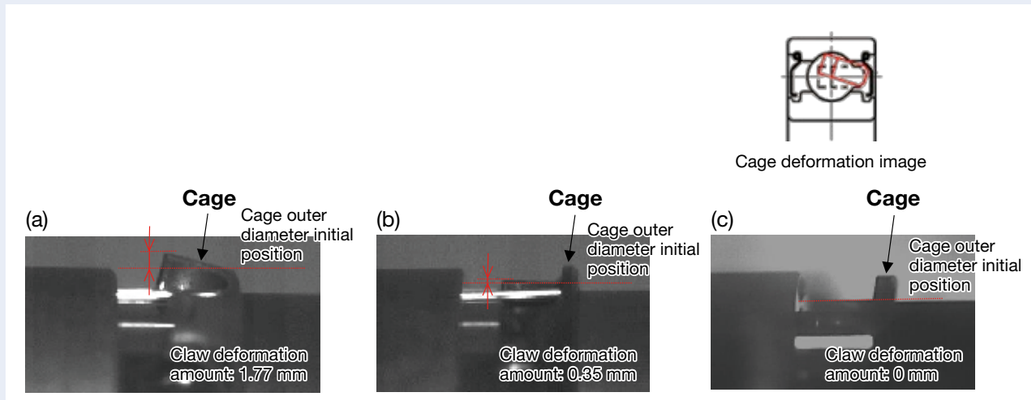

Fig. 10 Visualization of the cage deformation test results
(a) Gen 1 (b) Gen 2 (c) Gen 3

Figure 12 shows the test results. Figure 12 (a) shows the test results of Gen 2, and Figure 12 (b) shows those of Gen 3. As shown in Figure 12 (a), Gen 2 reached the target time without causing abnormal heat generation under the condition of 1.4 million dmN. However, under the condition of 1.6 million dmN, abnormal heat generation occurred in about seven hours. After observing the inside of the bearing that caused abnormal heat generation under the condition of 1.6 million dmN, we found that the cage was deformed due to the impact of centrifugal force and that there was a trace of interference with the seal. Conversely, Gen 3 reached the target time without abnormal heat generation, even under the condition of 1.8 million dmN, as shown in Figure 12 (b). We reduced the weight of the Gen 3 cage further, compared to Gen 2, by using topology optimization calculations and, because of that weight reduction, we achieved high-speed rotation of at least 1.8 million dmN. With the development of Gen 3, NSK has achieved the world's highest level of speed as a grease lubricated, deep groove ball bearing for EV drive motors.

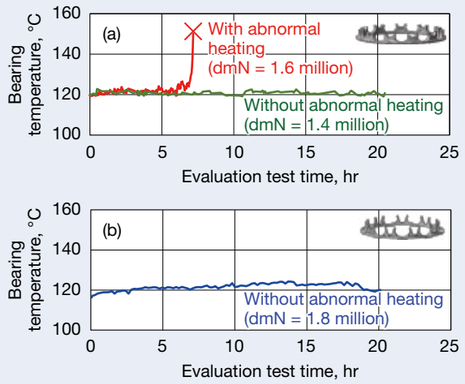

Fig. 12 High-speed rotation evaluation test results
(a) Gen 2 (b) Gen 3

4.3 Torque performance

The Gen 3 cage, the weight of which we have reduced to the utmost limit by pursuing high-speed performance, has about 60% smaller volume compared to the conventional high-speed specification for Gen 1. We therefore believe that the agitation resistance of the lubricating oil caused by the cage becomes smaller during high-speed rotation, thereby reducing torque. To test this theory, we measured and compared the friction of Gen 1 and 3. The testing machine structure was the same as that of the high-speed durability tester, shown in Figure 11, but we measured the test bearings with oil lubrication as well as the support bearings. The conditions for this measurement were such that the radial load was 5% of the basic dynamic load rating of the bearing, the rotation speed was increased by 2 500 rpm from 10 000 rpm to 20 000 rpm, and the oil temperature was 50°C.

As shown in the measurement results in Figure 13, the friction of Gen 3 was reduced over the entire speed range compared to Gen 1, confirming the effect of reducing friction by about 10% when the amount of lubricating oil is 100 cc/min and about 25% when the amount of lubricating oil is 200 cc/min. When using bearings at high-speed rotation, problems result from increased friction due to agitation of the lubricating oil, but by applying Gen 3, the friction of the bearing is reduced, further improving the fuel and power economy of HEVs and EVs.

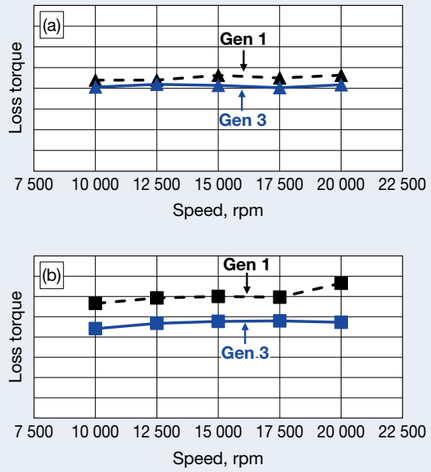

Fig. 13 Torque evaluation test results
(a) 100 cc/min (b) 150 cc/min

5. Afterword

In this article, we have introduced the grease lubricated high-speed ball bearing for drive motors for HEVs and EVs.

By applying our original high-speed grease EA9 and reducing the weight of high-rigidity materials and cages, NSK has achieved high-speed rotation of 1.4 million dmN or more for the high-speed specification Gen 2, and 1.8 million dmN or more for Gen 3.

We expect that the use of electric vehicles such as HEVs and EVs will increase rapidly, given the trend toward becoming a carbon neutral society. By fully understanding the usage environment and continuously promoting product development that meets the needs of the market, NSK will contribute to improving the fuel economy and power of HEVs and EVs, thus also improving their reliability.

References

1) Yasuhiro Iwanaga, "Latest Technical Trends for HEV/EV Powertrain Bearings," *Monthly Tribology*, 2019.10.
2) Kosuke Aiki, Mathias Deiml, Tommie Eriksson, Matthias Schneck, and Peyman Jafarian, "Development of High Speed Electric Drive Unit," Proceedings of the 2019 annual congress of the Society of Automotive Engineers of Japan (2019), 20195157.
3) Shintaro Yamazaki, "Topology Optimization and New Development," *Control: Information Systems Control Journal*, Vol. 61, No. 1, 2017, pp. 29–34.

Eisaku Suzuki

Yasuhiro Iwanaga

Yoshimune Shimokawa

Hub Unit Bearing Design Using Digital Twins

Hideo Nishizawa
Automotive Technology Development Center
Automotive Bearing Technology Center
Chassis Bearing Technology Department

Abstract

Needs for automobiles that are environmentally friendly and feature improved performance are increasing day by day. NSK continues to work on increasingly sophisticated design technology using numerical analysis to improve the performance and development speed of hub unit bearings. We define the reproduction of a real, physical phenomenon with a digital numerical analysis model as a Digital Twin (DT).

This article presents some examples of DT techniques used in designing third-generation hub unit bearings. Since hub unit bearings support the vehicle body, considering their strength and rigidity is especially important. In these calculations, we use finite element analysis (FEA) to obtain data on stress and deformation. We succeeded in reducing analysis time by using high-performance computing and a unique algorithm. We will continue to develop DT technology toward a state where trial production is unnecessary.

1. Introduction

In recent years, developed nations have launched various policies toward achieving carbon neutrality. These include tightening fuel efficiency regulations for automobiles and the eventual elimination of those with combustion engines. In addition, analysts say the automobile industry is entering an era of reform unlike any other in 100 years, such as the practical application of automated driving by utilizing ICT. In response to these trends, NSK has developed an advanced design technology using numerical analysis and has been streamlining its processes (fewer tests and evaluations) in the areas of weight reduction, decreased friction, and higher performance in hub unit bearings. NSK's development and design technology has led to new solutions by making full use of phenomenon prediction technology using a digital numerical analysis model gleaned from observing and measuring actual physical phenomena, which has been verified for accuracy. We call the development and design technology Digital Twin (DT).

While we produce first- to third-generation hub unit bearings, this article discusses the design of the third-generation hub unit bearings only since they require advanced design technology. Figure 1 shows an overview of the hub unit bearings mounted on the driving and non-driving wheels of passenger cars. In addition to the two rows of bearing sections, the bearing has a unitized flange for fastening to vehicles, wheels, and brakes, making it smaller and lighter and thus more highly functioning as well as easier to assemble and maintain than conventional single row bearings.

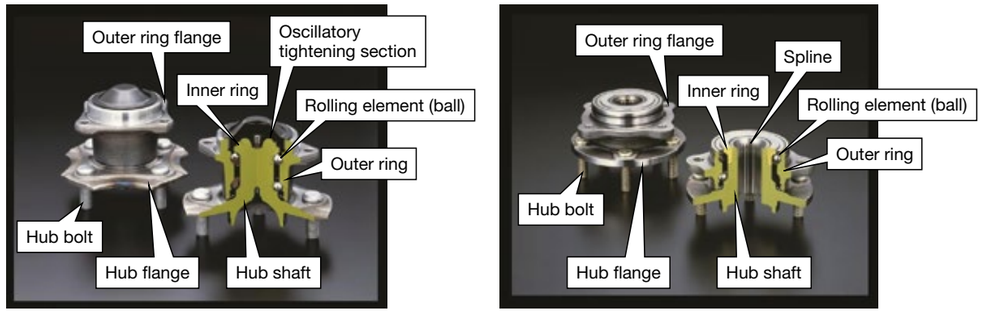

Fig. 1 Hub unit bearing[1)]

Usually, hub unit bearings are designed exclusively for each vehicle or platform. We have reduced the number of tests and evaluations as much as possible to reduce development man-hours and costs, and we have applied DT in a wide range of fields in order to develop the optimum design. Figure 2 outlines the design procedure for hub unit bearings. We have classified the process into two types: bearing internal design (process (1)) and unit component design (process (2)). We often use process (1) with in-house numerical analysis software and commercially available dedicated analysis software that has earned an extensive and proven track record as the bearing specific theory, and its formulation and standardization have progressed. Since most of such software can be used on an ordinary PC and has short calculation times, we are also working on a design using a multi-objective optimization algorithm that combines several pieces of analysis software. We often use process (2) with a highly versatile numerical analysis method, such as commercially available FEA software.

Recently, cost reductions for high-speed arithmetic units such as multi-core CPUs and GPGPUs, large-capacity memories, and high-speed and large-capacity storage systems have become widespread. As a result, computing power improved dramatically even for relatively small-scale calculation systems, making finite element analysis (FEA), using a large-scale model, available for everyday design studies. NSK is accelerating the utilization and deployment of DT by creating an environment in which design engineers can operate and execute large-scale analysis, which analytics specialists often used previously for research. In the following sections, we will introduce some of the latest DT utilization examples in the design process.

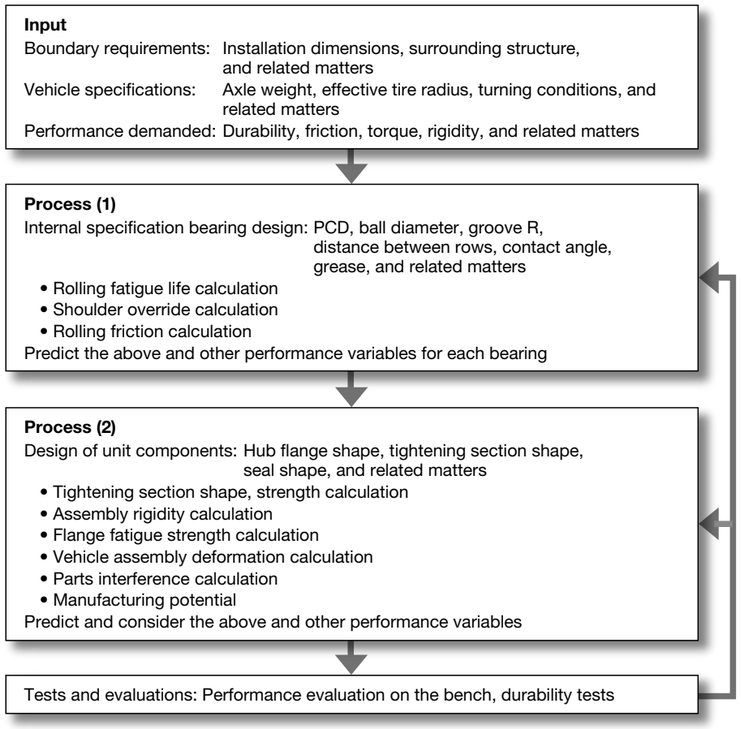

Fig. 2 Design flow for hub unit bearing

2. Example of Rolling Fatigue Life Prediction of the Raceway Ring

Figure 3 shows an example of a shoulder override state in which the contact range between the rolling element and raceway ring groove exceeds the groove shoulder when a large load is input, causing excessive contact surface pressure. Depending on vehicle usage conditions, it is difficult to avoid shoulder override, so precision contact analysis is necessary to study the optimum shape of the groove shoulder. Figure 4 shows the results of the durability test and contact stress analysis after taking countermeasures. By keeping the contact stress generated near the shoulder of the raceway surface low, we successfully prevented early rolling fatigue damage.

Normally, rolling fatigue life is evaluated based on the calculated life standardized by ISO281[2]. However, as part of its design process, NSK is studying ways to prevent fatal damage to hub unit bearings by studying precise rolling fatigue life while also considering the effects of fastening the mating parts to the outer ring flange.

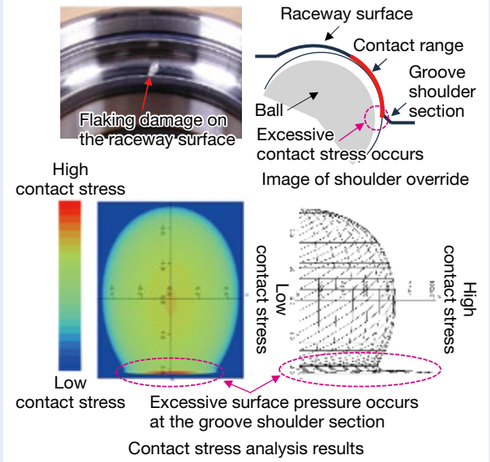

Fig. 3 Example of flaking damage from shoulder override and contact stress analysis results

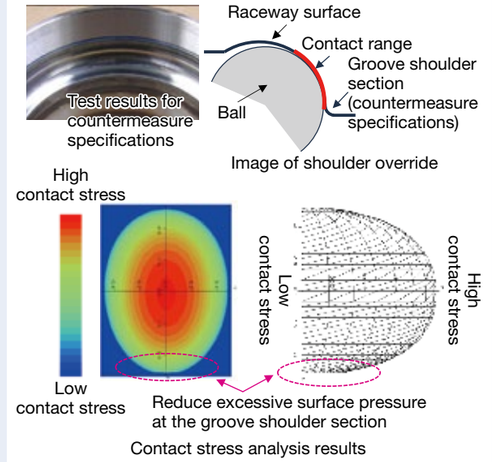

Fig. 4 Endurance test results and contact stress analysis results for anti-override specifications

3. Example of Shape Prediction of the Oscillatory Tightening Section

Figure 5 shows an example of elasto-plastic finite element analysis (elasto-plastic FEA) for determining shape and residual stress after oscillatory tightening. For the analysis, we used Deform[3], which is excellent in terms of tightening the die operating condition setting and large-scale plastic deformation analysis. Figure 5 also shows the high accuracy in the shape prediction of the obtained tightening section. The machining conditions entered in the analysis reflected the machining load measurement results using the actual manufacturing equipment. In addition, material properties such as a stress-strain curve were taken from various material tests. Since the strength (hardness) and residual stress after machining can be obtained from the analysis results, it is possible to predict the fatigue strength during the vehicle's operation. Using this method made possible greater efficiency of the tightening section design, which used to rely heavily on a simple analysis method and trial and error of the actual machine.

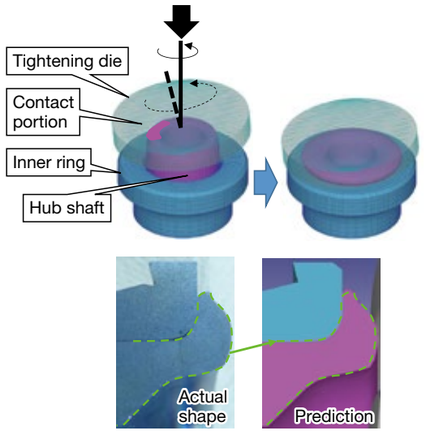

Fig. 5 Analysis of oscillatory tightening

4. Example of Rigidity Prediction

Hub unit bearings support the inertial force generated by vehicle weight and motion such as turning, and the magnitude of deformation (rigidity) is an important factor affecting the dynamics of vehicle performance. We have classified deformation into three types: (1) deformation of the hub shaft (including the hub flange), (2) contact deformation between the rolling element and raceway ring, and (3) deformation of the outer ring flange. We arranged individual sections in a series so that they rely on each other, and they have a non-linear load displacement characteristic that involves contact. We used non-linear finite element analysis (non-linear FEA) to predict such stiffness, and Abaqus[4] as the analysis software. Figure 6 shows a schematic diagram of the rigidity evaluation test and an example of an analysis model. The hub flange and load jig, and the outer ring flange and fixing jig, are fastened with bolts, respectively. Constant velocity joints are also fastened with nuts. In the analysis, the screw portions for bolts and constant velocity joints are not modeled to achieve simplification, but a compressive load is applied as the fastening axial force. Since the contact area between the rolling element and raceway ring is very small, it is necessary to make the mesh size sufficiently small in order to conduct accurate calculations with FEA, which requires large-scale and time-consuming calculations. In this case, the analysis method is Full-FEA. It is generally known that the contact between the rolling element (sphere) and raceway ring (curved surface) is in the formulated Hertz contact state. Furthermore, when a load is applied to the hub unit bearing, the rigidity becomes complicated and non-linear due to changes in the contact angle between the rolling element and raceway surface as well as changes in the load zone range. Therefore, we incorporated BRAIN (Bearing Analysis In NSK)[5], a software originally developed by NSK based on the Hertz contact theory, into Abaqus as a user subroutine, eliminating the need for the fine mesh of the contact portion, which was essential for Full-FEA. At the same time, we constructed a coupled analysis method that is able to consider highly accurate non-linear rigidity. This method is called Usub-FEA.

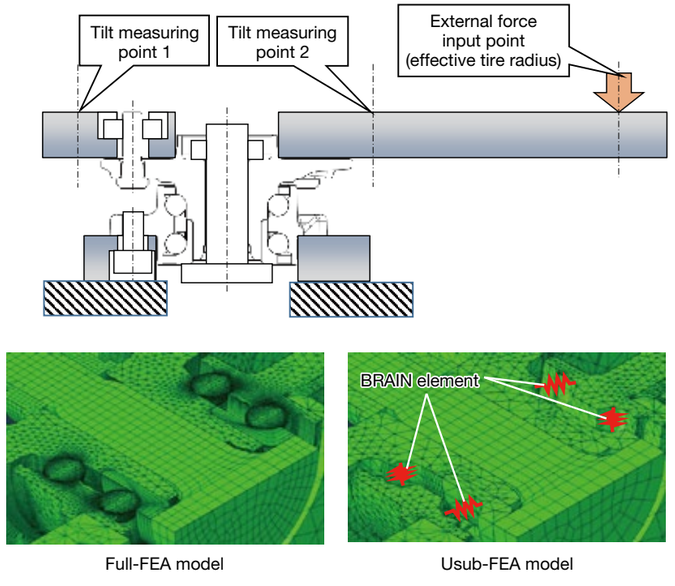

Fig. 6 Rigidity tester schematic and FEA model

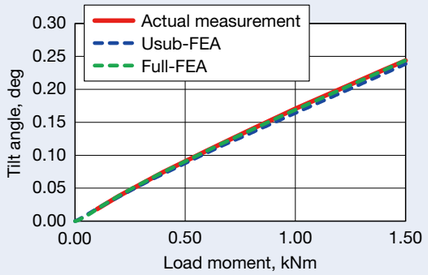

Fig. 7 Comparison of predicted rigidity and actual values

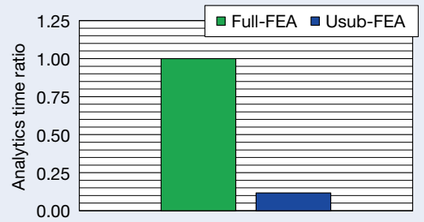

Fig. 8 Comparison of analysis time

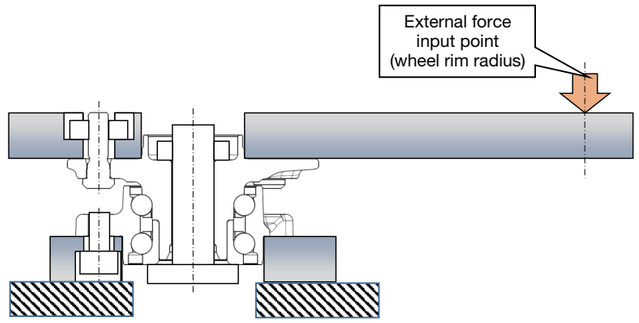

Fig. 9 Schematic for reproduction test indentation

Figure 7 shows a comparison of the predicted and measured values of rigidity. The predicted values obtained by analysis showed the same tendency as the actual measurement for both Full-FEA and Usub-FEA, and we found they had sufficient accuracy. Full-FEA has many nodal points on the raceway surface that transmit the contact load, has high contact rigidity and high reproducibility of the deformation of the raceway surface, and tends to be slightly more accurate than Usub-FEA. Figure 8 shows a comparison of the calculation time of both analytic methods. Since we did not have to reduce the mesh size for Usub-FEA to simulate the contact state, we could successfully reduce the model scale and thereby significantly reduce calculation time while maintaining analytic accuracy.

Since Usub-FEA can reduce the mesh size of rolling elements and raceway surfaces, it can be expanded easily to analysis, including peripheral vehicle parts such as wheels, brake disks, and knuckles, by using computational resources with spare capacity. We would like to apply this method to predictions of hub unit bearing performance when they are mounted on a vehicle, with the objective of developing hub unit bearings that can contribute to improving the dynamic performance of vehicles. Furthermore, although Full-FEA has the disadvantage of increased model scale, we plan to consider using it for applications other than rigidity prediction since it has higher analytic accuracy.

5. Example of Utilization of Full-FEA for Indentation Resistance Prediction

In real-world applications, excessive load may be input to the hub unit bearing due to a collision of the tire or wheel rim with a curb, contact between a pothole in the road and the tire, or any other accident. This may result in plastic deformation, called “indentation,” on the raceway surface. In many cases, the vehicle can run even after the indentation has occurred. However, when the rolling element revolves, it periodically collides with the indentation on the raceway surface, causing vibration and abnormal noise, which may make the driver feel uncomfortable. Furthermore, continuous use of hub unit bearings may lead to serious damage due to fatigue of the raceway surface starting from indentations. In general, we know that indentation resistance varies depending on design parameters such as the shape of the raceway ring, number and size of the rolling elements, and shape of the outer ring flange, in addition to the strength of the material. We must therefore study the indentation resistance of the external load assumed at the time of design.

Figure 9 is a schematic diagram of the indentation reproduction test. Figure 10 shows the state of the raceway surface with indentations measured using a roundness measuring instrument. Figure 10 indicates that the range and depth of indentation are different between the outer row of the vehicle and inner row of the vehicle. It can be assumed that the deformation of each part affects the formation of indentations when an excessive load is applied, so we calculated the load distribution of the rolling element using the Full-FEA method. Figure 11 compares the rolling element load distribution and deformation diagram of the outer ring between the outer row of the vehicle and inner row of the vehicle. In the inner row, the load zone of the rolling element overlaps with the range where the rigidity of the raceway ring is low, and the raceway surface is deformed into an elliptical shape. We can assume that the number of indentations increased as the load zone became wider due to the deformation of the raceway ring. From this result, we found that the use of Full-FEA could lead to optimization of the thickness design of the raceway ring based on indentation resistance.

In the future, by inputting the material strength distribution into this method, we will be able to make quantitative predictions of indentation shape.

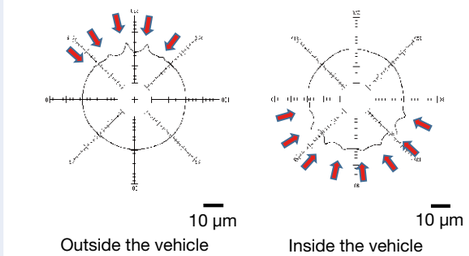

Fig. 10 Outer ring roundness measurements after the indentation test

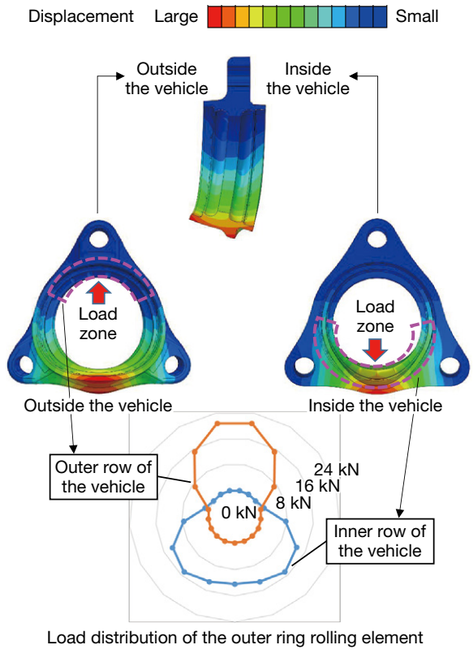

Fig. 11 Rolling element load distribution and deformation diagram of the outer ring

6. Example of Fatigue Strength Prediction of the Hub Flange

Since the hub unit bearing supports the vehicle, damage to it could cause an accident, so hub units must have high durability. In particular, the hub flange is fastened to the wheels and brakes, and repeated cyclic stress is input when the vehicle is running, so we need a highly reliable prediction of fatigue strength. For this reason, we make full use of FEA with wheels and brakes through Abaqus. Figure 12 shows the outline of the analytics model. Since the main damage factor is fatigue due to deformation (bending) of the hub flange with the wheel-fastening part as the fulcrum, which is caused by the external force transmitted from the tire, the scope of modeling includes not only the hub unit bearing but also the wheels and brakes. In addition, we set multiple rolling element load conditions in order to input repeated cyclic stress when the vehicle was running.

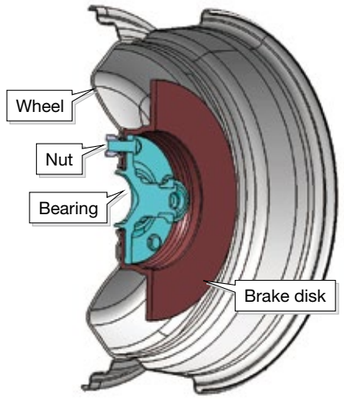

Fig. 12 Fatigue strength analysis model with wheel and brake[6]

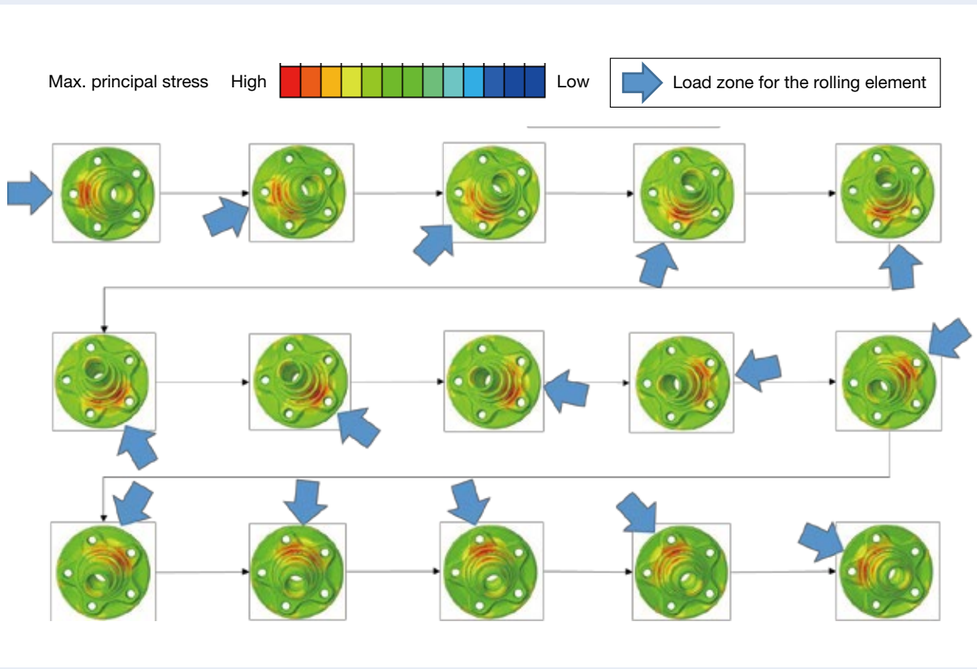

Fig. 13 Principal stress distribution at each load phase

Figure 13 shows the maximum principal stress distribution of the hub flange at each rolling element load phase. In addition to the function of assembling wheels and brakes, the hub flange has a different shape for each vehicle to ensure performance such as weight reduction and rigidity. For this reason, the weakest portion differs for each model, and it is necessary to comprehensively consider strength to input the rotational load.

After obtaining stress distribution under each load condition, we determined the fatigue durability by using the fatigue analysis software fe-safe[7] for post-processing. The hub flange has a turned finish surface and a forged finish surface, and different strength criteria are applied due to the difference in surface roughness. Figure 14 shows the weakest portion predicted by numerical analysis and the stained and observed photograph of fatigue cracks found in the penetrant inspection after the durability test. A series of numerical analyses made possible the prediction of damage at almost the same position as the actual machine. Fatigue damage is known to be affected not only by repeated cyclic stress but also by residual stress due to forging and heat treatment during the manufacturing of hub unit bearings. Considering these effects in terms of the analysis model, we would like to further improve the accuracy of strength prediction.

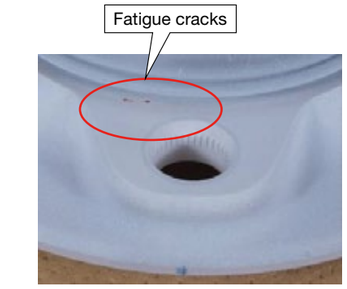

Observing fatigue cracks on the actual machine

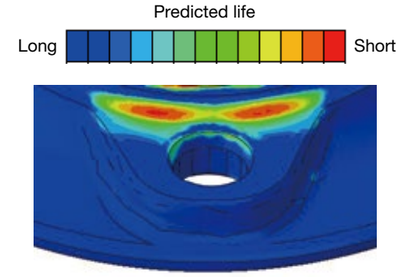

Predicted fatigue strength

Fig. 14 Damaged section of an actual bearing and predicted fatigue strength

7. Summary

We have introduced an example of DT application for hub unit bearings that uses recent improvements in computing power. Although we tend to avoid the use of nonlinear FEA in large-scale models for our designs as much as possible, from the viewpoint of calculation cost (calculation time) and modeling difficulty, we have found that it has many advantages.

The performance of computing servers and software that makes effective use of the servers is improving daily and, even if present analysis technology is difficult to use in regular design processes, it may become available with sufficient accuracy and at reasonable cost within a few years. In addition, even with commercially available analysis software, it is possible to significantly reduce analysis costs by customizing some models and coupling them with other methods, as Usub-FEA does. DT, which is based on highly reliable numerical analysis, is an indispensable technology for realizing our ultimate goal of streamlining processes, i.e., reducing the number of tests and evaluations. We will continue to promote technological development such as this from both a medium- and long-term perspective.

References

1) NSK Ltd., "Hub Unit Bearings," CAT. No. E4201b, 2007.
2) ISO281:2007
3) Scientific Forming Technologies Corporation, https://www.deform.com/
4) Dassault Systèmes, https://www.3ds.com/ja/products-services/simulia/products/abaqus/
5) H. Aramaki, "Rolling Bearing Analysis Program Package BRAIN," *Motion & Control*, No. 3, (1997), pp. 15–24.
6) T. Sakaguchi, "Recent Technical Trends in Hub Unit Bearings," *Motion & Control*, No. 29, (2018), pp. 43–50.
7) Dassault Systèmes, https://www.3ds.com/ja/products-services/simulia/products/fe-safe/

Hideo Nishizawa

Introduction of Analysis Method Automation Technology for Efficient Design

Yuki Uchiyama
Steering & Actuator Technology Center Steering Engineering Development Department
Richard Habermann
NSK Deutschland GmbH European Technology Center
Gergely Laszlo
Steering & Actuator Technology Center
Takashi Iwai
Steering & Actuator Technology Center Steering Engineering Development Department

Abstract

The finite element method (FEM) is an important verification process for structural analysis of mechanical design in a product development flow. With ever-advancing computer performance, it is becoming increasingly possible for large-scale, high-precision structural analyses to be performed in a short time. However, such complex analysis models increasingly require more staff hours to prepare. To achieve high-quality, low-cost design through structural analysis, programs have been developed to build analysis models automatically. Here, we will compare conventional methods with other analysis types and explore the potential labor-saving impact of this automation technology.

1. Foreword

Model-based development (MBD) is a product-system development method used with the aim of efficient product design by studying the feasibility of each design stage[1]. Computer-aided engineering (CAE) technology is indispensable for utilizing MBD, and both MBD and CAE use structural analysis (computer simulation) based on the finite element method (FEM) to verify the design feasibility of machine elements. Structural analysis for design studies requires high reproducibility of actual machines in order to prevent time-wasting rework in the mechanical design flow and thus reduce experimental costs.

To meet strong demand, the analysis model used for structural analysis tends to increase in scale and complexity year by year. However, even with such a large-scale analysis model, while it has become possible to perform calculations in a relatively short period due to recent improvements in computing power, there have been no innovative measures to reduce the amount of man hours required to construct an analysis model that addresses the increase in scale and complexity. Furthermore, the items studied through structural analysis in our design study process and the number of the items implemented have also increased annually.

There is a concern that such a situation may cause analytical work to bottleneck in the design study process. Therefore, we need measures to ensure that this process moves forward smoothly while avoiding an increase in the number of analysts in order to prevent increases in design cost.

Considering this situation, to improve the efficiency of design work, we have developed structural analysis, work-automation technology using computer programs for various analysis methods, mainly for electric power steering (EPS) products. In addition, with a view to the application of such technology in other fields, we have developed a program structure that is easily applicable at each technical site.

This article describes the background of the above automation technology's development, its technical features, and its operational effects.

2. Development Purpose

2.1 Current situation and analysis work problems

Substantial investments of time and money are typically needed in order to verify that automobile parts have been designed to satisfy specified safety, functionality, and durability requirements. MBD improves design efficiency by studying the validity of each design stage in advance, thereby limiting the occurrence of unexpected defects at the end of the design and the number of actual machine tests necessary to reduce costs.

In designing our steering products, we have been studying since the early 1990s the design through computer-based structural analysis. Since then, we have developed various analysis methods through correlation with the test results with the aim of improving the validity and machine reproducibility of such analysis results. The analysis methods we have developed to date cover each assembly component of the entire steering system (Figure 1).

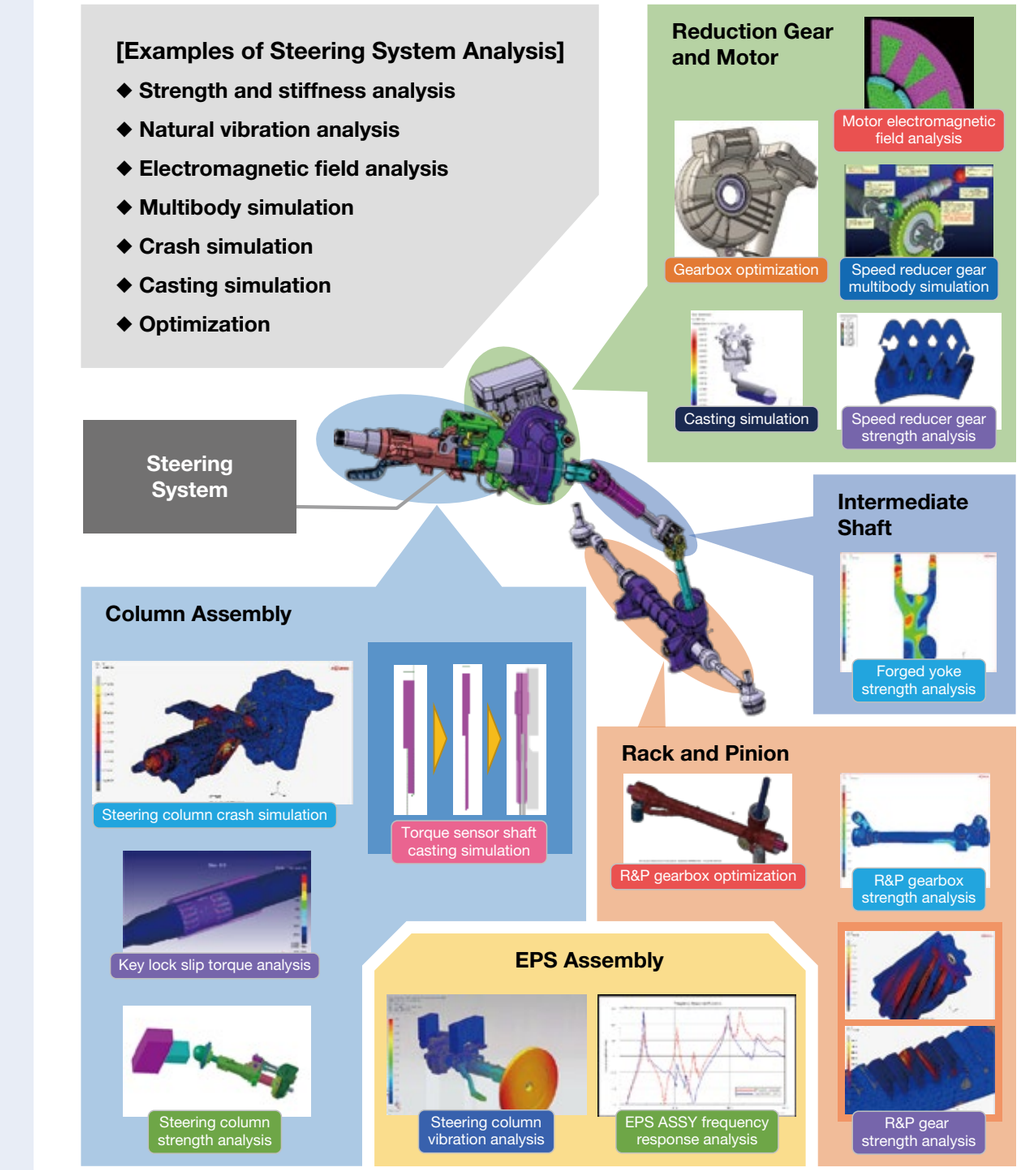

Fig. 1 Examples of steering system analysis

As an example of improving machine reproducibility, we have changed the method of studying a steering column assembly consisting of multiple parts from a simple linear analysis method to a non-linear analysis method with higher actual machine reproducibility. This is largely because non-linear analysis of assembly models, which used to take an enormous amount of time, can be calculated in a relatively short time now due to improvements in computing power and the development of parallel computing technology. Applying this non-linear analysis made it possible to define complicated conditions, thereby improving the analysis method's accuracy.

Currently, the development department is in charge of constructing and updating the new analysis method described above, and the design department uses this method for design study in each project. Utilization of the method requires specialized knowledge and experience regarding CAE and FEM, so the design department has a dedicated analysis specialist with whom the designer of each project consults throughout the design process. Due to increased demand for design study analysis, the workload of analysis specialists has increased in recent years. In addition, the analysis model of the development department's new method is increasing in scale and complexity, as mentioned above. The result has been an increase in the lead time until the designer completes the analysis request, which affects the progress and efficiency of the design study process (Figure 2).

For this reason, with the aim of improving the efficiency of design work by streamlining analysis, we have begun building an automatic analysis model-creation program.

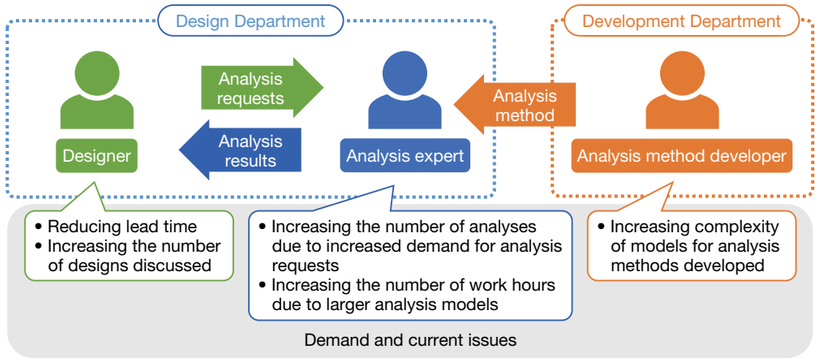

Fig. 2 Relationships between coordinators of analysis operations

2.2 Aggregation of the number of analyses implemented and selection of automation targets

Prior to the construction of automation technology, we identified the status of analysis and selected the targets to which the automation technology would be applied. Figure 3 shows a graph comparing the ratio of the number of analyses implemented, as classified by method.

According to the comparison of the number of analyses implemented, we applied the automation technology to steering column vibration analysis, steering column strength analysis, and rack and pinion gearbox strength analysis, which is the largest number of analyses implemented. In addition, we have prioritized rack and pinion gear strength analysis, which requires only a small number of analyses, although it has a large number of parts and requires a complicated analysis model. We have also prioritized steering column crash simulation. We have already applied automation technology to the former, and we plan to apply it to the latter in the future. Conversely, other component analyses have a small number of parts, so they require limited man hours to create the analysis model, which is why we decided not to apply the technology to those types of analyses for this study.

2.3 Changes in workflow with automation technology

The procedure for executing structural analysis using FEM is generally uniform regardless of the purpose of the analysis and target assembly component. Figure 4 shows the analysis workflow, taking steering column strength analysis as an example.

In this workflow, the items that require extensive man hours are "Modify a CAD model," "Create a mesh model," "Set analysis conditions," and "Process/Report analysis results." Of these, we developed automation technology to reduce man hours for "Create a mesh model" and "Set analysis conditions" because we can automate these two processes by constructing an analysis model generation program that uses the application programming interface (API) of the analysis software. On the contrary, we excluded "Modify a CAD model" and "Process/Report analysis results" from recent automation technology development because we decided that automation of these processes would be difficult due to changes in the parts configuration and the required reporting format for each project.

Figure 5 shows the changes in the workflow from "Modify a CAD model" to "Perform analysis" resulting from the application of automation technology.

By applying automation technology, we replaced "Create a mesh model" and "Set analysis conditions" with "Create a setting file," which defines all the conditions of the mesh and analysis models as a text file, and "Run a program," which automatically generates the analysis model. This reduces the number of processes and man hours and thus reduces the workload required to construct a structural analysis model.

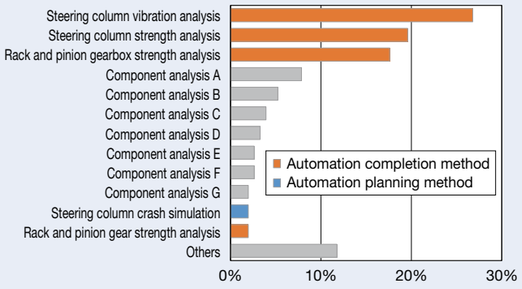

Fig. 3 Ratio of implementation for each analysis method

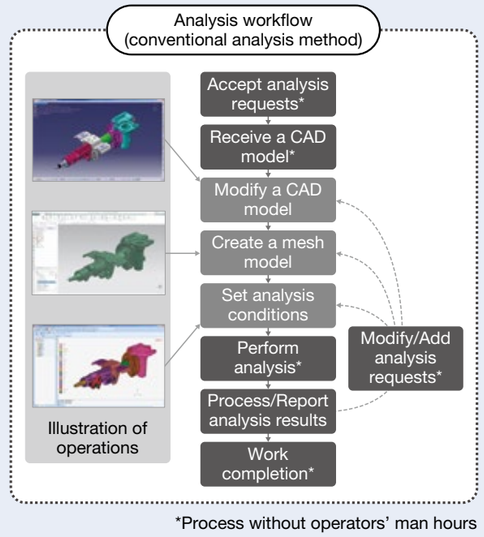

Fig. 4 Analysis workflow for steering products

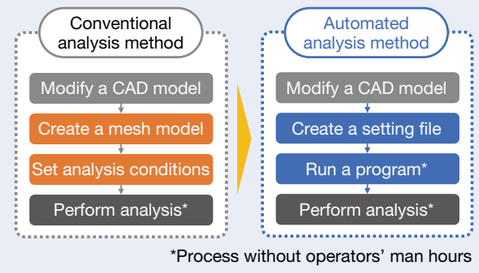

Fig. 5 Changes in workflow with automation technology

3. Development of Automation Technology

3.1 Overview of automation technology

We developed a method that automatically creates an analysis model with a program for every product at each of our technical sites. This was in an attempt to mutually utilize the automation technology specialized in the products and the analysis methods held by each base.

Regarding the operation of the program, we developed it based on the process of automatically creating a model with Dassault Systèmes' finite element method analysis software Abaqus™ based on Dassault Systèmes' CATIA™ format CAD model and text-based configuration files.

In addition, to further improve development efficiency, we created a program that enables engineers at each site to utilize automation technology independently while supporting products and analysis methods that related technical sites manage.

3.2 Development of the automatic analysis model creation program

When developing the new automation technology, we focused on securing extensibility of functions and maintainability.

As in the past, when each technical site performs its own automation development, it is difficult to efficiently add or expand functions by sharing program information because the individual sites have different implementation formats and program configurations. On the other hand, by unifying the implementation formats and sharing them within a single program code, we can improve the above-mentioned extensibility. However, since the individual sites handle different products, it is difficult to determine whether the program works properly for products that are out of scope of a site after we modify the program. Furthermore, as development progresses and the number of applicable products increases, there is a risk of increases in the number of test items associated with a program that could decrease maintainability (Figure 6).

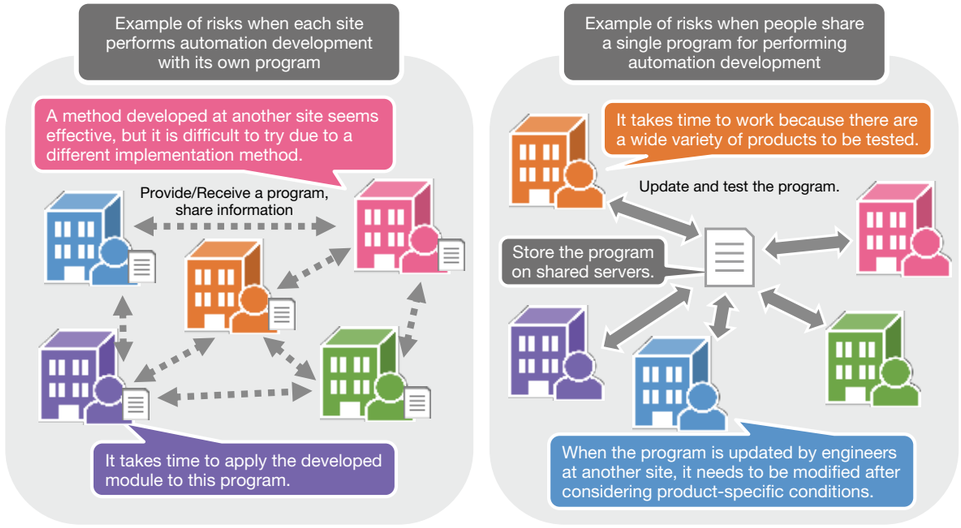

Fig. 6 Expected problems when collaborating in the development of automation programs

We need to avoid such problems and develop an automation program with excellent process extensibility and maintainability while supporting various products and analysis methods. To achieve this, we developed our own software framework, the objective of which is to define a procedure that divides the analysis model construction process for each function, then combine procedures appropriately for each product and analysis method to form a distribution, i.e., a series of processes.

Below are the details of the framework. Each procedure's program is composed of roughly two subprograms. One is modeling processing, which describes the processing contents for creating an analysis model, and the other is config definition, which acquires the values necessary for model processing. In the config definition, we describe the data type, definitions of options, and dependency related to the value established in the configuration file. Unifying the method of defining the input values used in the procedure will improve the readability of the program and smoothly promote development of the graphical user interface (GUI), which we will describe later. In the modeling process, we describe the analysis model process executed in the procedure. Here, it is desirable that the execution range of one modeling process is composed of the smallest units and loosely coupled to other procedures when we divide each stage of analysis model creation. We combine these divided-function procedures as a distribution to form a series of automatic analysis model creation programs. Engineers familiar with each product and analysis method can create a distribution and check the operation to evaluate whether the analysis model is generating correctly and automatically.

By developing automation technology according to this framework, we obtain two advantages. First, it becomes easier to apply newly developed procedures since when we create a procedure, we can confirm its effectiveness easily by replacing it with a procedure with the same function in an existing distribution and checking its operation. Second, it limited the requirement for operation checks associated with program changes since we can perform the operation check for each distribution, and when we change the program (procedure), workers do not need to check the application to products other than the products or analysis methods that they manage. This will make it easier to conduct maintenance work associated with function additions and bug fixes (Figure 7).

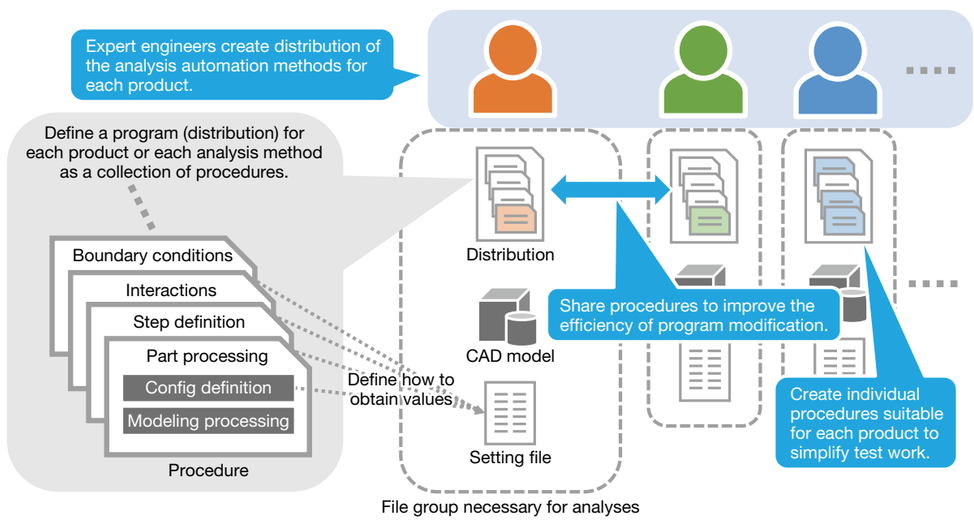

Fig. 7 Illustration of the framework structure and relationships between automated analysis methods

Here, regarding completed development of steering column strength analysis, steering column vibration analysis, and rack and pinion gearbox strength analysis, we will explain the advantages of constructing automation technology having this framework by using the created distribution as an example. Compared to steering column strength analysis, the distribution of steering column vibration analysis has different procedures except for part processing, reference point creation, and job setting, i.e., it is mostly composed of newly created procedures. For this reason, the man hours for maintenance such as bug fixing will increase somewhat, but since test calculations at the time of program changes only need to be performed through vibration analysis, we can efficiently implement program improvement. On the other hand, the distribution configuration of rack and pinion gearbox strength analysis is common except for the procedure for reading the gear specifications, so even if we find a bug in the program of the common procedure, we can make the correction in one operation, which facilitates maintenance work (Figure 8).

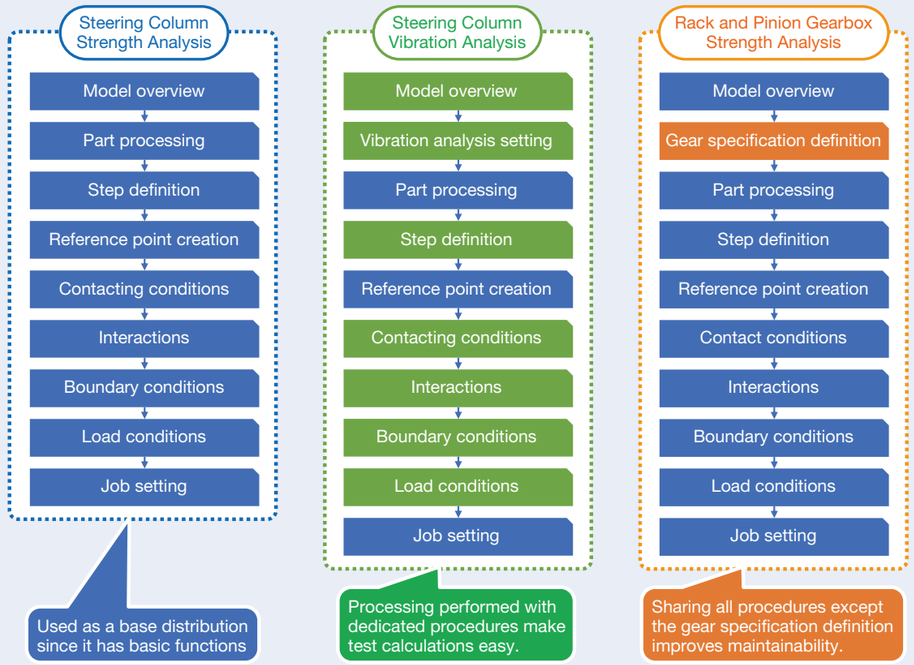

Fig. 8 Procedure structure and characteristics for automated analysis methods

3.3 Development of the operator support GUI

We can automate analysis model construction by using the above-mentioned automation program, but there remains a problem with creating a configuration file that describes the conditions of the analysis model. To do so, the operator must create a configuration file that describes the analysis conditions before running the program and, in the case of a configuration file for a large-scale model, the operator must create condition settings with more than 1 000 lines as a text file. Therefore, unless we improve efficiency, we might not be able to maximize the effects of automation due to an increase in the work hours until the execution of the program and rework caused by description errors in text files.

To solve this problem, in parallel with the development of the analysis model construction program, we developed an operator support GUI, which creates configuration files efficiently and quickly.

The role of the GUI is to support the operator in creating an appropriate configuration file. In order for us to select and describe the input values for each procedure, we have improved work efficiency by constructing an input form with radio buttons and pull-down menus on a general settings window. In addition, we created the GUI so users can automatically read the config definition in the procedure and reflect it in the input form so that the GUI can support input the format that changes for each procedure, making it universally available, even for new procedures. With the GUI, we can efficiently create configuration files that reduce the frequency of mistakes (Figure 9).

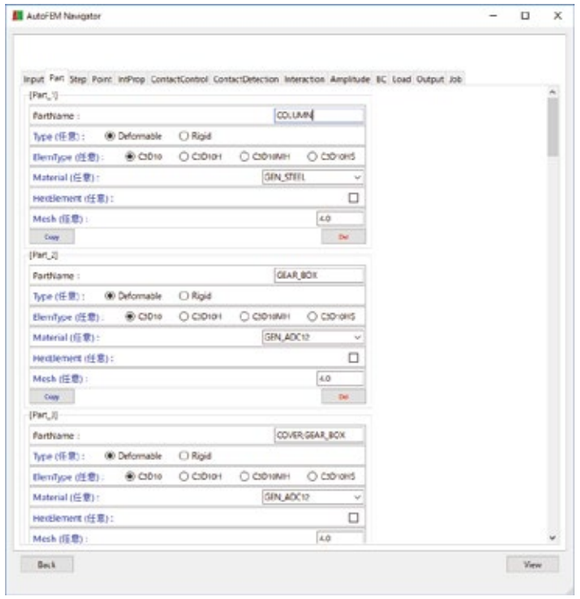

Fig. 9 General settings window in operator support GUI

In addition, more than half of the descriptions of the created setting files are the “parts” settings imported from a CAD model and the “interaction characteristics” settings that define the contact conditions between parts. To reduce man hours, we created individual condition setting screens for these two settings.

When setting parts, users read part information from the assembly file, then the screen for setting the material characteristics and mesh size of individual parts. The setting screen for parts makes it possible to set all the parts used for analyses in a single list and to enter conditions more quickly and reliably than in the general settings window mentioned above. Similarly, the interaction characteristic setting screen makes it possible to set the interaction characteristics, such as contact and inter-part coupling, in a single list based on the clearance information between parts detected on CAD in advance (Figure 10).

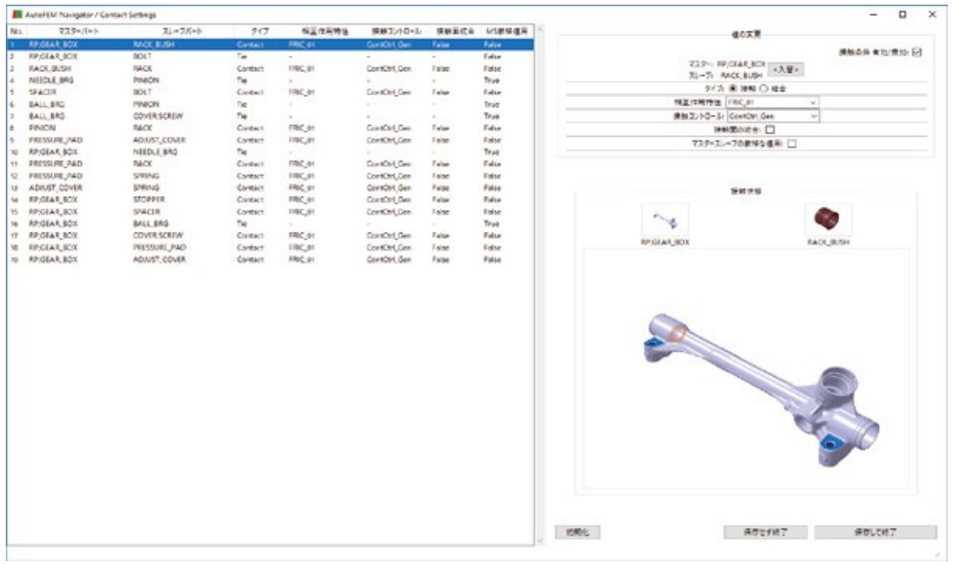

Fig. 10 Support GUI window for definitions of interaction properties

3.4 Example of the automated analysis methods we have developed

Below are the features of the automated analysis methods that we have developed so far.

(1) Steering column strength analysis

This is a strength verification method for each load condition of the steering column, which is the main product we have developed. Since it has been carried out as strength analysis of each assembly under many products and load conditions, we applied the automation technology to this development first.

A steering column assembly consists of nearly 100 parts, of which about 20 to 30 are used in strength analysis. In the past, we created meshes and set material properties for each of these CAD models, manually defining contact and boundary conditions between parts. Constructing a model this way required far more man hours than doing component analysis with a small number of parts, but now we can reduce the workload significantly with the application of automation technology. Regarding the automated analysis method for steering column strength analysis, we investigated the operational effect, and the results are described in 3.5 “Investigation of operation performance” below.

(2) Steering column vibration analysis

For the sound and vibration performance of steering products, the number of those with post-shipment defects is high. In recent years, we have implemented the highest number of analyses ever due to the increased demand for preliminary analysis studies. The new method’s key feature is that we perform the analysis using a two-step procedure. First, we check the contact state between parts by analyzing the lock state of the handle position adjustment lever. Second, we consider the results in the vibration analysis model. This requires us to create two types of analysis models to check the vibration performance, requiring a lot of man hours.

To solve this problem, we applied the automation technology to steering column vibration analysis, which requires reproduction of the inertia and weight of parts, so the number of parts and the model construction man hours tend to be high compared to strength analysis. In contrast, the automation technology has a greater man-hour reduction effect since it handles a larger number of parts, so it significantly reduces man hours when applied to vibration analysis. It further reduces workload by forming a program that automatically reflects the coupling range of the contact part caused by lever lock state analysis (Figure 11).

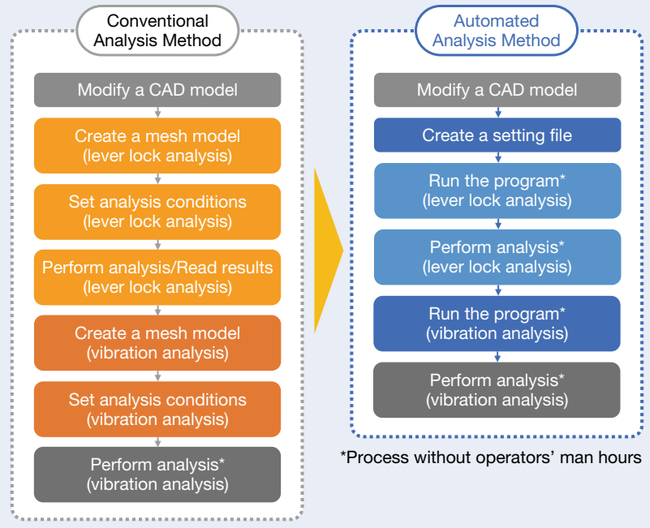

Fig. 11 Changes in workflow for steering column vibration analysis with automation technology

(3) Rack and pinion gearbox strength analysis

The functions required to automate the analysis method for rack and pinion are almost the same as those for the above-mentioned steering column strength analysis. The difference is that the correct gear shape needs to be imported to reproduce the engagement of the rack and pinion gear in detail. To deal with this, in collaboration with our specialized rack and pinion development department, we introduced a system that automatically creates CAD and mesh models of gear shapes with high accuracy, which has enabled automatic import of gear shape models that simulate the actual engagement state from the gear specification information, thereby achieving further efficiency improvement. We also use this function for automation of rack and pinion gear strength analysis.

Our steering department plans to strengthen the supply of pinion type EPS and is promoting the development of dual-pinion EP, so the importance of this method is expected to increase in the future.

3.5 Investigation of operation performance

Regarding the automated analysis method for steering column strength analysis that we developed, our design department investigated the effect of automation when operating it in an actual project. As a result of eliminating the processes of "Create a mesh model" and "Set analysis conditions," they achieved a significant reduction in man hours as an actual value (Figure 12).

Since we conducted this investigation of the operation in the earliest stage of automation development, the above-mentioned GUI function was incomplete since the operators were not proficient in CAD operations peculiar to the automation technology. We expect that the man-hour reduction effect of the automation technology will improve further once the operators are more familiar with CAD operations and significantly improved GUI function as the operation continues in the future.

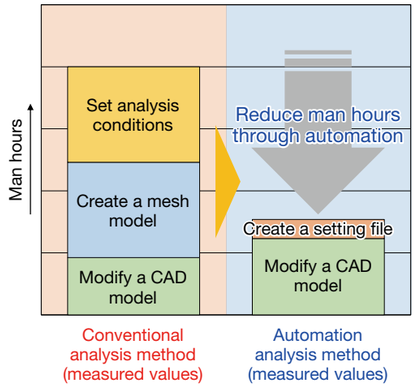

Fig. 12 Operational results for steering column strength analysis with automation technology

4. Afterword

Here we introduced automation technology that improves the efficiency of structural analysis work in the design study process. Also, we described the investigation results of the operation performance.

In the future, along with the expansion of the analysis method that will be the scope of application, we will promote the standardization of program specifications and the updating process so that each technical site can continue to utilize common automation technology. In the long term, we will fully automate the existing analysis workflow by means of CAD model recognition utilizing artificial intelligence (AI) and GUI function expansion, so that analysis specialists can concentrate on more advanced work in our aim to create design processes of higher quality and lower cost.

Reference

1) S. Fujikawa, "Model Based Development in Mazda," *Mazda Technical Review*, No. 31 (2013), pp. 44–47.


Yuki Uchiyama


Richard Habermann

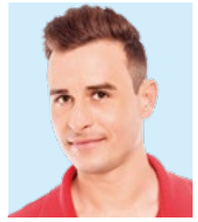
Gergely Laszlo


Takashi Iwai

Estimation of Noise Radiation Including Airborne Noise Using the In-situ Blocked Force Approach (Third Report, Experimental Verification of the Estimation Method by Application to Rattle Noise from an Electric Power Steering System)

Yoshihiro Sato
Technology Development Division Headquarters, Core Technology R&D Center, Technology Research & Development Office 3
Jan Hendrik Elm, Jens Viehöfer
Forschungsgesellschaft Kraftfahrwesen mbH Aachen
Jan-Welm Biermann
Institut für Kraftfahrzeuge, RWTH Aachen University
Nobuyuki Iwatsuki
Department of Mechanical Engineering, Tokyo institute of Technology

This article has been approved for reprint by the Japan Society of Mechanical Engineers, following preprints of the Transactions of the JSME Vol.86, No.891 (2020).

Abstract

In the previous reports, a methodology for estimating noise radiation including airborne noise from a mechanical system under the operational condition by component test of a certain active subsystem using the in-situ blocked force approach, which is normally used for estimating only structure borne noise, was proposed and verified by numerical simulations of noise radiation from a cantilever rectangular plate. This paper describes experimental verification of the proposed methodology by application to rattle noise from a column-type electric power steering system (EPS) for a vehicle. An EPS corresponds to the active subsystem, while other parts such as the vehicle body correspond to passive subsystems. At first, a method of measuring rattle noise from an EPS under the operational conditions, i.e., running tests with a vehicle, was established. Since it is possible to apply the in-situ blocked force approach also to vehicle running tests and to estimate rattle noise, the measured and estimated rattle noises under an identical operational condition were compared and validity of the proposed methodology was confirmed. Next, a component test bench that allows for the reproduction of the vibration behavior of an EPS under the operational conditions was developed, and rattle noise under an operational condition was estimated by means of the proposed methodology using both vibration accelerations measured with this component test bench and vibro-acoustic transfer functions measured with the vehicle under a static condition. Finally, the proposed methodology was verified by comparing the estimated and measured rattle noises under the operational condition. The proposed methodology is expected to replace time-consuming operational tests of a whole mechanical system to simple component tests of the active subsystem.

1. Introduction

Since multiple subsystems, which comprise a mechanical system, are developed concurrently, each subsystem is tested individually. However, when it comes to noise and vibration, in cases where there is strong interaction between subsystems, the entire mechanical system needs to be evaluated under the operational condition rather than evaluating the individual subsystems and, if the final performance does not meet the required specifications, the subsystem designs must be modified. Therefore, it is desirable that the noise and vibration of the entire mechanical system under the operational condition could be estimated at the subsystem development stage.

As an example of the case where noise of an entire mechanical system under the operational condition differs from that in the component test due to the interaction between subsystems, Figure 1 shows the results of comparing rattle noise from an electric power steering system (EPS) for automobiles. In this case, the actual operation test for the EPS requires a running test of a vehicle. By the EPS component test, external force was applied to the tie rod end with a vibration exciter so that the axial vibration acceleration under the vehicle running condition would be reproduced by trial and error. Details of the rattle noise measurement method, the vehicle running condition, and the EPS component test bench will be explained in the following chapters.

Figure 1 (a) shows the results of comparing the sound pressure level (JIS C 1509-1, time-weighted time constant 50 msec), while Figure 1 (b) shows the results of comparing the frequency spectra. In the component test, mean amplitude of the axial vibration acceleration of the tie rod was reproduced in the frequency domain, but phase was not considered. Thus the waveform of the sound pressure level is different in the time domain. However, not only the waveform but also the averaged sound pressure level shown in the legend is also different by about 7 dB (A). Although this difference could result from the low reproducibility of the axial vibration acceleration of the tie rod on the EPS, differences in support structure and vibration characteristics of the EPS between the vehicle and the component test bench are also factors. Therefore, even if the rattle noise measured by the component test bench at the EPS development stage is within the specified value, it may fail in the final running test of the vehicle and require modifications in the EPS design. To prevent this, at the EPS development stage

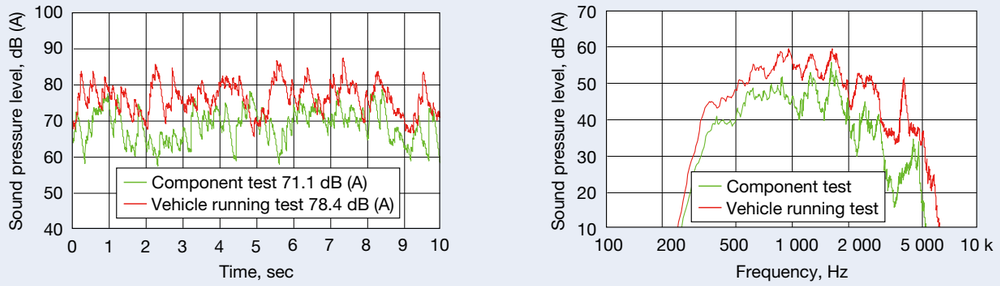

(a) Time waveforms of sound pressure level (TC = 50 ms)

(b) Frequency spectra of sound pressure level

Fig. 1 Measured sound pressure levels corresponding to rattle noises from an EPS extracted by both A-weighting filter and a band-pass filter from 300 Hz to 5 kHz by component test and by vehicle running test.

the sound pressure level of the rattle noise during vehicle operation needs to be estimated.

To estimate the sound pressure level of a mechanical system under the operational condition by the component test of the subsystem, the in-situ blocked force approach[2, 10] could be employed, with which blocked force[4], unique to the subsystem and not dependent on the support structure, can be identified. Therefore, the same blocked force as in the operational condition of the entire mechanical system can be identified by the component test of the subsystem using this method. By obtaining the transfer function of the target sound pressure (hereinafter the "vibro-acoustic transfer function") of the entire mechanical system in advance, the sound pressure level of the entire mechanical system under the operational condition is possible to be estimated through multiplying the function by the blocked force identified by the component test of the subsystem. At the subsystem development stage, it is impossible to obtain such a vibro-acoustic transfer function since the other subsystems are also in development and not available. However, we could estimate the sound pressure level approximately by substituting the vibro-acoustic transfer function of other existing mechanical systems with similar vibration characteristics. For cases in which the mechanical system already exists, the sound pressure level of the entire mechanical system under the operational condition could be evaluated by the component test of the subsystem without a time-consuming operation test of the entire mechanical system.

As described above, by using the in-situ blocked force approach, the sound pressure level of the entire mechanical system could be estimated by the component test of the subsystem. However, since this method is for structure-borne noise and cannot be applied when the required sound pressure level includes airborne noise[3, 6]. When the entire mechanical system is divided into two subsystems, one includes the vibration sources (hereinafter the "active subsystem"), and vibration of the vibration sources is transferred to the other subsystem (hereinafter the "passive subsystem"). Airborne noise is radiated directly from the active subsystem, whereas structure-borne noise is radiated from the passive subsystem. In the case of the above-mentioned rattle noise, since the EPS is an active subsystem, it radiates airborne noise, whereas the vehicle body structure radiates structure-borne noise, i.e., it is a passive subsystem. Regardless, both structure-borne and airborne noise must be included no matter where in the vehicle interior the sound pressure is measured, and it is difficult to exclude only airborne noise when measuring sound pressure. In addition, even if the S/N ratio of the rattle noise is improved by using a measurement method in which airborne noise is dominant, the advantage of such a measurement method cannot be taken in the application of the in-situ blocked force approach.

In this study, we examined a case where airborne noise was included in the sound pressure level estimated using the in-situ blocked force approach and found that the estimation error at the natural frequencies of the mechanical system became smaller. Based on this result, in cases where the natural frequency component is dominant, we proposed to estimate the sound pressure level including airborne noise by using the in-situ blocked force approach and verified its effectiveness by means of a simple model with the 3 degrees of freedom model[11]. Next, we verified its effectiveness by numerical simulation of noise radiation from a cantilever rectangular plate, which is a high-order, multiple-degree-of-freedom model, and proposed a method to reduce the estimation error[12].

In this report, we describe the results of the experimental verification of the estimation method by application to rattle noise from an EPS. Since the rattle noise results from collisions between the parts inside the EPS, the EPS is an active subsystem, whereas the vehicle body structure (other than the EPS or the frame structure of the component test bench) is a passive subsystem. We will describe the details in the next chapter, but the measured rattle noise was dominated by airborne noise radiated directly from the EPS. Since the purpose of this study is to estimate the sound pressure level including the airborne noise of the entire mechanical system under the operational condition by the component test of the active subsystem, we identified the blocked force by the EPS component test, estimated the rattle noise by multiplying it by the vibro-acoustic transfer function of the vehicle, and verified the estimation method by comparing it with the measured rattle noise under the vehicle running condition. In addition, as mentioned above, since we could identify the blocked force of the EPS by the vehicle running test, we also verified the estimation method with the blocked force identified by the vehicle running test.

When identifying the blocked force by the vehicle running test, we measured first (as shown in Figure 2 (b)) the vibro-acoustic transfer function of the rattle noise and the inertance to each vibration measurement point of a stationary vehicle by impulse excitation. Next, as shown in Figure 2 (a), we measured the rattle noise while the vehicle was running; that is, the operational condition of the EPS, and as shown in Figure 2 (c), identified the blocked force by using the measured inertance and the vibration acceleration of the EPS measured at the same time with the vehicle running test. Then, using Transfer Path Analysis (TPA)[1] formulations, we estimated the rattle noise generated during vehicle operation and compared it with the measured noise. The sound pressure level of the estimated rattle noise was higher than that of the measured noise, but the time waveform of the sound pressure level was almost the same, so we could successfully verify the validity of the estimation method. Also, in the case of identifying the blocked force by the EPS component test, we measured the vibration acceleration of the EPS by applying external force with a vibration exciter, reproducing the axial vibration acceleration of the tie rod during vehicle operation, as shown in Figure 2 (d). Since the reproduction accuracy of the tie rod axial vibration acceleration was low, the estimated time waveform and spectral shape of the rattle noise differed from those measured, but the averaged sound pressure level was almost the same, meaning that we could verify the estimation method quantitatively. We will explain the details of these verification experiments in the following chapters.

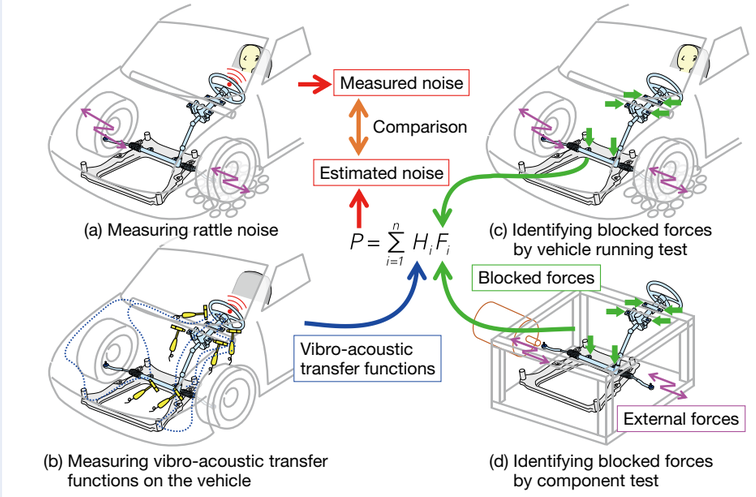

Fig. 2 Schematic view of two experimental verifications for the noise estimation method. One way is identifying blocked forces by vehicle running test and the other is identifying blocked forces by component test.

2. Characteristics, Measurement Method, and Generation Mechanism of the Rattle Noise

2.1 Rattle noise characteristics, measurement method, and vehicle running-test conditions

EPS rattle noise results from collisions between parts, which are especially common when the vehicle is running along uneven, rough roads. The sound pressure level of EPS rattle noise is usually performed by subjective rating of test drivers at the final inspection of a vehicle running test. Generally, test drivers can identify EPS rattle noise from other noise (e.g., engine and road noise), but since that the sound pressure level of EPS rattle noise is lower compared to other noise, it is difficult to extract the rattle noise component from the sound pressure when measured by a microphone installed near the driver's

Fig. 3 Microphone mounted at the steering wheel center from which the airbag module has been removed

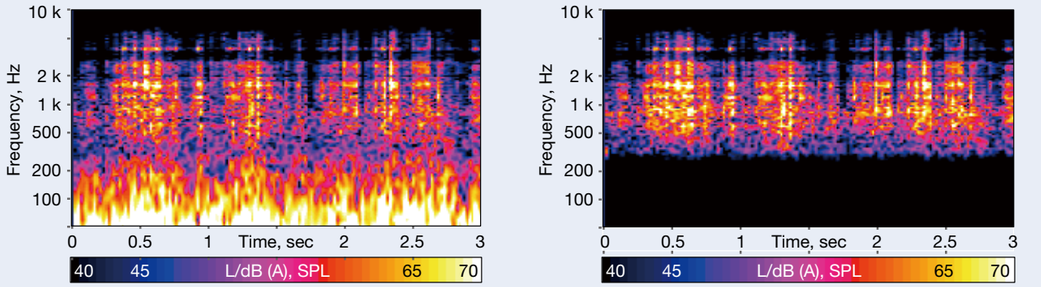

(a) Original sound

(b) Rattle noise component extracted by a band-pass filter

Fig. 4 Time-frequency spectra of the sound pressure measured by a microphone at the steering wheel center under a vehicle running test on the cobble road at 15 km/h

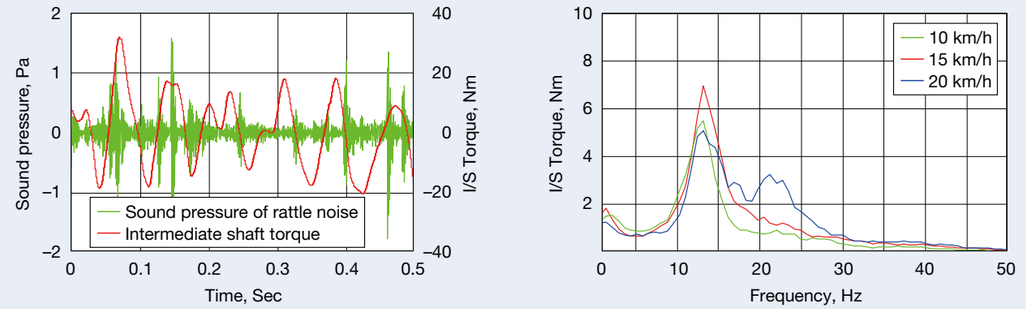

(a) Sound pressure of EPS rattle noise and I/S torque

(b) Frequency spectra of I/S torques

Fig. 6 Left figure (a) indicates sound pressure corresponding to EPS rattle noise extracted by both A-weighting filter and a band-pass filter from 300 Hz to 5 kHz and I/S torque measured by vehicle running test on the cobble road at 15 km/h. Right figure (b) indicates frequency spectra of I/S torques measured by vehicle running test on the cobble road at 10, 15, and 20 km/h.

ear. To evaluate rattle noise both quantitatively and automatically, it is essential to extract the rattle noise component from the sound pressure. After trial and error regarding the installation position of a microphone, we improved the S/N ratio of the rattle noise component by installing a microphone near the center of the steering wheel, from which the airbag module was removed, as shown in Figure 3. Figure 4 (a) shows the results of analyzing the sound pressure measured in this way using STFT. The horizontal axis indicates time, the vertical axis indicates frequency, and the color indicates magnitude of the sound pressure level. By extracting the high-frequency band with a band-pass filter of 300 to 5 000 Hz, as shown in Figure 4 (b), only the rattle noise component becomes audible. Based on this, we decided to evaluate the signal as the rattle noise component, in which we extracted the band of 300 to 5 000 Hz with a band-pass filter and an A-characteristic filter from the sound pressure measured by the microphone installed, as shown in Figure 3. Airborne noise radiating directly from the EPS dominates the rattle noise, but it also includes a small amount of structure-borne noise radiated from the vehicle body. Incidentally, we performed all-vehicle running tests to measure the rattle noise on a cobble road (a bumpy test course with numerous rounded stones, irregularly embedded) at the Ford Lommel Proving Ground (https://www.fordlpg.com/en/) at a speed of 15 km/h (where rattle noise is most audible).

2.2 Rattle noise generation mechanism and excitation method in the EPS component test bench

In the column-type EPS covered by this report, steering force input from the steering wheel is assisted by the motor, which is decelerated by the worm wheel and transferred to the tires via the intermediate shaft and rack and pinion. However, when the vehicle runs on cobble roads, the reverse input load from the tires transfers to each machine element, resulting in rattling due to the collisions between parts, as shown in Figure 5. Therefore, we must reproduce the collisions between parts, i.e., the direct cause of the rattle noise, in EPS component tests. The collisions between parts occur because of the reverse input load from the tires, as an alternative to the reverse input load, we measured torque of the intermediate shaft during rattle noise generation. Figure 6 (a) shows the measurement results, in which the rattle noise occurs at the moment when the intermediate shaft torque reverses or increases. Figure 6 (b) shows frequency spectra of the intermediate shaft torque measured by changing vehicle speed. Since the frequency at the dominant peak near 13 Hz does not change, regardless of vehicle speed, that could be the natural frequency of the chassis system. Therefore, a rattle noise generation mechanism could be as follows: low-frequency resonance (about 13 Hz) with reverse input load from the tires generates the collision between parts and, as a result, high-frequency vibration (300 to 5 000 Hz) occurs and is transferred to each structures, while sound radiates from parts including flat surfaces such as the steering wheel. Due to low-frequency resonance, the tires move both in the vertical and steering-angle direction, but the steering-angle direction is dominant with respect to the rattle noise according to the vehicle vibration test shown in the Appendix. When a vehicle runs on a cobble road, the reverse input load is so large that the steering wheel cannot be fixed by hand even when traveling straight, so the tires move in the steering-angle direction since they are moving diagonally across the cobblestones. In the EPS component test bench, we reproduced the collision between the parts by vibrating the tie rod in the axial direction at low frequencies since low-frequency resonance is an indirect cause of rattle noise. Since we set the vibration frequency to 100 Hz or less, it did not overlap with the frequency band of rattle noise (300 to 5 000 Hz), and forced vibration from a vibration exciter did not cause a problem.

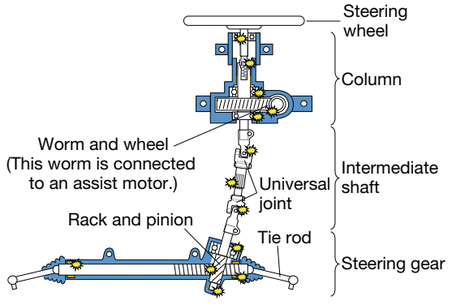

Fig. 5 Schematic view of a column-type EPS in which yellow marks indicate potential sources of rattle impacts

3. Verification When Identifying Blocked Force by the Vehicle Running Test

3.1 TPA model for estimating rattle noise

As shown in Figure 2, in this study we estimated rattle noise under the vehicle running condition by using blocked forces and vibro-acoustic transfer functions as the TPA input. This section describes the method of identifying the blocked force by the vehicle running test, the method of measuring the vibro-acoustic transfer function of the vehicle, the positions and mounting methods of the required sensors, and related matters.

In this study, the EPS is as an active subsystem, thus the blocked force is defined as the force to completely fix the EPS connection. But the blocked force was indirectly identified by the in-situ blocked force approach and the vibration measured in the running test of the entire vehicle including the EPS. Specifically, we calculated the blocked force using the inverse matrix method shown in Equation (1)[11].

$$[G]^{+}=\left(\left[[U][S][V]^{*}\right)^{+}=\left(\left[U\right]\begin{bmatrix}\sigma_1 & 0 & \cdots & 0\\ 0 & \sigma_2 & & \vdots\\ \vdots & & \ddots & 0\\ 0 & \cdots & 0 & \sigma_N\\ 0 & & & 0\\ \vdots & & & \vdots\\ 0 & \cdots & \cdots & 0\end{bmatrix}\left[V\right]^{*}\right)^{+}=\left[V\right]\begin{bmatrix}1/\sigma_1 & 0 & \cdots & 0 & 0 & \cdots & 0\\ 0 & 1/\sigma_2 & & \vdots & & & \vdots\\ \vdots & & \ddots & 0 & & & \vdots\\ 0 & \cdots & 0 & 1/\sigma_N & 0 & \cdots & 0\end{bmatrix}\left[U\right]^{*} \quad \cdots\cdots\cdots (2)$$

$$\left\{f_{\mathrm{bl}}\right\}=\left[G\right]^{+}\left\{A\right\} \quad \cdots\cdots\cdots (1)$$

Where {*A*} is the vibration accelerations of the reference points when the vehicle is running, [*G*] is the inertance matrix from the EPS connections to the reference points, and + is the pseudo-inverse matrix. Although the inertance is a frequency spectrum, we treated the vibration acceleration as a time waveform, so the blocked force was identified in the time domain by convolution of these[13]. In addition, we calculated the pseudo inverse of the inertance matrix $[G]^{+}$ by using the singular value decomposition shown in Equation (2) for each frequency, as in the previous report[12].

We set the EPS connections to the six reference points indicated by the green circles in Figure 7 (four at the column, and two at the steering gear), and the additional reference points to the seven indicated by the red circles in Figure 7 (four at the connection between the subframe and the steering gear, and three on the EPS) in addition to the EPS connections. This is because, in the determination of force by the inverse matrix method, the measurement error could be reduced by setting the same number (or more) of the additional reference points as the number of the reference point[9]. The tie rod ends at both sides are also EPS connections, but in this study, we did not consider the blocked force of the tie rod ends for two reasons: first, since the tie rod ends are far from the center of the steering wheel (where we measure the target sound pressure), we assumed that its influence would be minimal; second, because it was difficult to identify the blocked force when one of the tie rod ends was free in the EPS component test bench described later in this report. Incidentally, as described in the previous report[11], the vibration behavior under the actual EPS operating state (i.e., the running state of the entire vehicle) is equivalent to that under the equivalent vibration state (i.e., the state where the blocked force is applied to the EPS connection) in a passive subsystem (i.e., the vehicle body structure not including the EPS), but not in the active subsystem (EPS). Thus, in principle, we should place the additional reference points only on the vehicle body structure, not on the EPS. In this study, however, since the vibration behavior of the active subsystem under the actual operating state is approximately equivalent to that under the equivalent vibration state when the natural frequency is dominant, we placed the additional reference points also on the active subsystem (EPS).

For the blocked force and vibration of the reference points, we considered the three orthogonal directions of XYZ shown in Figure 7 for each location; the number of blocked forces is 6 × 3 = 18, the number of vibrations at the reference points is (6 + 7) × 3 = 39, and the number of inertances is 18 × 39 = 702. Since inertance measurement required impulse excitation of the EPS connection in three orthogonal directions of XYZ, we attached an aluminum piece with planes in the vertical and horizontal directions near the EPS connection and used it as the excitation point, as shown in Figure 8. However, in the -X direction (in the rear direction of the vehicle) of the steering-gear housing connection shown in Figure 8 (b), we could not generate vibration up to the high-frequency band where rattle noise was distributed, so as an alternative, we excited the neighboring subframes. In the case of a mechanical system containing backlash such as EPS, the best way to obtain the vibro-acoustic transfer function is applying random excitation and averaging such vibration by using a vibration exciter. However, because of a small space near the EPS connection, it was not possible to install a vibration exciter, so with an awareness of potential errors due to the excitation method, we performed impulse excitation, with which we could obtain the vibro-acoustic transfer function with relative ease, even in a confined space. As shown in Figures 8 and 9, we measured the reference point vibration using triaxial accelerometers, and for parts where there is no plane in the vertical and horizontal directions at the sensor-

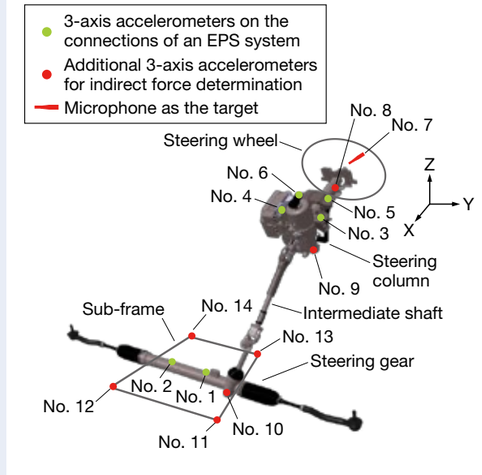

Fig. 7 Positions of 3-axis accelerometers and a microphone.

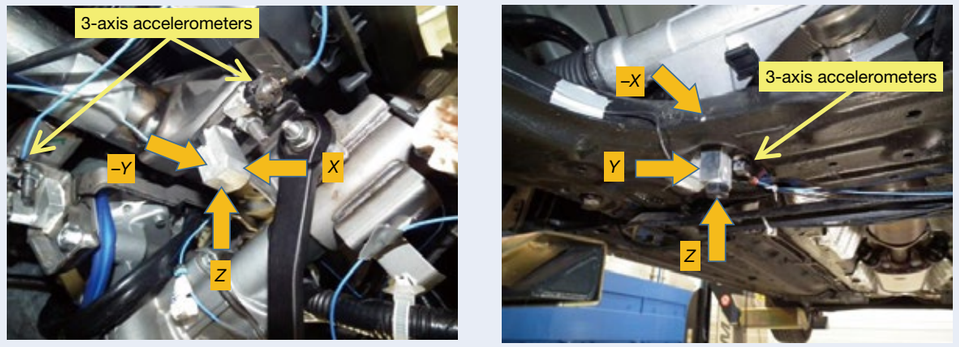

(a) Left-hand connection of the steering column (No. 3, 5)

(b) Right-hand connection of the steering gear housing (No. 2)

Fig. 8 Accelerometers on the connections of an EPS system in which hammering points are illustrated

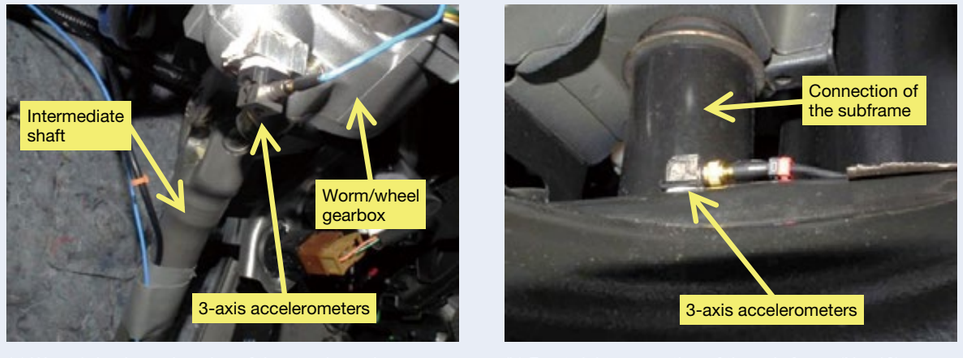

(a) Worm/wheel gear housing of the steering column (No. 9)

(b) Front-right connection of the sub-frame (No. 12)

Fig. 9 Additional 3-axis accelerometers

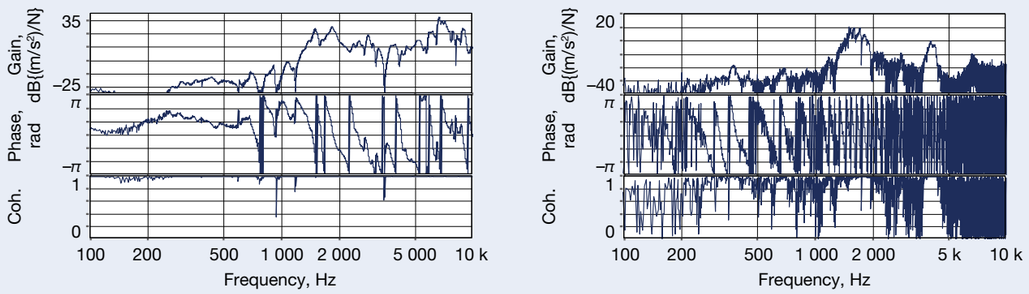

(a) Response at the accelerometer No. 6 in the X direction

(b) Response at the accelerometer No. 10 in the X direction

Fig. 10 Measured inertances and their coherences whose impact position is near the accelerometer No. 6 in the X direction

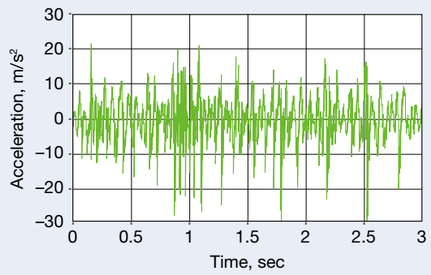

Fig. 11 Measured acceleration using the accelerometer No. 6 in the X direction by vehicle running test on the cobble road at 15 km/h

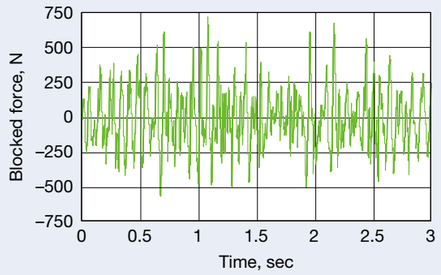

Fig. 12 Blocked force at the connection of EPS near the accelerometer No. 6 in X the direction identified by means of inverse matrix method using the measured inertances and accelerations

mounting position, we aligned the direction of the three axes of the sensor with XYZ by inserting an aluminum piece. Figures 10 and 11 show the inertance and vibrations we measured as described above, while Figure 12 shows one of the blocked forces we calculated by substituting these inertance and vibrations into Equation (1). In addition to the excitation point inertance at the same position and in the same direction as the excitation force (Figure 10 (a)), Figure 10 also shows the inertance at a position far from the excitation point (Figure 10 (b)). From each coherence, the inertance was measured accurately near the excitation point but not at the position far from the excitation point, particularly at high frequencies.

The vibro-acoustic transfer function of the vehicle (i.e., the transfer function between the blocked force and the target sound pressure) was obtained by impulse excitation of each EPS connection, as was the same with the above-mentioned inertance. As a result, at the same time as the vibration of the reference point, we measured the sound pressure using a microphone installed near the center of the steering wheel, with which we obtained a total of 18 vibro-acoustic transfer functions. Figure 13 shows the case of exciting the connection (No. 6) on the upper right of the column in the X direction, which indicates a high coherence. Figure 14 shows frequency spectra of the impulse excitation forces and coherences of the vibro-acoustic transfer functions in all the cases, including the X direction excitation of No. 6. The coherence in the X direction of No. 6 is high, although excitation is not performed at the middle frequency band due to the influence of a natural frequency. On the contrary, some coherences are low even when excitation is performed up to the high-frequency band.

Next, we estimated the rattle noise using the blocked force and vibro-acoustic transfer function as the TPA input. The blocked force is a time waveform, but the vibro-acoustic transfer function is a frequency spectrum, so we calculated the sound pressure in the time domain by convolution of these and extracted the rattle noise component by applying the filters described in the

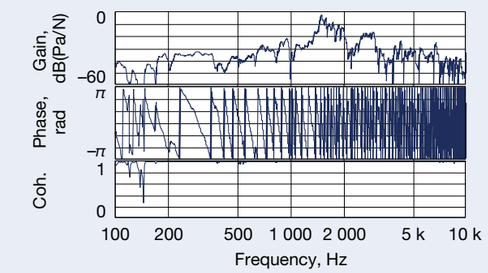

Fig. 13 Measured vibro-acoustic transfer function and its coherence whose impact position is near the accelerometer No. 6 in the X direction and sound pressure is measured by the microphone No. 7

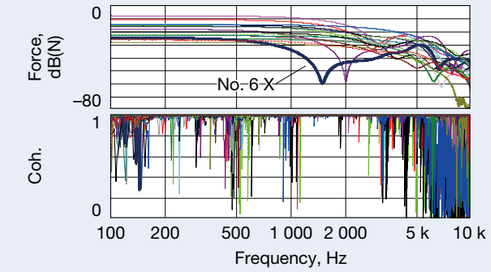

Fig. 14 Upper figure indicates frequency spectra of all impact forces applied to measure the vibro-acoustic transfer unctions, and the lower figure indicates their coherences

previous chapter. As shown in Figures 10 and 14, the inertance and the coherence of the vibro-acoustic transfer function are low in the high-frequency band, meaning that the estimated accuracy of the high-frequency band would be low. Furthermore, we considered the steering wheel as part of the EPS, so it is not necessary to consider the blocked force at the connection between the steering wheel and the column shaft. The target sound pressure did not mainly result from structure-borne noise but from airborne noise directly radiated from the EPS.

3.2 Verification procedures and results

Figure 15 shows the verification process flow. First, in a stationary vehicle, we measured the vibro-acoustic transfer function from each EPS connection to the target (Step 1), and simultaneously we measured the inertance from each EPS connection to each reference point (Step 2). Next, we measured the vibration at each reference point in a vehicle running test (Step 3) and simultaneously the target sound pressure (Step 4). Then, we calculated the blocked force from the measured inertance and vibration

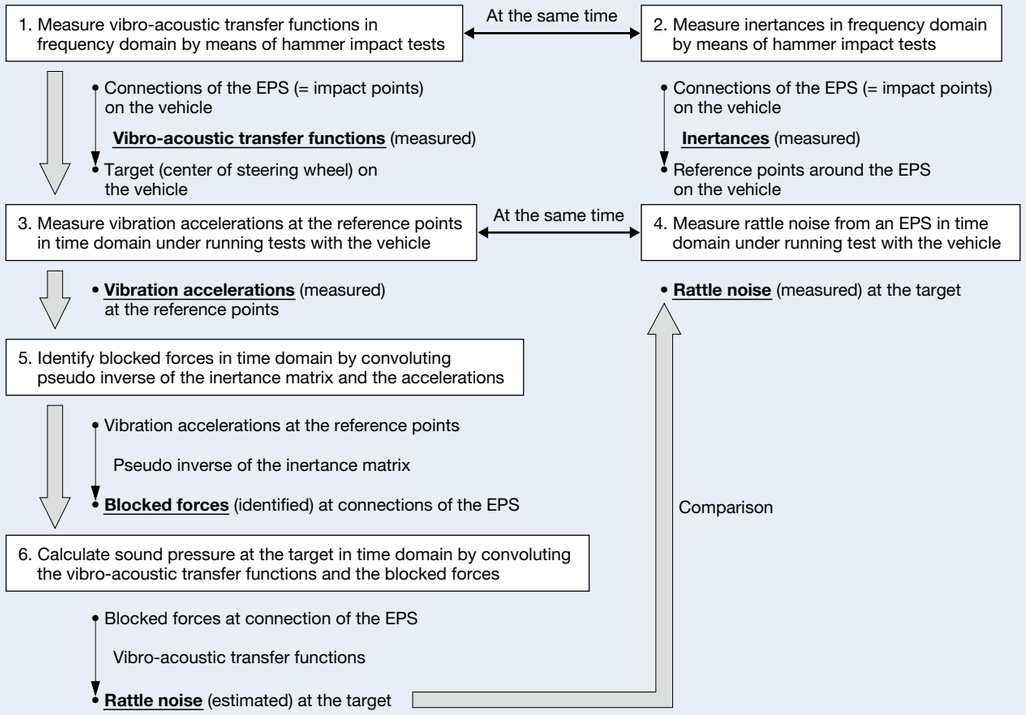

Fig. 15 Experimental verification procedure of the estimation method by application to rattle noise from an EPS. Blocked forces of the EPS are identified by vehicle running test.

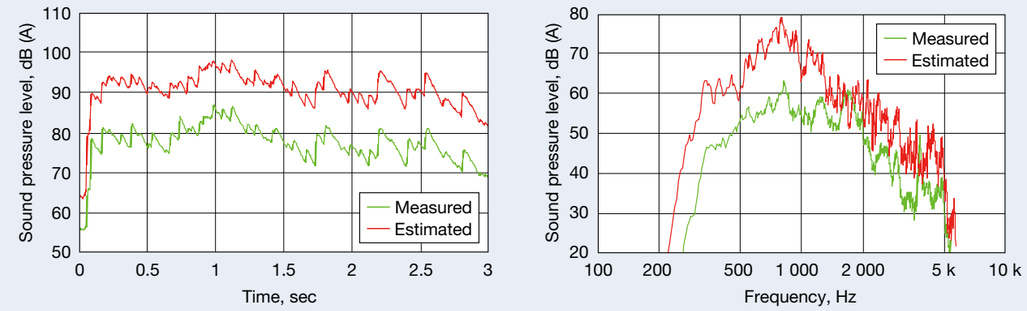

(a) Time waveforms of sound pressure levels (TC = 50 ms)

(b) Frequency spectra of sound pressure levels

Fig. 16 Measured and estimated sound pressure levels corresponding to EPS rattle noise extracted by both A-weighting filter and a band-pass filter from 300 Hz to 5 kHz by vehicle running test on the cobble road at 15 km/h

(Step 5) and the target sound pressure by multiplying the blocked force by the vibro-acoustic transfer function (Step 6). Finally, we applied the abovementioned filters to both the measured and calculated sound pressures to extract and compare the rattle noise component. Figure 16 shows the results of comparing the sound pressure levels and the frequency spectra between the measured and estimated rattle noise. The sound pressure level differs by about 12 dB, and the frequency spectrum also differs from each other.

3.3 Estimation error reduction method

As mentioned in this report's introduction, since the estimation method proposed in this study is an approximation, the sound pressure level difference between the estimated and measured rattle noise shown in Figure 16 includes the influence of such approximation. As mentioned in the previous report[12], peaks of the blocked force at natural frequencies of the active subsystem result in overestimation of the sound pressure level, but this estimation error could be reduced by using the proposed method. In our proposed estimation error reduction method, the singular value decomposition of Equation (2) is employed to calculate the pseudo inverse of the inertance matrix, and some small singular values are discarded in this calculation. Generally, this method is employed to reduce the numerical calculation errors when the condition number (i.e., the ratio of the maximum singular value with respect to the minimum singular

$$[G]^{+}_{\text{regularized}} = [V] \begin{bmatrix} 1/\sigma_1 & 0 & \cdots & 0 & \cdots & 0 & 0 \\ 0 & \ddots & & \vdots & & \vdots & \vdots \\ \vdots & & 1/\sigma_M & \vdots & & & \\ & & & 0 & & & \\ \vdots & & & \vdots & \ddots & \vdots & \vdots \\ 0 & \cdots & \cdots & 0 & \cdots & 0 & \cdots & 0 \end{bmatrix} [U]^{*}, \quad 1-\frac{\sum_{r=1}^{M}\sigma_r^2}{\sum_{r=1}^{N}\sigma_r^2} \le \phi < 1-\frac{\sum_{r=1}^{M-1}\sigma_r^2}{\sum_{r=1}^{N}\sigma_r^2} \qquad \cdots\cdots\cdots (3)$$

value) is excessive[8] but, as previously reported, it is also effective in reducing the estimation error of the proposed method. The number of singular values to be discarded should be such that the approximate indication[5] based on the ratio of the sum of squared singular values is constant at each frequency. Specifically, as shown in Equation (3), in the case of an inertance matrix with N singular values, a pseudo-inverse matrix is composed of M (< N) singular values using a common threshold ϕ for each frequency.

Figure 17 shows time waveform of the blocked force identified using the pseudo-inverse matrix when the threshold ϕ in Equation (3) was 0.03, while Figure 18 shows the sound pressure levels and frequency spectra of

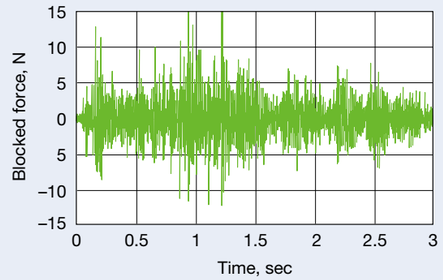

Fig. 17 Blocked force at the connection of EPS near the accelerometer No. 6 in the X direction identified by means of inverse matrix method with the regularization factor ϕ = 0.03

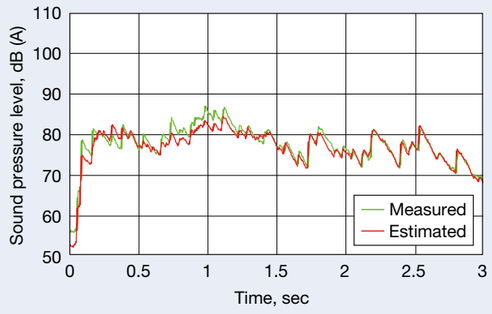

(a) Time waveforms of sound pressure levels (TC = 50 ms)

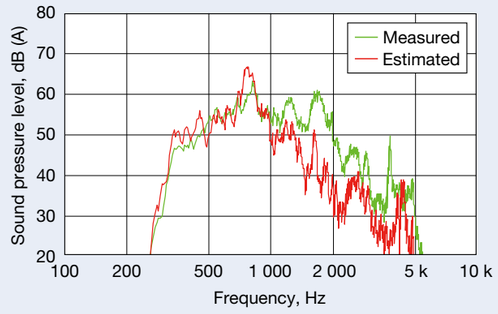

(b) Frequency spectra of sound pressure levels

Fig. 18 Measured and estimated sound pressure levels corresponding to EPS rattle noises extracted by both A-weighting filter and a band-pass filter from 300 Hz to 5 kHz by vehicle running test on the cobble road at 15 km/h. The inertances used to estimate sound pressure are regularized with the factor ϕ = 0.03.

the rattle noise. We adjusted the threshold value of 0.03 so that the averaged sound pressure level of the estimated rattle noise matched that of the measured noise, but also the time waveform of the estimated noise became almost the same as that of the measured noise. Therefore, although there are some differences in the spectral shape at high frequencies, we could estimate a generally reasonable sound pressure level by using the estimation error reduction method proposed in our previous report.

Figure 19 (a) shows condition numbers of the inertance matrix before and after discarding small singular values, while Figure 19 (b) shows the numbers of singular values that compose the pseudo-inverse matrix at that time. In each figure, in addition to the case of ϕ = 0.03, the case of ϕ = 0.001 is shown for reference. In the case of ϕ = 0.03, the condition number is smaller than in the case of ϕ = 0.001, meaning that more small singular values are discarded. When the absolute value of the condition number in each case is compared to the previous report, the condition number in the case of ϕ = 0.001 is already sufficiently small, and then the numerical calculation errors and the estimation errors due to our proposed method should be small. Therefore, the small singular values discarded by increasing the threshold from ϕ = 0.001 to ϕ = 0.03 is not necessary for reducing the errors but for eliminating other factors. In terms of prerequisites for applying the proposed estimation method, the entire mechanical system is divided into an active subsystem including vibration sources and a passive subsystem on the side to which the force of the vibration source transfers, and the blocked force particular to the active subsystem is identified indirectly to estimate airborne noise and structure-borne noise. In this study, the EPS is an active subsystem, and the vehicle body structure (other than the EPS) is a passive subsystem. However, since the vehicle body structure includes other vibration sources such as an engine, this does not entirely meet the prerequisites for applying the proposed estimation method. Therefore, the vibration accelerations measured at the reference points shown in Figure 7 include influence of the other vibration sources such as an engine, and the blocked force calculated using the inverse matrix method using this vibration acceleration as an input and the estimated target sound pressure also include such influence, and then the threshold needs to be increased in order to eliminate the influence. The target sound pressure measured with a microphone installed near the center of the steering wheel also includes the influence of other vibration sources such as an engine, but these influences could be eliminated using the band-pass filter described above. However, the band-pass filter might not be able to eliminate the influence because the vibration accelerations measured at the reference points shown in Figure 7 are sensitive to other vibration sources such as an engine. In Figure 16

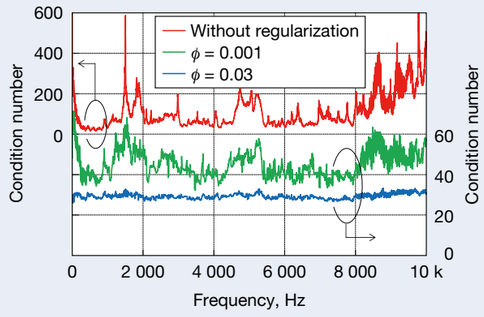

(a) Condition numbers

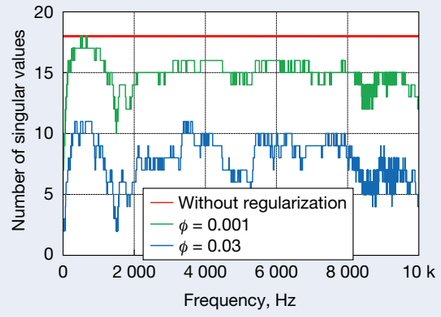

(b) Number of singular values

Fig. 19 Condition numbers and number of singular values of the inertance matrices with and without regularization for identifying blocked forces by means of inverse matrix method

(a), the difference in sound pressure level is about 12 dB between the estimated and measured rattle noise, but when $\phi = 0.001$, the difference is still about 10 dB. From these results, it seems that the influence of other vibration sources, such as an engine, is the main factor in the difference in Figure 16 (a) and is almost constant through the frequency band of the rattle noise.

In addition, while the time waveforms of the sound pressure level match relatively well in Figure 18 (a), there are some differences (especially in the high-frequency band) in Figure 18 (b). Since the frequency spectra in Figure 18 (b) are averaged frequency spectra of 3 seconds, the vibration acceleration data was divided every 0.5 second, and frequency spectra were calculated at each section, as shown in Figure 20. When comparing Figure 20 (a) with Figure 20 (b) in the first half of the data, there are some differences between the shapes of the frequency spectra, but the differences in Figure 20 (c) and Figure 20 (d) in the second half of the data are relatively small.

In Figure 18 (a), there are also some differences between the time waveforms in the first half (unlike in the second half), so it seems that the difference between the averaged frequency spectra results from the differences between the frequency spectra in the first half of the data. Regarding the reason for the difference between the frequency spectra in the high-frequency band, one factor is low coherences of the inertance and vibro-acoustic transfer function, as shown in Figures 13 and 14.

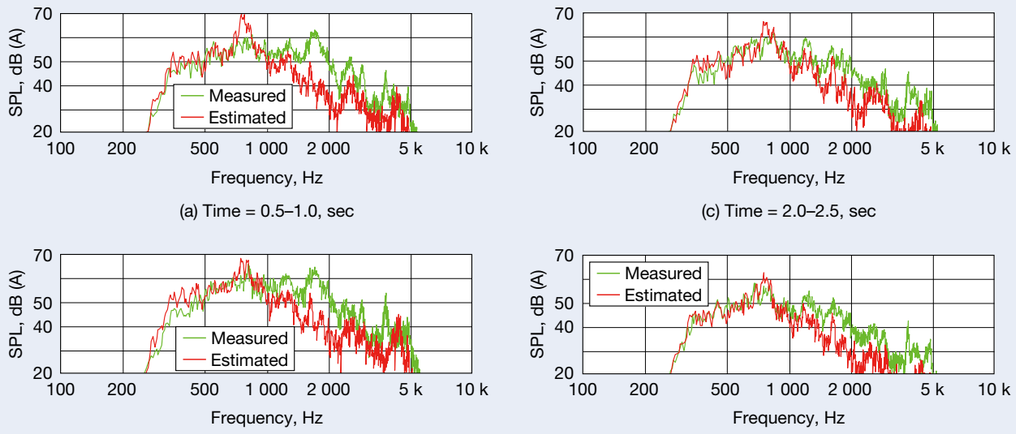

(a) Time = 0.5–1.0, sec

(c) Time = 2.0–2.5, sec

(b) Time = 1.0–1.5, sec

(d) Time = 2.5–3.0, sec

Fig. 20 Frequency spectra of the measured and estimated sound pressure levels which are part of the data in Fig. 18

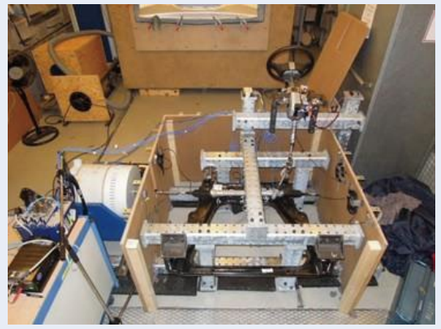

(a) Overall view

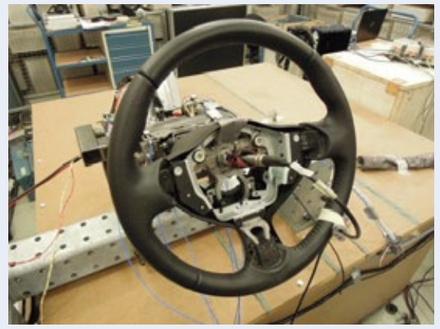

(b) Microphone at the steering wheel center (No. 7)

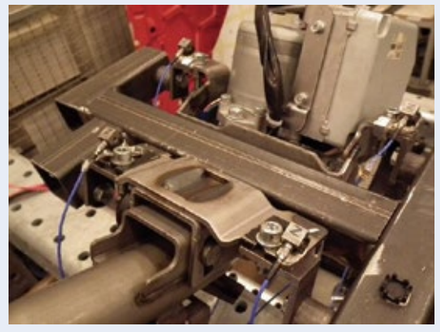

(c) 3-axis accelerometers on the connections of steering column (No. 3, 4, 5, 6)

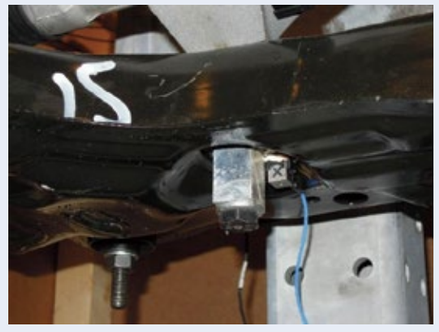

(d) 3-axis accelerometer on the right hand connection of steering gear housing (No. 2)

(e) Additional 3-axis accelerometer on the front-right connection of sub-frame (No. 12)

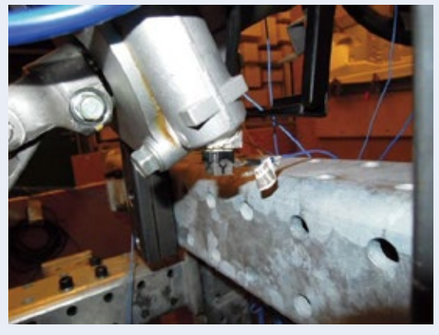

(f) Additional 3-axis accelerometer on the worm/wheel gear housing of steering column (No. 9)

Fig. 21 EPS component test bench for evaluating rattle noise

4. Verification When Identifying the Blocked Force by the EPS Component Test

4.1 EPS component test bench configuration

igure 21 (a) shows the appearance of the EPS component test bench. The subframe of the vehicle was diverted for fixing the steering gear housing to the mainframe of the component test bench in order to improve blocked force identification accuracy by making the structure of the component test bench similar to that of the vehicle[7]. Also, the column was fixed to the mainframe via another fixture. External force was applied to one tie rod of the EPS in the axial direction, as described in Section 2.2, and the positions of the reference points for vibration measurement were the same as those for the vehicle, as shown in Figure 21 (c), (d), (e), and (f). However, as shown in Figure 21 (c), the sensor installation at the column connection differed between the lower surface side (vehicle) and upper surface side (component test bench) verticals. Inertances were measured by impulse excitation, which was the same as in the case of the vehicle. As shown in Figure 20 (b), sound pressure was measured by a microphone installed near the center of the steering wheel to compare with the case of the vehicle for reference, and the results are shown in Figure 1. Since the noise radiated from the vibration exciter and the subframe was so loud, the entire component test bench was covered with wooden boards except for the steering wheel portion.

Regarding the axial vibration of the tie rod, we tried to reproduce mean amplitude of the vibration acceleration in the frequency domain when the vehicle was running. Since the vibration exciter has an upper limit of stroke, the lower frequency limit of the control signal was set to 10 Hz. The upper frequency limit was set to 100 Hz so as not to overlap with the frequency band of the rattle noise component of 300 to 5 000 Hz, as described above.

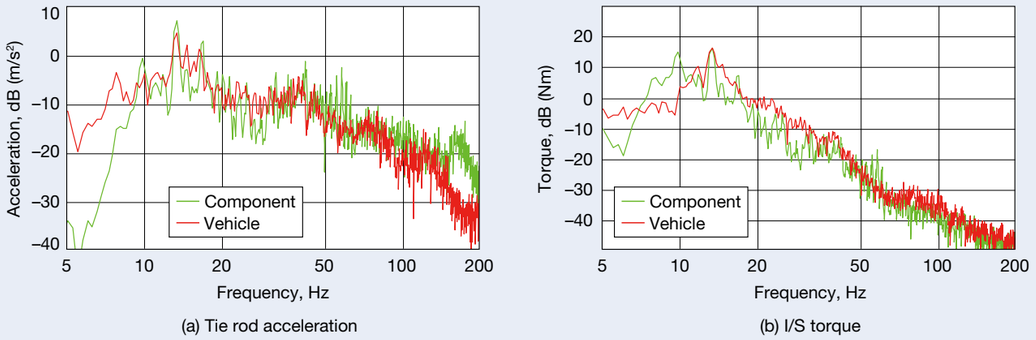

Fig. 22 Frequency spectra of tie rod axial accelerations and I/S torques by component test and by vehicle running test

Figure 22 (a) shows a comparison of the reproduced vibration acceleration in the tie rod axial direction with the component test bench and the measured noise when the vehicle was running. The results indicate that, in addition to the dominant peak level near 15 Hz, the approximate spectral shape could be reproduced by using the component test bench. Although the control signal of 10 to 100 Hz was applied to the vibration exciter, the resulted vibration acceleration includes a frequency component of less than 10 Hz and more than 100 Hz. Figure 22 (b) shows a comparison of the intermediate shaft torques measured with the component test bench and the vehicle. Although there is an unnecessary peak near 10 Hz in the case of the component test bench, the spectral shapes in other parts are almost the same.

4.2 Verification procedures, results, and discussion

Figure 23 shows the verification procedures. First, in the stationary vehicle, the vibro-acoustic transfer function from each connection of the EPS to the target microphone was measured (Step 1). Next, the vibration acceleration of the tie rod in the running test of the vehicle was measured

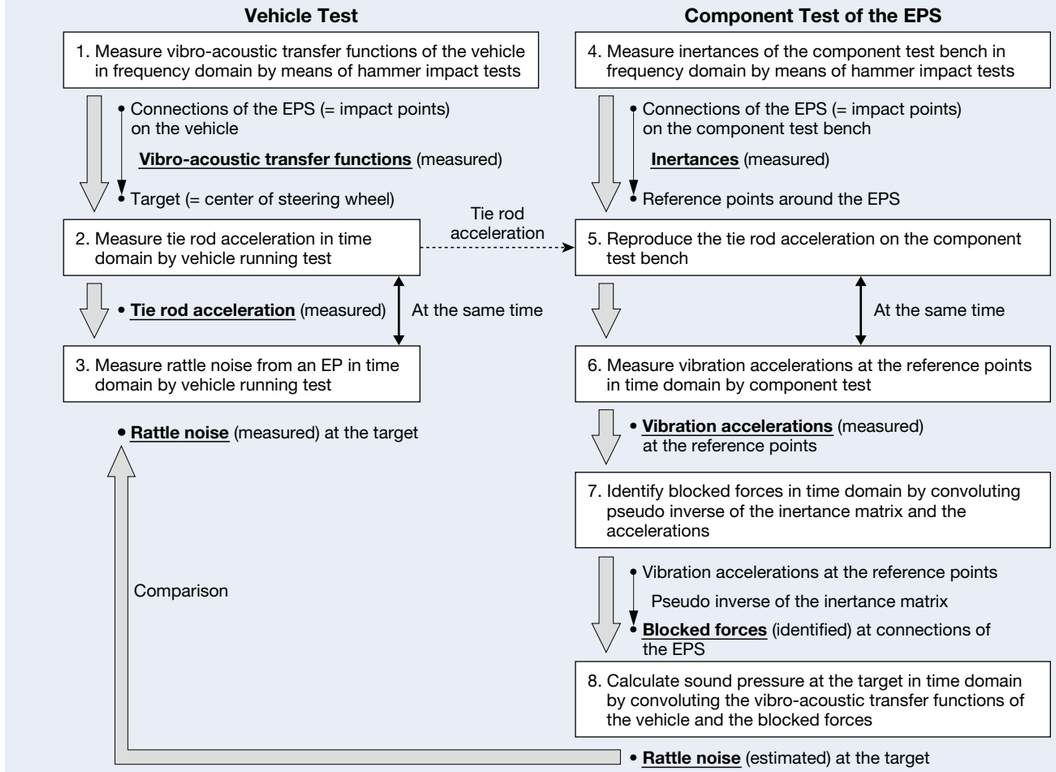

Fig. 23 Experimental verification procedure of the estimation method by application to rattle noise from an EPS. Blocked forces of the EPS are identified by component test.

(Step 2), and simultaneously the target sound pressure was measured (Step 3). Then, in the EPS component test bench, the inertance from each connection of the EPS to each reference point was measured (Step 4). Next, the vibration acceleration of the tie rod measured by the vehicle running test was reproduced by using the test bench (Step 5), and vibration accelerations of the reference points were measured (Step 6). Then, the blocked forces were calculated from the measured inertances and vibration accelerations (Step 7), and the target sound pressure was calculated by multiplying the blocked forces by the vibro-acoustic transfer functions (Step 8). Finally, the above-mentioned filters were applied to both the measured and calculated sound pressures to extract the rattle noise components

Figure 24 shows comparisons of the sound pressure levels and the frequency spectra between the measured and estimated rattle noise. As mentioned before, we reproduced mean amplitude of the axial vibration acceleration of a tie rod during vehicle running in the frequency domain using the test bench, but the waveform of the sound pressure level differed in the time domain shown in Figure 24 (a) because the phase was not taken into account. However, not only are the waveforms different, but the averaged sound pressure levels shown in the legend of Figure 24 (a) differ by about 5 dB, and the spectra shown in Figure 24 (b) also have differences such as peaks from 300 to 700 Hz. As already mentioned, these differences could be caused by numerical calculation errors and estimation errors due to our proposed method. In order to reduce these errors, the threshold value ϕ in Equation (3) was set at 0.001 by referring to the examination in Chapter 3. As a result, as shown in the legend of Figure 25 (a), the averaged sound pressure level of the estimated rattle noise was 78.2 dB (A), i.e., almost the same as the 78.4 dB (A) measured by the vehicle running test. Although there is still a difference in shape of the frequency spectrum, as shown in Figure 25 (b), this could be because the reproduction accuracy of the tie rod axial vibration acceleration in the test bench was insufficient and because the inertances and vibro-acoustic transfer functions were not obtained with a vibration exciter ideally but with impulse excitation. Figure 26 (a) shows the condition numbers of the inertance matrix before and after discarding small singular values, and Figure 26 (b) shows the number of singular values that compose those matrices. Compared to the case where the threshold ϕ is 0.03 in Figure 19, the number of discarded singular values is lower, so only the errors seems to be reduced by improving the condition number, which indicates that adjustment or elimination of other factors is not necessary. In the case of the vehicle running test shown in Figures 16 and 18, the rattle noise and vibration accelerations, which are required for estimating the rattle noise, were measured at the same time, so it was possible to compare whether the time waveforms matched but, as described above, the time waveforms estimated by the component test bench were not comparable. With that in mind, in Figures 24 (a) and 25 (a), the maximum and minimum values in the time waveforms of longer than

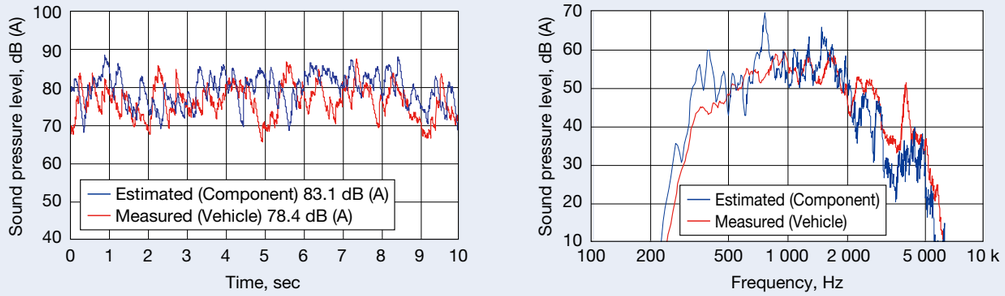

(a) Time waveforms of sound pressure levels (TC = 50 ms)

(b) Frequency spectra of sound pressure levels

Fig. 24 Sound pressure levels corresponding to EPS rattle noises extracted by both A-weighting filter and a band-pass filter from 300 Hz to 5 kHz. One is measured by vehicle running test and the other is estimated by component test.

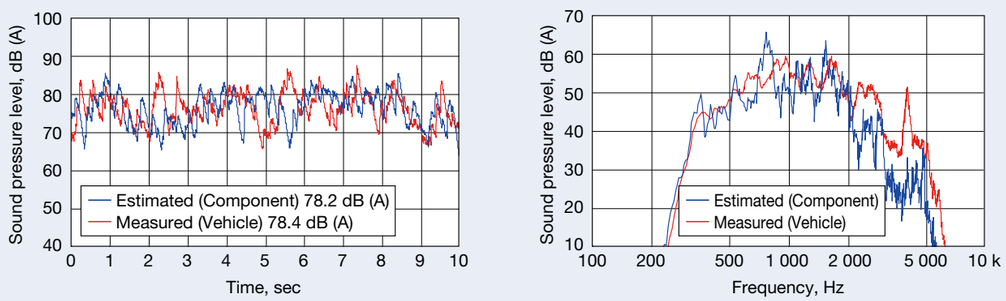

(a) Time waveforms of sound pressure levels (TC = 50 ms)

(b) Frequency spectra of sound pressure levels

Fig. 25 Sound pressure levels corresponding to EPS rattle noises extracted by both A-weighting filter and a band-pass filter from 300 Hz to 5 kHz. One is measured by vehicle running test and the other is estimated by component test. The inertances used to estimate sound pressure are regularized with the factor $\phi = 0.001$.

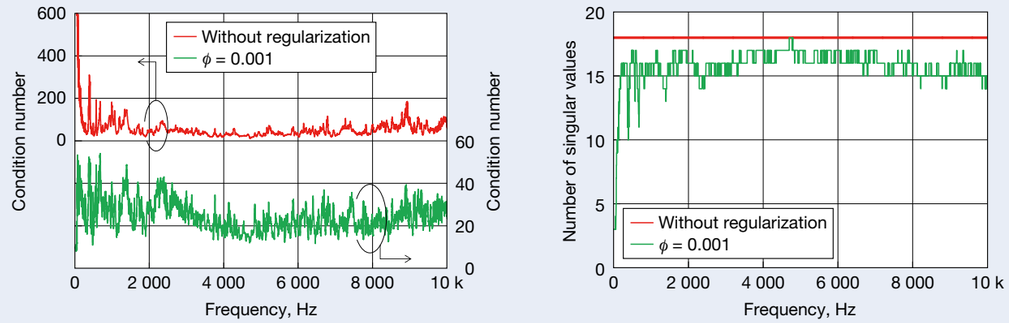

(a) Condition numbers

(b) Number of singular values

Fig. 26 Condition numbers and number of singular values of the inertance matrices with and without regularization for identifying blocked forces by means of inverse matrix method.

10 seconds were compared, and, as Figure 25 (a) shows, these values are almost the same. Considering the above, quantitatively estimation of the rattle noise during vehicle running could be possible by the EPS component tests with the estimation error reduction method proposed in the previous report[12], and it would appear that the proposed estimation method was experimentally verified.

The axial vibration acceleration, which was reproduced by the EPS component test, and the vibration acceleration at each reference point, which was required for identification of the blocked force, were not measured with the same vehicle running test due to the upper limit of the recorder channels. Therefore, the measured rattle noise shown in Figures 16 and 18 is different from that shown in Figures 24 and 25. However, the averaged sound pressure levels and spectral shapes of the rattle noise measured in both tests are almost the same as that shown in Figure 27, so it is reasonable to assume that the axial vibration acceleration of the tie rod is also the same. As mentioned in the introduction, blocked force is a value particular to the active subsystem, and if the axial vibration acceleration of the tie rod is the same, then the blocked force identified by the EPS component test should be the same as the blocked force identified by the vehicle running test. Based on this, the two blocked forces will be compared. Incidentally, the time waveforms of the sound pressure level in Figure 27 that showed 10 seconds, and the time waveform of the measured sound pressure level in Figures 16 and 18 corresponds to that from three to six seconds in Figure 27.

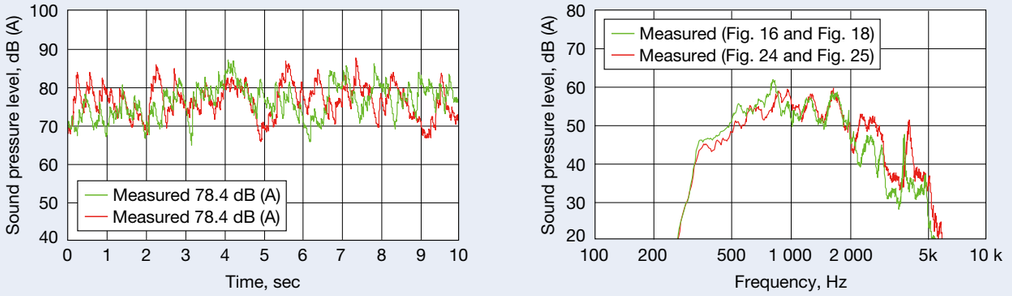

(a) Time waveforms of sound pressure levels (TC = 50 ms)　(b) Frequency spectra of sound pressure levels

Fig. 27 Measured sound pressure levels corresponding to EPS rattle noises extracted by both A-weighting filter and a band-pass filter from 300 Hz to 5 kHz. One is same with the data shown in Figure 16 and 18 although analyzed time is longer than them. The other is same with the data shown in Figure 24 and 25.

(a) Time waveforms of the blocked forces　(b) Frequency spectra of the blocked forces

Fig. 28 Blocked forces at the connection of EPS near the accelerometer No. 6 in the X direction. One is identified by inverse matrix method with the regularization factor $\phi = 0.03$ and vibrations measured by vehicle running test (same with Fig. 17). The other is similarly identified with the factor $\phi = 0.001$ and vibrations measured by component test.

Figure 28 shows a comparison of each time waveform and frequency spectrum between the blocked forces. In the case of the blocked force identified by the component test, the estimation errors were reduced by setting the threshold to $\phi = 0.001$ in Equation (3), and in the case of the blocked force identified by vehicle running test, the influence of other vibration sources was eliminated by setting the threshold to $\phi = 0.03$. For both tests, the maximum values were equivalent at about 15 N, and the spectral shapes were almost the same. Therefore, it is considered that the same blocked force was identified in both tests.

In addition, the averaged sound pressure level measured by the component test was 71.1 dB (A), as shown in Figure 1. Compared to the sound pressure level of 78.4 dB (A) measured by the vehicle running test, the difference is 7.3 dB. On the other hand, the sound pressure level estimated by the component test with the proposed method is 78.2 dB (A), so the difference from the sound pressure level measured by the vehicle running test is 0.2 dB. Therefore, the sound pressure level estimated with the proposed method has better estimation accuracy compared to the noise measured by the component test.

4.3 Verification by evaluation of EPS individual differences

Next, we will describe the results of verifying the proposed estimation method by evaluating the individual differences in EPS. As Figure 23 shows, the vehicle running conditions of the estimated and measured rattle noise in Figure 25 were identical. However, when evaluating individual differences, it is possible to test under the same vibration conditions in the component test bench, but impossible in the vehicle running test since the vehicle running conditions varied each time because of irregular cobblestones. Therefore, in the vehicle running test, multiple running tests were performed, and the averaged sound pressure level of the rattle noise was evaluated for each.

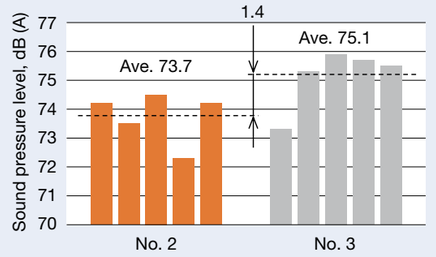

Fig. 29 Sound pressure levels measured by vehicle running tests with the EPS No. 2 and No. 3. Five measurements were done with each EPS.

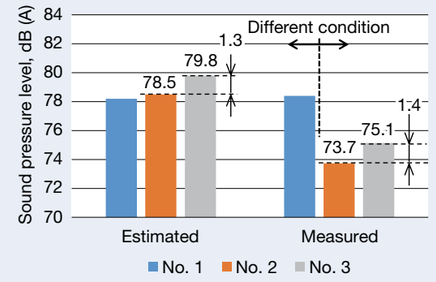

Fig. 30 Left-hand sound pressure levels were estimated by component tests on which tie rod acceleration measured by vehicle running test with the EPS No. 1 was reproduced. Right-hand sound pressure levels were measured by vehicle running tests. The test condition used to measure sound pressure level with EPS No. 2 is same as that with EPS No. 3 but is different from that of EPS No. 1.

Using two non-standard EPSs in which joint gaps of the intermediate shaft were intentionally changed, measurements of the rattle noise were conducted five times by the vehicle running test of 10 seconds on the same test course with each EPS. Figure 29 shows the averaged sound pressure level of each measurement, where No. 1 indicates the EPS used in Figures 24 and 25, and Nos. 2 and 3 indicate two non-standard EPSs. As shown, the sound pressure level varied from measurement to measurement, and the average of the five measurements differed significantly, by 1.4 dB. Furthermore, by using the proposed method, we could quantitively estimate the sound pressure level during vehicle running. Figure 30 shows a comparison of the averaged sound pressure levels of the rattle noise estimated by the component test and those measured by the vehicle running test, including No. 1. The first thing to notice is that the sound pressure levels of the rattle noise estimated in Nos. 2 and 3 differs significantly from the measurements. One reason for this is that the vehicle running conditions of the measurements with Nos. 2 and 3 were not the same as that with No. 1, although the same tie rod axial vibration acceleration with No. 1 was reproduced in the component test with Nos. 2 and 3 for estimating the rattle noise. However, the difference is larger than the variation for each run, as shown in Figure 29. The other reason is that the measurements with Nos. 2 and 3 were conducted on the same test course on the same day, whereas the measurement with No. 1 was conducted on a different day at a different temperature and humidity level. Furthermore, the Ford Lommel Proving Ground has several test courses with similar cobble roads, and the test course used by the measurement with No. 1 was different from that with Nos. 2 and 3. These factors could contribute to the fact that the sound pressure levels of the rattle noise estimated with Nos. 2 and 3 were significantly different from those measured, but the details are unknown. So, the proposed estimation method has not yet been verified quantitatively.

Regarding the individual differences between Nos. 2 and 3, the sound pressure level of the rattle noise estimated with No. 3 is 1.3 dB higher than that with No. 2 in the component tests, whereas the sound pressure level of the rattle noise measured with No. 3 is 1.4 dB higher than that with No. 2 in the vehicle running tests. This means that the individual difference of the sound pressure levels estimated by the component test corresponds to the noise measured by the vehicle running test, thus the effectiveness of the proposed estimation method was verified qualitatively.

5 Conclusion

In this report, in order to estimate sound pressure level including airborne noise, we employed the in-situ blocked force approach proposed in our previous report and reduced the estimation errors by discarding small singular values in the inverse matrix method used in the process, and we demonstrated an estimation of the rattle noise from an electric power steering system (EPS) for automobiles, which is dominated by the natural frequency component, and the following conclusions were obtained.

(1) By applying the in-situ blocked force approach to both the vehicle running test and EPS component test in which the EPS (including the steering wheel) as an active subsystem, the identified blocked forces, from which the influence of vibration sources other than the EPS, were proved to be comparable to each other.

(2) The sound pressure level of the rattle noise was estimated by applying the proposed method to a vehicle running test. As a result, by discarding small singular values in order to eliminate the influence of vibration sources other than the EPS, the estimated sound pressure level and time waveform corresponded to the measured noise, which indicates that sound pressure level including airborne noise, which is dominated by the natural frequency component, could be estimated with high accuracy by the proposed method.

(3) The sound pressure level of the rattle noise was estimated by applying the proposed method to the EPS component test. As a result, the estimated sound pressure level corresponded to the measured noise by the vehicle running test, which indicates that the sound pressure level including airborne noise, which is dominated by the natural frequency component, could be estimated with high accuracy by the proposed method.

(4) The individual difference of the sound pressure levels estimated by the component test with two EPSs qualitatively corresponded to the measurement averaged by the five vehicle running tests, which indicates that the influence of the individual EPS difference on the rattle noise could be evaluated by the proposed method.

Acknowledgments

This report is the result of joint research between Forschungsgesellschaft Kraftfahrwesen mbH Aachen and NSK Ltd. We would like to express our gratitude to both companies.

Appendix

Investigation of the external force in the EPS component test bench by vehicle vibration tests

Although the vibration source of the EPS rattle noise is the collision between parts, to reproduce this collision in the EPS component test bench, the low-frequency resonance of the chassis system needs to be reproduced. The low-frequency resonance could be caused by movement of the tires in the vertical and steering-angle direction, but in order to investigate which direction has the greater influence on the rattle noise, we conducted vehicle vibration tests in each direction independently. The vertical vibration test shown in Figure A1 (a) reproduced the vertical vibration accelerations of the knuckles at the left and right sides simultaneously during vehicle operation, while the vibration test in the steering-angle direction shown in Figure A2 (a) reproduced the horizontal vibration acceleration of the knuckle on the opposite side of the wheel to which external force was applied with a vibration exciter. The high-frequency hitting sound (a characteristic of the rattle noise) does not appear in the STFT analysis result of the vertical vibration shown in Figure A1 (b), but it appears in that of the steering-angle direction shown in Figure A2 (b). In addition, the rattle noise was audible only in the steering-angle direction, so it seems that tire movement in the steering-angle direction

(a) Vibration test

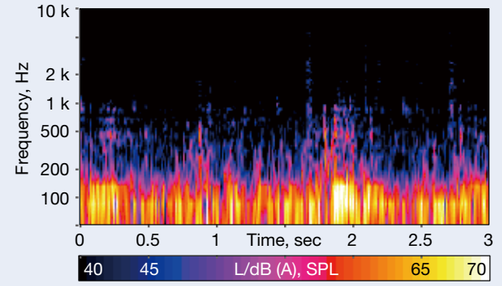

(b) Time-frequency spectrum of the sound pressure

Fig. A1 Vibration test of a vehicle under the condition that front wheels are excited in the vertical direction

(a) Vibration test

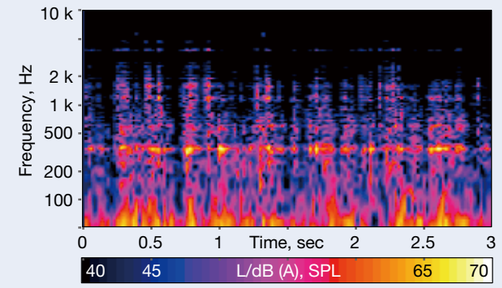

(b) Time-frequency spectrum of the sound pressure

Fig. A2 Vibration test of a vehicle under the condition that front wheels are excited in the steering direction

is the dominant factor in the rattle noise, and we therefore applied the external force only in the axial direction of the tie rod in the EPS component test bench.

References

1) Auweraer, H.V., Mas, P., Dom, S., Vecchio, A., Janssens, K., and Ponseele, P.V., "Transfer path analysis in the critical path of vehicle refinement: the role of fast, hybrid and operational path analysis," SAE Technical paper, 2007-01-2352 (2007).
2) Elliott, A.S. and Moorhouse, A.T., "Characterisation of structure borne sound sources from measurement in-situ," Proceedings of Acoustics 2008 Paris (2008), pp. 1,477–1,482.
3) Elliott, A.S., Moorehouse, A.T., Huntley, T., and Tate, S., "In-situ source path contribution analysis of structure borne road noise," *Journal of Sound and Vibration*, Vol. 332 (2013), pp. 6,276–6,295.
4) Gardonio, P. and Brennan, M.J., "Moblility and impedance methods in structural dynamics," *Advanced application in acoustics, noise and vibration* (2004), pp. 389–447.
5) Greenacre, M.J., "Singular value decomposition (SVD) and multidimensional analysis," Theory and applications of correspondence analysis, *Academic Press* (1984), p. 344.
6) Klerk, D. and Rixen, D.J., "Component transfer path analysis method with compensation for test bench dynamics," *Mechanical Systems and Signal Processing*, Vol. 24 (2010), pp. 1,693–1,710.
7) Lennström, D., Olsson, M., Wullens, F., and Nykänen, A., "Validation of the blocked force method for various boundary conditions for automotive source characterization," *Applied Acoustics*, Vol. 102 (2016), pp. 108–119.
8) Martens, T. and Wyckaert, K., "Matrix inversion technology for vibro-acoustic modeling applications: practical examples of measurement noise reduction by SVD," Proceedings of ISMA 23 (1998).
9) Mas, P., Sas, P., and Wyckaert, K., "Indirect force identification based upon impedance matrix inversion: A study on statistical and deterministical accuracy," Proceedings of ISMA19 (1994), pp. 1,049–1,065.
10) Moorhouse, A.T., Elliott, A.S., and Evans, T.A., "In situ measurement of the blocked force of structure-borne sound sources," *Journal of Sound and Vibration*, Vol. 325 (2009), pp. 679–685.
11) Sato, Y. and Iwatsuki, N., Estimation of noise radiation including airborne noise using the in-situ blocked force approach (Proposal of an approximate method and its verification using a simple model), Transactions of the JSME (in Japanese), Vol. 84, No. 865 (2018), DOI:10.1299/transjsme.18-00049.
12) Sato, Y., Murakami, K., and Iwatsuki, N., Estimation of noise radiation including airborne noise using the in-situ blocked force approach (Second report, verification of the estimation method by numerical analysis of noise radiation from a cantilever rectangular plate and proposal of an estimation error reduction method), Transactions of the JSME (in Japanese), Vol. 86, No. 882 (2020), DOI:10.1299/transjsme.19-00348.
13) Shiozaki, H., Geluk, T., Daenen, F., Iwanaga, Y., and Herbruggen, J.V., "Time-domain transfer path analysis for transient phenomena applied to tip-in/tip-out (shock & jerk)," SAE Technical paper, 2012-01-1545 (2012).

Yoshihiro Sato

Jan Hendrik Elm

Jens Viehöfer

Jan-Welm Biermann

Nobuyuki Iwatsuki

Fracture Mechanics-Based Criteria for Fatigue Fracture of Rolling Bearings under the Influence of Defects

Daisuke Watanuki, Masako Tsutsumi
Core Technology R&D Center, Technology Research & Development Office 1
Hideyuki Hidaka
Core Technology R&D Center
Kentaro Wada
Department of Mechanical Engineering, Fukuoka University
Hisao Matsunaga
Department of Mechanical Engineering, Kyushu University
International Institute for Carbon-Neutral Energy Research (I2CNER), Kyushu University
AIST-Kyushu University Hydrogen Materials Laboratory (HydroMate)

This article is reprinted with permission from John Wiley & Sons, Inc. from *Fatigue & Fracture of Engineering Materials & Structures*, Vol. 44, Issue 4 (2021).

Abstract

Fatigue tests were carried out on real bearings with various types of artificial defects on their outer-ring raceways. Finite element analysis (FEM) revealed that the stress intensity factor (SIF) ranges and stress ratios were complex and variable, depending on the gap fittings between the outer rings and housings, as well as on the sizes of the initial defects, both of which influenced the fatigue thresholds of the bearings. In order to establish a comprehensive evaluation of fatigue limits under several combinations of bearing geometries and defect sizes, fatigue crack-growth thresholds were also measured at different stress ratios by focusing on crack-closure behaviour. Based on all of the analytical and experimental results, fracture mechanics-based criteria were proposed for the assessment of fatigue fracture in rolling bearings.

1. Introduction

Rolling bearings are susceptible to numerous forms of damage, including wear, rust, corrosion, denting, electrical corrosion, flaking and fracture[1, 2]. Of these many possibilities, flaking due to rolling-contact fatigue (RCF) usually occurs after a long period of use, even at proper operating conditions[3–6]. Since flaking determines the service life of a rolling bearing, numerous studies have been conducted to improve and quantitatively evaluate flaking life[7–16]. The onset of flaking leads to increased vibration and a concomitant deterioration in positioning accuracy, the incidence of which seldom leads to any critical impairment of the machine as a whole. Notwithstanding, a fracture would ultimately be the most catastrophic damage that results in generating rather serious destruction within peripheral components and even rotation-locking caused by broken parts. Therefore, fracture prevention is among the most crucial issues in the context of the structural integrity of rolling bearings. Although its incidence rate is not so high, the risk of fracture has greatly increased in recent years, due to more severe usage conditions. In general, two kinds of fracture are conceivable: (i) fracture caused by monotonic or impact loading and (ii) fracture due to fatigue. The former can be evaluated based on the fracture-toughness value and the Charpy impact-absorption energy relative to toughness indexes[11, 17–19], the strength-design methods for which have been well established. Regarding the latter, in many cases, fatigue cracks originate at stress concentration sites like small defects (e.g. a flaked surface-pit). Since flaking can occur relatively frequently, even under normal conditions of use, it is vitally important to make a proper risk assessment for the fatal fracture of all bearings, since fatigue crack-propagation originates from flaking.

Three necessary conditions must be satisfied to facilitate the quantitative prediction of such fatigue fracture in bearings: (I) assessment of crack-growth resistance in bearing steel, (II) exposure of fluctuating stress-distribution in bearings and defect/crack-enhanced stress intensity on bearing raceways and (III) inclusion of both crack-growth resistance and stress-state in an adequate mechanical model. Multiple studies have investigated the fatigue-strength properties of bearing steels[20–32], yet few have attempted fatigue-strength evaluation of actual bearings. Regarding (I), for example, Beswick measured the crack-growth rate in a bearing steel at positive stress ratios, using a compact-tension specimen[33]. However, such results obtained at high-stress ratios cannot be applied to relevant problems, since bearing components are generally subjected to cyclic-compressive stress caused by rolling contact. To achieve a quantitative evaluation, a crack's growth/threshold properties at negative stress-ratios are required, the data for which little research exists.

With respect to (II), Kim et al. developed a hypothesis to analyse crack-propagation in a range of bearing sizes, thereby demonstrating the stress intensity factor (SIF) variation during the fracture process[34]. Such a fracture mechanics-based approach was groundbreaking with respect to creating a bearing "failure map", although their analysis was not sufficiently linked to the crack-growth properties of the bearing steel under corresponding loading conditions. Also, the impact of initial defect shapes/dimensions on bearing fatigue-strength has not been explored in existing literature. This should further be elucidated while developing a fracture mechanics-based approach for relevant issues. Concerning (III), Hirakawa et al. proposed a model for reproducing fatigue fracture, as observed in a rolling-bearing raceway with a pre-crack, thus evaluating the fracture resistance of some materials[35]. However, their analysis only examined the inner-ring hoop stress, without considering the impact of rolling-contact stress. Consequently, their model clearly did not accurately describe the mechanical phenomenon in actual effect during the fracture process. As previously noted, due to the shortfall in conditions (I)–(III), extensive criteria for the fracture of bearings have not yet been established.

In this study, using a small bearing, a simple test method was developed to reproduce fatigue fracture from assorted defect shapes and dimensions. In each test condition, stress intensity was analysed via the finite element method (FEM) to evaluate the phenomenon, considering both rolling-contact and fitting conditions. Moreover, crack-growth resistance of bearing steel was measured under different stress ratios, with investigation of crack-opening/closing behaviour. The results offer novel criteria for creating a fracture map for rolling bearings.

2. Experimental Procedure

2.1 Materials and specimens

A cylindrical, JIS-NU206, roller bearing was used for fatigue-testing. The steel grade of the specimen bearing was JIS-SUJ2, the main components of which were 1% carbon and 1.5% chromium. Figure 1A displays the shape and dimensions of the test bearing.

Two kinds of artificial defects were introduced onto the outer-ring raceway. Type A defects were semicircular slits, simulating early-stage flaking, with depths ranging from 0.05–0.15 mm (cf. Figure 1B). On the other hand, Type B defects were through-thickness incisions, replicating deeper cracks, with depths ranging from 1.0–1.8 mm (cf. Figure 1C). Both defect types were generated by electron discharge machining (EDM).

Crack-growth testing was also conducted on JIS-SUJ2, the chemical composition of which was 1.02C-0.27Si-0.39Mn-0.022P-0.008S-1.39Cr (mass %), balanced with Fe. Rectangular plate-specimens (cf. Figure 2A) were fabricated from a round bar of 75 mm in diameter, with care taken to avoid the central region (cf. Figure 2B). The plates were heat-treated at 1113 K for 1 h, then quenched in an oil bath and finally tempered at 473 K for 1.5 h. Subsequently, a parallel grinder was used to remove a surface oxidation layer, then a 3 mm deep notch was added via EDM as a crack-starter.

To measure fatigue crack-closure behaviour during tension-compression fatigue tests, JIS-SUJ2 was also supplied, containing 1.00 C-0.27 Si-0.36 Mn-0.014 P-0.006 S-1.41Cr (mass %), balanced with Fe. Figure 3A exhibits the shape and dimensions of the specimen, fabricated from a round bar of 22 mm in diameter. After rough machining, the material was heat-treated at 1113 K for around 1.5 h, followed by oil-quenching and tempering at 473K for 2 h. Thereafter, the specimen was machined to the final shape. The specimen surface was polished with emery papers and buffed with a diamond paste, then the surface layer was electro-polished at 40 µm per diameter, using a liquid consisting of 2 L of phosphoric acid, 40 g of oxalic acid and 40 g of gelatin. A semicircular notch was later introduced by EDM onto the specimen surface, as shown in Figure 3B.

Regarding the materials used in the tension-compression and four-point bending tests, it must be noted that their heat-treatment conditions were specifically determined so that their hardness values corresponded to those of the bearing test samples. Hence, Rockwell hardness values of all materials fell within the range of HRC 60–62.

2.2 Fatigue tests

2.2.1 Bearing test

The bearing test is schematically illustrated in Figure 4. VG68 viscosity-grade machine oil was continuously supplied via a forced circulating style (cf. Figure 4A). The bearing load was applied to the outer ring in a radial direction through the housing (cf. Figure 4B). The outer ring was positioned to ensure that the defect was located in the load-zone centre. In all tests, the bearing load was 8.0 kN and the rotation speed was 500 rpm. The bearing load generates a rolling-element load, caused by each rolling element in action on the raceway (cf. Figure 4C), variable depending on their circumferential position. The

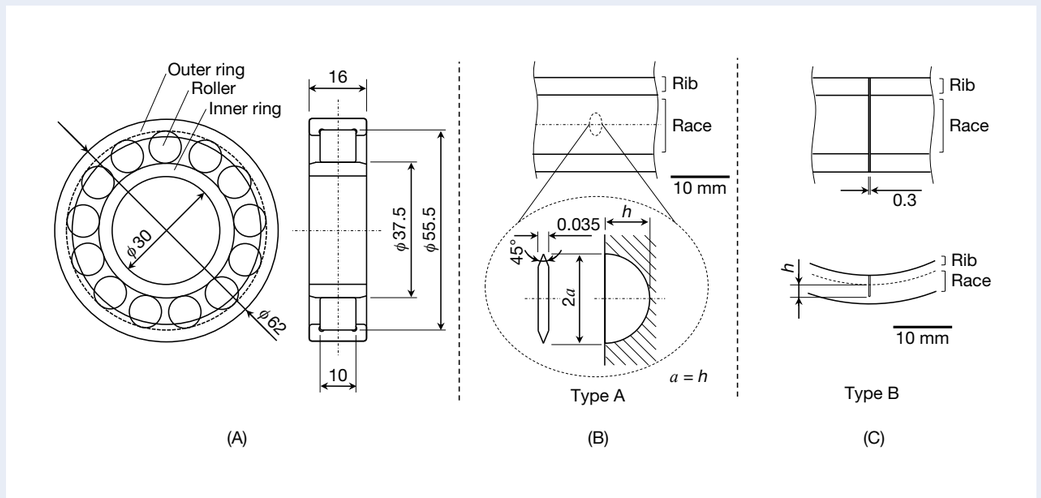

Fig. 1 Shape and dimensions of bearing test specimen, in mm: (A) test bearing NU206, (B) Type A defect, (C) Type B defect

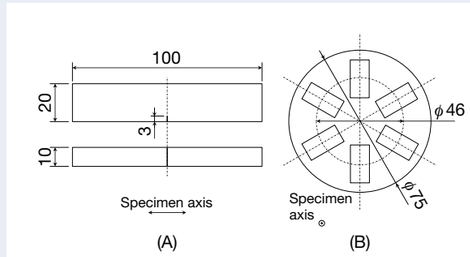

Fig. 2 Shape and dimensions (in mm) of the four-point bending test specimen: (A) rectangular specimen, (B) position from which rectangular plates were extracted from the round steel bar

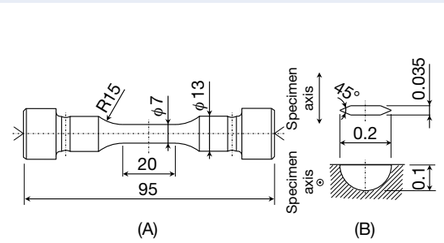

Fig. 3 Shape and dimensions (in mm) of the tension-compression test specimen: (A) round-bar fatigue specimen, (B) the artificial defect

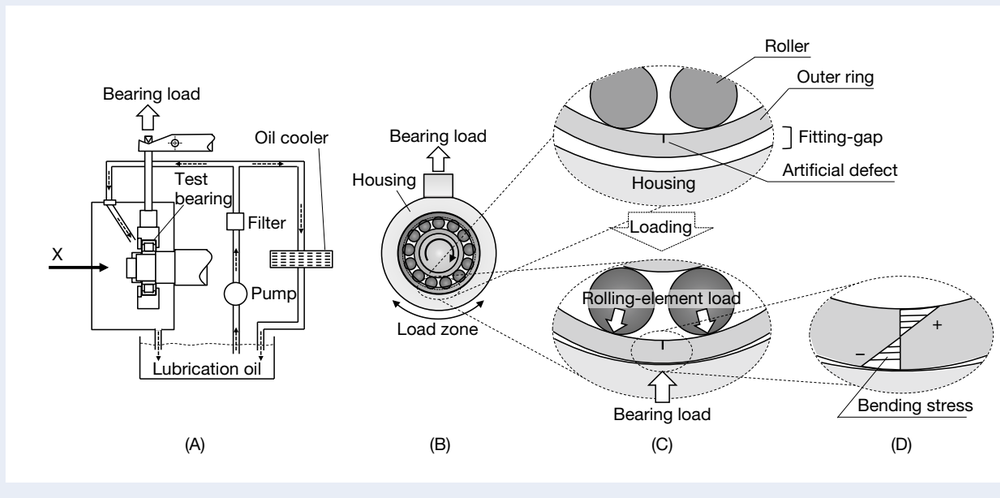

Fig. 4 Schematic of the bearing fatigue test: (A) test rigs for cylindrical roller bearings, (B) the housing and test bearing (magnified view of arrow X), (C) the fitting-gap and rolling-element load, (D) bending-stress on the raceway

utmost, rolling-element load was calculated as 2.8 kN, matching the maximum contact stress of 1.7 GPa, with a half-contact width of 0.11 mm[36–38]. The fitting-gap and outer-ring load conditions are shown in Figure 4C, D. The fitting-gap has been defined as the difference between the inner housing radius and the exterior outer-ring radius. In this study, the fitting gap was modified by altering the interior housing diameter so as to vary bending stress. In actual rolling bearings, the fracture process can be accelerated by an inadequately loose fitting. Specifically, a loose fitting is caused occasionally by severe housing wear and/or by housing stiffness-decay due to oil-circulation grooves/holes. Therefore, to simulate these effects, bearing tests were conducted under a few loose-fitting conditions, whereby the fitting gap for bearings with Type A defects was 0.5 or 1.0 mm, while that for bearings with Type B was 0.2 or 0.5 mm.

2.2.2 Four-point bending test

To measure crack-growth resistance, four-point bending tests were conducted in ambient air at room temperature, using a servo-hydraulic, fatigue-testing machine at a stress ratio, R, of 0.1, 0.3 or 0.5, and a test frequency of 60 Hz. The crack-arrest point was determined via the ΔK-decreasing test after pre-crack introduction. The ΔK that corresponds to a growth rate less than 2×10^{-8} mm/cycle was defined as ΔK_{th} in this test. Crack-length was monitored and assessed via the direct current potential drop (DCPD) technique. After fatigue-testing, the estimated crack-length was duly corrected by means of the observed fracture-surface beach marks.

2.2.3 Tension-compression fatigue test

Tension-compression fatigue tests were performed at R of –1 or –3, in ambient air at room temperature. During testing, crack-length was measured using the plastic replica method, by which ΔK was calculated with the following equation[39]:

$$\Delta K = 2 \times 0.65 \cdot \sigma_a \sqrt{\pi \sqrt{area}} \quad \cdots\cdots (1)$$

where, σ_a is stress amplitude and $\sqrt{area}$ is the square root of the crack-area. Since the $\sqrt{area}$ of a growing crack is unknown during fatigue-testing, it was calculated based on crack-length, assuming that the crack was semicircular in shape. After the crack-length reached a certain level, ΔK was gradually decreased by a declining rate of ≈ 50 000 MPa/$\sqrt{m}$ (i.e. ≈ 1 MPa$\sqrt{m}$ per 20 µm of growth), resulting in arrested crack-growth at an approximate crack-length of 500 µm. It is noted that the crack was defined as an arrested crack when the growth was less than 0.01 mm in 2×10^6 cycles. Hereafter, the cracks that satisfy this definition are referred to as a non-propagating cracks. Subsequently, the fatigue crack-growth threshold was ascertained using the following equation:

$$K_{max\ th} = 0.65 \cdot \sigma_{max\ th} \sqrt{\pi \sqrt{area}} \quad \cdots\cdots (2)$$

where, $\sigma_{max\ th}$ is the maximum stress at which a crack stopped propagating.

When crack-propagation halted, crack-closure behaviour was investigated using the elastic unloading compliance method[40]. Two strain gauges (0.2 mm long and 1.4 mm wide) were attached to the gauge section: the centre of one gauge was set precisely at the crack centre, while the other was placed on the smooth section beyond the crack. The strain difference (so-called subtracted strain) was then plotted as a function of nominal stress. The diagram generally consists of two different lines corresponding to crack-opening/closing processes, with the latter's knee point viewed as the crack-closure point[41,42]. Essentially, the diagram was fixed so the straight line in an upper part of the curve could become upright, enabling the crack-closing point to be determined precisely[40], as is later depicted in Figure 10. Both the effective stress range, $\Delta\sigma_{eff}$, and effective SIF range, ΔK_{eff}, were calculated using the following equations:

$$\Delta\sigma_{eff} = \sigma_{max} - \sigma_{cl} \quad \cdots\cdots (3)$$

$$\Delta K_{eff} = 0.65 \cdot \Delta\sigma_{eff} \sqrt{\pi \sqrt{area}} \quad \cdots\cdots (4)$$

It is noted that, in the calculation of $K_{max\ th}$ and ΔK_{eff}, $\sqrt{area}$ was assessed via fractographic observation by breaking the specimen at a cryogenic temperature after the crack-closure evaluation.

2.3 Method of analysis

During bearing tests, SIF fluctuations of outer-ring cracks were established with FEM. Calculations were implemented with two-dimensional models via MSC Marc/Mentat® software version 2014.1.0, using the QUAD and TRI plane-strain elements. Young's modulus and Poisson's ratio of the outer ring were determined as 208 GPa and 0.3, respectively. Housing and rolling elements were modeled as rigid bodies since their stiffness negligibly affected the SIF.

For the cases of Type A defects, bending-stress distribution in the outer ring without defect was first computed. Then, based on the assumption that a defect is mechanically equivalent to a crack[39], the SIF was calculated according to the approximate analytical solution for a surface crack under remote stress, σ_0, as expressed by the following equation:

$$K_I = 0.65\ \sigma_0 \sqrt{\pi \sqrt{area}} \quad \cdots\cdots (5)$$

Regarding Type B defects, the J-integral method[43] was applied for SIF-calculation. A circular area around the crack tip was divided radially into eight layers, for which eight orbital paths were created. The SIF was based on the average of six J-integral values obtained from second to seventh paths, via the following equation:

$$J = K_I^2 / E' \quad \cdots\cdots (6)$$

where, $E' = E$ for plane stress and $E' = E/(1 - \nu^2)$ for plane strain[44].

3. Results and Discussion

3.1 Results of stress analyses

3.1.1 Stress analysis for artificial defects on the bearing raceway

Circumferential, normal-stress distributions relative to depth direction are featured in Figure 5, which was used for calculating the SIF of Type A defects. The corresponding roller positions 1 and 2 are also depicted in the figure. In position 1, two rollers are located furthest from the artificial defect, at the point where tensile bending stress on the raceway is maximized. On the other hand, in position 2, a roller is located directly on the artificial defect, at the point where compressive stress from contact is superposed onto the tensile bending stress, thereby maximizing compressive stress on the raceway.

Using the J-integral method, the accuracy of SIF-calculation was evaluated using a simple error verification model, whereby a rectangular cross section with a through-thickness crack displayed variations in crack-depth ratio and minimum mesh-size (*MMS*) at the crack tip. The difference between the K_I values obtained via the J-integral method and those derived from a solution by body force doublet method under pure bending was considered to be the error. K_I is expressed by the following formula[45]:

$$K_I = \frac{3Pl}{tW^2} \sqrt{\pi a} \cdot F_{IM}\left(\frac{a}{W}\right) \quad \cdots\cdots (7)$$

where,

$$F_{IM}\left(\frac{a}{W}\right) = 1.122 - 1.121\left(\frac{a}{W}\right) + 3.740\left(\frac{a}{W}\right)^2 + 3.873\left(\frac{a}{W}\right)^3 - 19.05\left(\frac{a}{W}\right)^4 + 22.55\left(\frac{a}{W}\right)^5$$

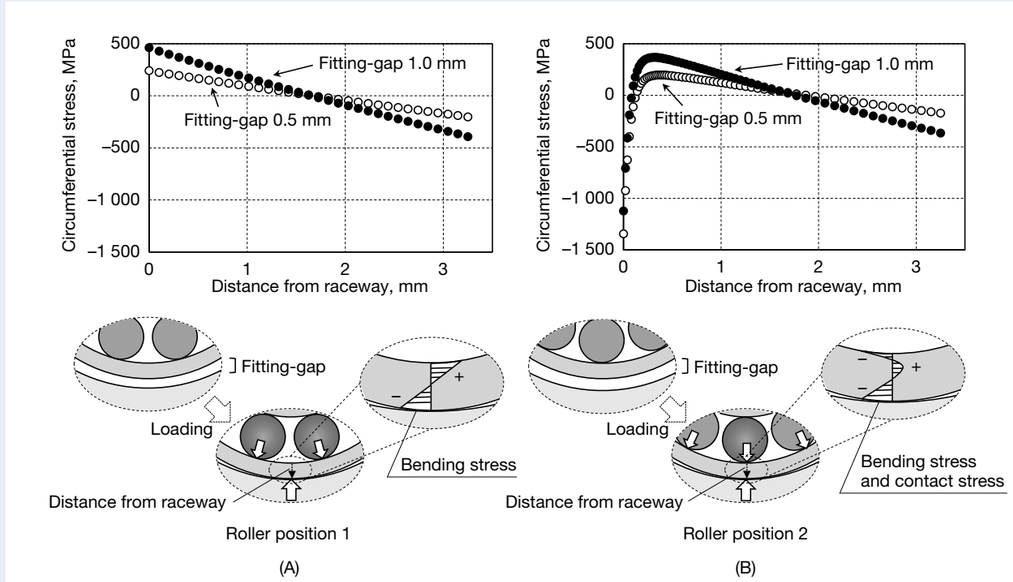

Fig. 5 Various gaps representing circumferential stress-distribution in the outer ring: (A) roller position 1, (B) roller position 2

Crack-depth values (*CD*) and *MMS* detected in error-verification models are documented in Table 1, along with the resultant K_I errors.

With an escalation in *MMS*/*CD*, the error tends to intensify. In this study, the K_I of the real bearing ring was calculated within the range of the *MMS*/*CD* listed in Table 1 (i.e. *MMS*/*CD* < 8%). Therefore, it was deduced that the model calculation error was less than 2.4%, sufficiently ensuring the calculation accuracy of the *J*-integral method.

Table 2 lists the SIFs and stress ratios in diverse test conditions for initial Type A and Type B defects, where defects were regarded as cracks with similar dimensions. The initial SIF range, $\Delta K_{initial}$, and stress ratio, $R_{initial}$, were respectively arranged from 3.1 to 10.7 MPa$\sqrt{m}$ and from –3.7 to 0.6.

3.1.2 SIF in the bearing crack-growth process

Aided by FEM, stress analyses were realized on through-thickness cracks, so as to reveal the stress-intensity variation of crack-growth from a Type B defect. It is noted that the analysis method conformed to that for Type B defects as specified in Section 3.1.1. Thus, the error verification as represented in Table 1 can be applicable also to this calculation. Figure 6 presents the calculation results for K_{min}, K_{max}, ΔK and R, as functions of a/W. Regarding the fitting-gap of 0.5 mm, K_{max} increased gradually with extended crack-length, for which K_{min} was maximized at $a/W \cong 0.4$. Consequently, the ΔK gradually augmented as crack-length expanded, while R slightly decreased with simultaneous crack-length extension. Notwithstanding, regarding the 0.2 mm fitting-gap, variation trends of K_{min}, K_{max} and ΔK were similar to that of the 0.5 mm fitting-gap, with their variation ranges becoming smaller. It is also noteworthy that R peaked at $a/W \cong 0.4$ for the 0.2 mm fitting-gap. Thus, in a rather complex fashion, the SIF range and stress ratio vary, depending on the fitting-gap and crack-length. Consequently, to quantitatively evaluate bearing fatigue strength, such variations should be taken into account, as will be discussed later in Section 3.3.

The smallest artificial defect used in this research was $\sqrt{area}$ = 0.06 mm. Where microscopic cracks are concerned, it is understood that when the small-scale yielding condition is not satisfied, a linear-elastic fracture mechanics (LEFM)-based approach becomes invalid. In such a case, the ΔK_{th} is less significant than for a long crack, decreasing with crack-size reduction[46, 47]. According to Chapetti et al., the small/large crack-transition size

Table 1 Crack-depth values and minimum mesh-sizes (*MMS*) resulting from the error-verification models and the resultant K_I errors

Crack-depth (*CD*) mm	Minimum mesh size (*MMS*) mm	*MMS*/*CD* %	K_I error %
6	0.024	0.4	0.46
6	0.10	1.7	0.86
6	0.48	8.0	2.4
10	0.10	1.0	0.67
14	0.10	0.7	1.1

Table 2 Bearing test-conditions and results of stress intensity factor (SIF) calculations

Defect-type	*h* mm	Fitting-gap mm	$\sqrt{area}$ mm	$K_{max\ initial}$ MPa$\sqrt{m}$	$K_{min\ initial}$ MPa$\sqrt{m}$	$\Delta K_{initial}$ MPa$\sqrt{m}$	$R_{initial}$
A	0.05	0.5	0.063	2.2	–8.1	10.3	–3.7
	0.05	1.0	0.063	4.1	–6.1	10.3	–1.5
	0.10	0.5	0.13	3.0	–7.7	10.7	–2.6
	0.10	1.0	0.13	5.8	–5.0	10.7	–0.9
	0.15	0.5	0.19	3.6	–6.5	10.1	–1.8
	0.15	1.0	0.19	6.9	–3.2	10.1	–0.5
B	1.0	0.2		5.3	2.2	3.1	0.4
	1.0	0.5		12.0	7.3	4.7	0.6
	1.8	0.2		6.4	2.4	4.0	0.4
	1.8	0.5		14.6	6.4	8.2	0.4

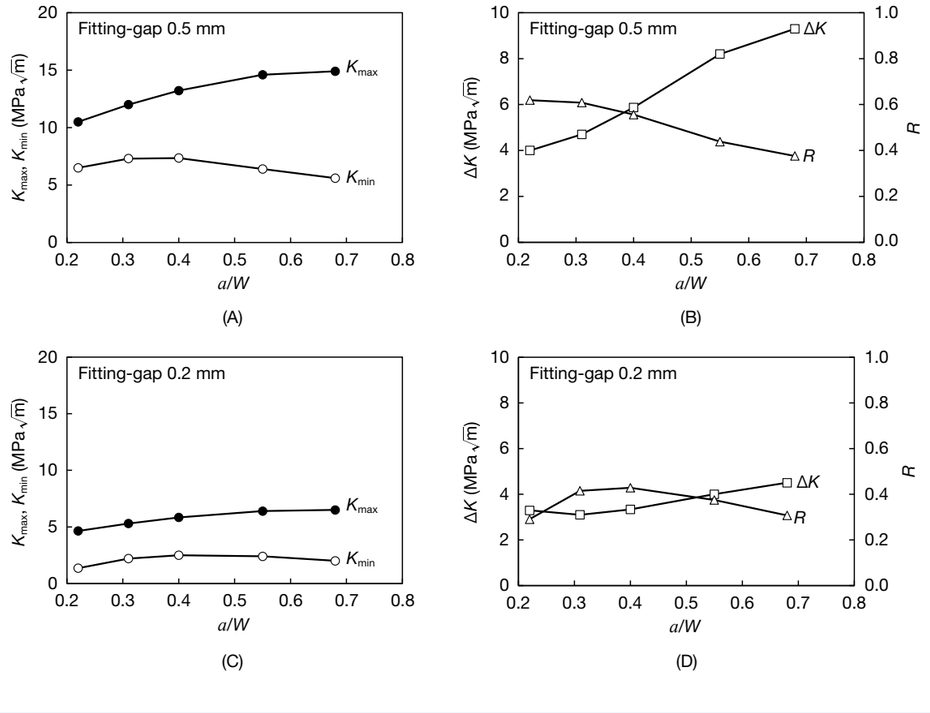

Fig. 6 Results of stress intensity factor (SIF) calculations: (A, B) fitting-gap = 0.5 mm, (C, D) fitting-gap = 0.2 mm

is more or less dependent on *HV*, i.e., the higher the *HV*, the smaller the transition size[48]. Åman et al. reported the transition size in bearing steels of *HV* ≈ 700 to be about 0.05 mm in $\sqrt{area}$[49], less than the smallest $\sqrt{area}$ of an artificial defect used in this study (i.e. 0.06 mm). Therefore, in the following sections, all cracks/defects are considered to be large cracks.

3.2 Results of fatigue tests

3.2.1 Fatigue tests of bearings

Table 3 lists the bearing test results. The loading cycles, *N*, were defined as the number of passes effected by the rolling element over the defect. In total, 10 specimens were tested under diverse conditions, five of which were broken, with the rest being run-out over *N* of 3.9×10^7 to 1.5×10^8 cycles. Of the six different tests with Type A defects (semicircular slits), two specimens tested with a 1.0 mm fitting-gap were broken, whereas the others survived. However, out of the four tests with Type B defects (through-thickness slits), only one specimen survived. It possessed a 1.0 mm deep defect and was tested with a 0.2 mm fitting-gap. It is noted that, in the two tests denoted by asterisks in Table 3, specimens were classified as broken since crack lengths reached 0.6–1.0 mm as measured from the notch root after the fatigue tests.

Figure 7 displays an example of the fracture surface and cross section of a broken specimen with a Type B defect (*h* = 1.0 mm, fitting-gap = 0.5 mm). Figure 7C features a crack that initiated near the notch-bottom, later propagating obliquely. Similarly, in specimens with Type B defects, cracks originated in the vicinity of the notch-bottom, rather than specifically at the notch-bottom itself, propagating obliquely, with a random scattering in the crack-path. On the other hand, in specimens with Type A defects, cracks started at defect-tips, later growing in a roughly radial direction.

To investigate the mechanistic reason for seemingly peculiar crack-path for Type B defect, an FEM stress analysis was performed using a two-dimensional, plane-strain model, with the notch subjected to rolling-contact loading. The variation of normal stress along the notch-root surface was calculated at assorted roller positions.

Table 3 Results after fracture-testing of bearings (results are supplemental to Table 2)

Defect-type	h mm	Fitting-gap mm	$\sqrt{area}$ mm	$K_{max\ initial}$ MPa$\sqrt{m}$	$K_{min\ initial}$ MPa$\sqrt{m}$	$\Delta K_{initial}$ MPa$\sqrt{m}$	$R_{initial}$	Test result	Loading cycles
A	0.05	0.5	0.063	2.2	–8.1	10.3	–3.7	Unbroken	3.9×10^7
	0.05	1.0	0.063	4.1	–6.1	10.3	–1.5	Unbroken	1.5×10^8
	0.10	0.5	0.13	3.0	–7.7	10.7	–2.6	Unbroken	3.9×10^7
	0.10	1.0	0.13	5.8	–5.0	10.7	–0.9	Broken*	1.1×10^8
	0.15	0.5	0.19	3.6	–6.5	10.1	–1.8	Unbroken	3.9×10^7
	0.15	1.0	0.19	6.9	–3.2	10.1	–0.5	Broken	4.6×10^7
B	1.0	0.2		5.3	2.2	3.1	0.4	Unbroken	4.2×10^7
	1.0	0.5		12.0	7.3	4.7	0.6	Broken	1.1×10^7
	1.8	0.2		6.4	2.4	4.0	0.4	Broken*	4.1×10^7
	1.8	0.5		14.6	6.4	8.2	0.4	Broken	9.8×10^5

*The specimens were deemed to be broken after the discovery of a propagated crack after the test.

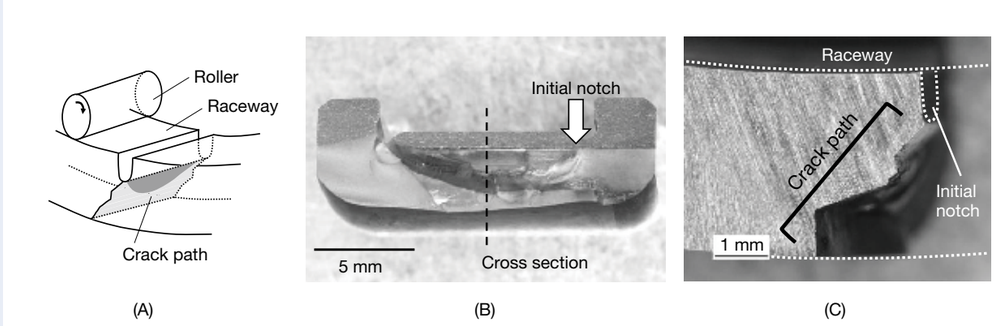

Fig. 7 Fractured outer ring having Type B defect: (A) schematics of fracture surface, (B) picture of the fracture surface, (C) picture of the cross section

Figure 8 reproduces the distribution of maximum stress, minimum stress, and stress range in a circumferential direction along the notch-root surface; σ_{max}, σ_{min} and $\Delta\sigma$, where the position is represented by the angle, θ (cf. illustrative definition in Figure 8). The difference between σ_{max} and σ_{min} represents the stress range, $\Delta\sigma$, a dominant parameter in fatigue crack-initiation. The $\Delta\sigma$ slightly varied with θ, peaking at $\theta \approx \pm 40°$. However, considering the broken bearing presented in Figure 7, the crack-initiation site was at $\theta \approx 75°$, where the $\Delta\sigma$ value was 11% lower than the maximum. It is difficult to accurately predict the crack-initiation site, since crack-initiation can also be dominated by the stress ratio that varies with θ. Furthermore, the crack-initiation site can be influenced by a microstructural irregularity near the notch-bottom. Consequently, as previously showcased, under gentle distribution of stress range and stress ratio in the notch-bottom region, the crack-initiation site was not always exactly at notch-bottom, leading to scatter of the crack-growth direction early in the fracture process. Accordingly, to assess the bearing fatigue-limit in this study, the through-thickness notches (i.e. Type B defects) were assumed to be cracks, thus rendering evaluation both simple and conservative.

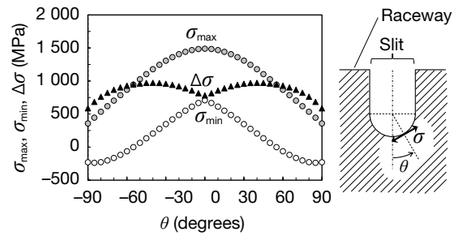

Fig. 8 Circumferential stress-distribution along the notch-root surface

3.2.2 Four-point bending tests

Figure 9 showcases the fatigue crack-growth curves and fracture surfaces, as analysed during four-point bending tests. Arrow marks on the fracture surfaces indicate the crack tip positions at which the ΔK-decreasing tests were launched and terminated. It was reported that, in high-strength steels as well as in low- and medium-strength steels, the ΔK_{th} decreased with an amplified R, becoming constant at a high R (e.g. $R > 0.7$)[50], where the crack-closure effect disappeared[51, 52]. By contrast, the ΔK_{th} in this test appears to be nearly independent of load ratio with a considerable scatter. The result infers that, in the present material, there is little influence of crack closure on the rate and threshold of crack-growth in the R range of 0.1–0.5. A dark section is discernible on the fracture surface in Figure 9, the area of which becomes less prominent with increased R. It is presumed that this was generated due to the repeated contact of mating fracture-surfaces, reflecting a presence of crack-closure at the R of 0.1 and 0.3 even though its influence is insignificant.

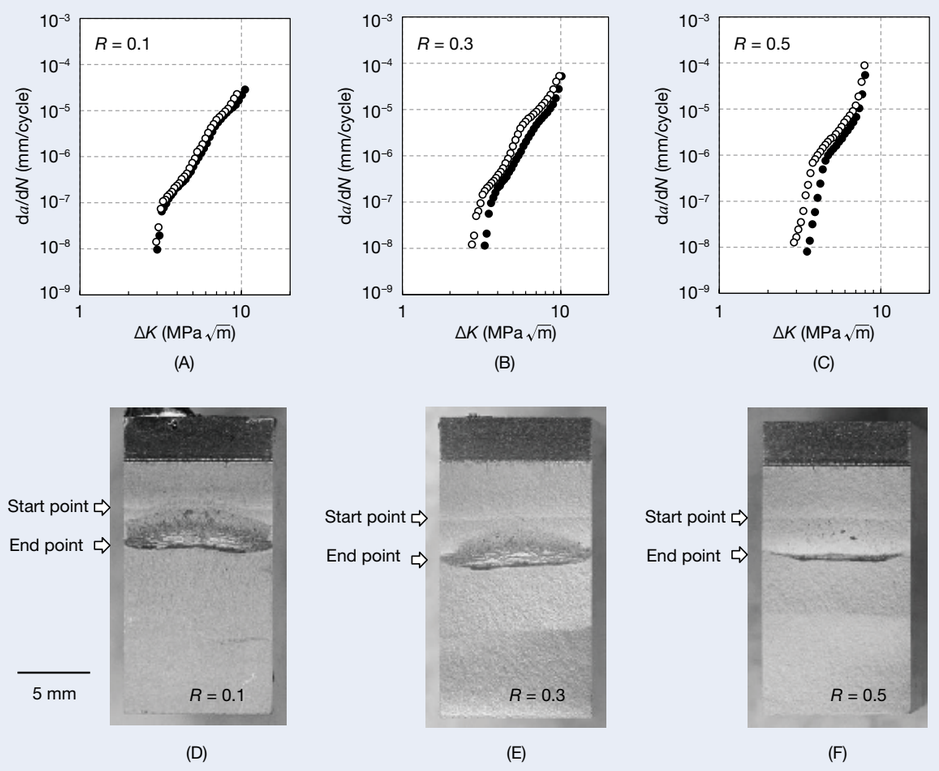

Fig. 9 Fatigue crack-growth curves and fracture surfaces: (A, D) stress ratio, R = 0.1; (B, E), R = 0.3; (C, F), R = 0.5

3.2.3 Crack-closure measurement by tension-compression fatigue-testing

Figure 10A, B display the crack-closing behaviour for non-propagating cracks in round-bar specimens under unloading processes, at R of –1 and –3, whereby a pre-crack was introduced via an ΔK-decreasing test. Figure 10C,D also exhibit the results of stress-constant tests at R of –5 and –10, based on data obtained during the authors' previous study[40], in which a pre-crack was introduced via the ΔP-constant test. Apart from the curves, the thick short lines pinpoint the crack-closure starting points during the unloading process, determined as the point of 0.1% deviation from the straight vertical line in the curve's higher-stress regime. The sizes and shapes of non-propagating cracks were measured by SEM observation of fracture surface after breaking the specimen at a cryogenic temperature, as depicted in Figure 10, from which $K_{\max\,th}$, K_{cl} and $\Delta K_{eff\,th}$ were calculated by using Equation 5. $K_{\max\,th}$ represents the maximum threshold SIF, while K_{cl} signifies the crack-closure start-point during the crack-closing process and $\Delta K_{eff\,th}$ is the effective threshold SIF range.

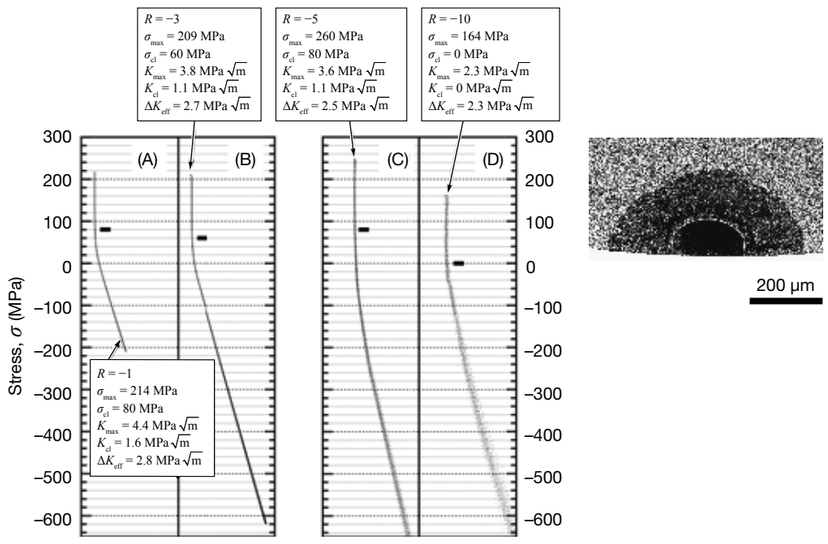

Fig. 10 Crack-closing behaviour at stress ratios R = –1, –3, –5 and –10, with an SEM image of a non-propagating crack at R = –1

Table 4 lists the values obtained for $K_{\max\,th}$, K_{cl} and $\Delta K_{eff\,th}$. Figure 11 depicts K_{cl} and $\Delta K_{eff\,th}$ as functions of (1–R). Also plotted in Figure 11B are average values of ΔK_{th}, calculated based on the four-point bending tests. The K_{cl} value was linearly reduced with an augmentation in (1–R), for which an approximate equation was defined, using the least-squares method (Figure 11A). The $\Delta K_{eff\,th}$ has been reported to be a material constant of a large crack[53]. However, the $\Delta K_{eff\,th}$ tends to decrease slightly with respect to (1–R), (cf. solid black circles in Figure 11B). A plausible reason would be the greater, local compressive strain at a lower stress ratio, caused by reverse yielding at the crack tip, possibly affecting local crack-closure behaviour, although it cannot be detected by the strain-gauge measurement. Thus, in the following discussion, such a slight $\Delta K_{eff\,th}$ variation is ignored, while the average value, $\Delta K_{eff\,th}$ = 2.6 MPa$\sqrt{m}$, is used as the material constant. Consequently, as demonstrated in Figure 11A, the K_{cl} values can be expressed accordingly:

$$K_{cl} = -0.17\,(1-R) + 2.0\ (\mathrm{MPa}\sqrt{m}) \quad \cdots\cdots (8)$$

Based on the definition, ΔK_{eff} can be expressed as follows[54]:

$$\Delta K_{eff} = K_{max} - K_{cl} \quad (\text{for } K_{min} \le K_{cl}) \quad \cdots\cdots (9)$$

$$\Delta K_{eff} = K_{max} - K_{min} \quad (\text{for } K_{min} > K_{cl}) \quad \cdots\cdots (10)$$

Table 4 Results of crack-closure measurement

R	$2a$ μm	$\sqrt{area}$ μm	$\sigma_{\max\,th}$ MPa	σ_{cl} MPa	$\Delta\sigma_{eff\,th}$ MPa	$K_{\max\,th}$ MPa$\sqrt{m}$	K_{cl} MPa$\sqrt{m}$	$\Delta K_{eff\,th}$ MPa$\sqrt{m}$
–1	521	319	214	80	134	4.4	1.6	2.8
–3	508	245	209	60	149	3.8	1.1	2.7
–5	245	148	260	80	180	3.6	1.1	2.5
–10	288	151	164	0	164	2.3	0	2.3

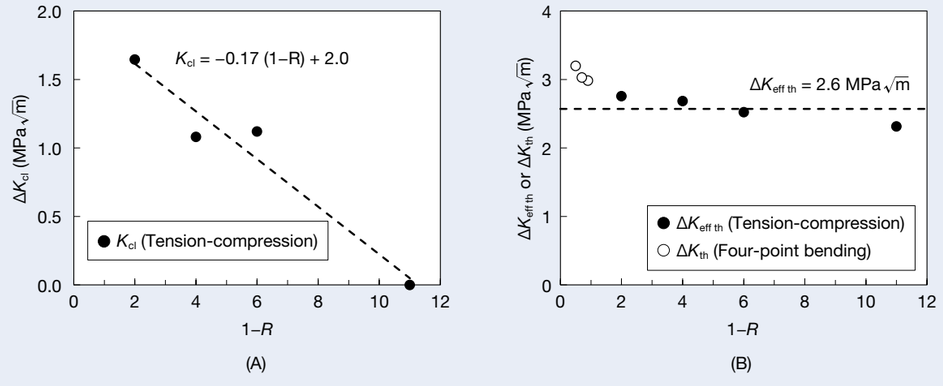

Fig. 11 Results of material tests: (A) K_{cl} via the tension-compression test; (B) $\Delta K_{eff\,th}$ obtained using the tension-compression test and average values of ΔK_{th} acquired with the four-point bending test

3.3 Criteria for fatigue fracture of rolling bearings under the influence of defects

A real fatigue-fracture scenario of a bearing, the actual aim of this study, is summarized as follows. Repeated, rolling-contact stress causes flaking on the raceway, after which flaking itself becomes a detrimental defect. When there exists an outer-ring bending stress due to the fitting-gap, repeated stress around the defect on the raceway surface includes a tension. Thus, if the cyclic-stress condition exceeds the crack-growth threshold, the fatigue fracture process begins, leading to the fracture of bearings. In this section, through the combination of all of the previously mentioned analytical and experimental results, we propose some criteria for the establishment of a failure map for bearings, duly influenced by prevailing defects.

Focusing on the crack-growth threshold, Equations 9 and 10 can be rewritten as:

$$K_{\max\,th} = \Delta K_{\mathrm{eff\,th}} + K_{cl} \quad (\text{for } K_{\min\,th} \le K_{cl}) \qquad \cdots\cdots\cdots (11)$$

$$K_{\max\,th} = \Delta K_{\mathrm{eff\,th}} + K_{\min\,th} \quad (\text{for } K_{\min\,th} > K_{cl}) \qquad \cdots\cdots\cdots (12)$$

As shown in Section 3.2.3, crack-closure significantly impacts the crack-growth threshold in the relatively low R regime. Then, assuming that $K_{\min\,th} \le K_{cl}$, and after substituting Equation 8 into Equation 11, $K_{\max\,th}$, is expressed accordingly:

$$K_{\max\,th} = -0.17\,(1-R) + 4.6 \quad (\text{for } K_{\min\,th} \le K_{cl}) \qquad \cdots\cdots\cdots (13)$$

Conversely, in the relatively high R regime (e.g. $R > 0.7$)[50], crack-closure exerts very little influence on the crack-growth threshold, if at all. Furthermore, assuming that $K_{\min\,th} > K_{cl}$, considering the relationship $R \cdot K_{\max\,th} = K_{\min\,th}$, Equation 12 can be modified as:

$$K_{\max\,th} = \frac{2.6}{1-R} \quad (\text{for } K_{\min\,th} > K_{cl}) \qquad \cdots\cdots\cdots (14)$$

Figure 12 plots the bearing test results, based on the relationship between $K_{\max\,th}$ and $(1–R)$, where R was obtained via FEM analyses in Section 3.1.1. The threshold lines described by Equations 13 and 14 are also drawn in the figure. In addition, as a fracture threshold for monotonic loading, the lower bound of the fracture-toughness scatter, K_{IC}, is revealed in the figure, the value of which was reported as 15 MPa$\sqrt{\mathrm{m}}$ for a large crack in a quenched-and-tempered bearing steel[11].

As evidenced in Figure 12, all results for broken bearings fell above the $K_{\max\,th}$ line, whereas most of the results for unbroken bearings fell below the line (shaded area). As denoted by an asterisk, a single result for an unbroken specimen was plotted slightly above the $K_{\max\,th}$ line. Such an underestimation can more or less arise, since the fatigue limit in a bearing test is not determined by the crack-growth threshold evaluated in this study, but by the crack-initiation threshold at the notch-root. This is because the crack-initiation threshold is sometimes considerably larger than the crack-growth threshold in high-strength steels[40]. From a conservative perspective, despite the possibility of such a prediction error, the fatigue limit of rolling-bearings originating from a defect (e.g. flaking) should always be evaluated within the context of a crack-growth threshold, assuming that a crack exists.

At present, it is noteworthy to mention that the proposed criteria are somewhat incomplete and can potentially be improved. For example, the current formulae do not embrace any environmental impacts (e.g. the effects of solute hydrogen, which can vary depending on loading condition and oil-type). In addition, the applicability of the proposed method to the evaluation of case-hardened components (e.g. carburized and induction-hardened steels) remains unclear, where a residual stress field can affect crack-opening/-closing behaviour. These issues will be the focus of our future research.

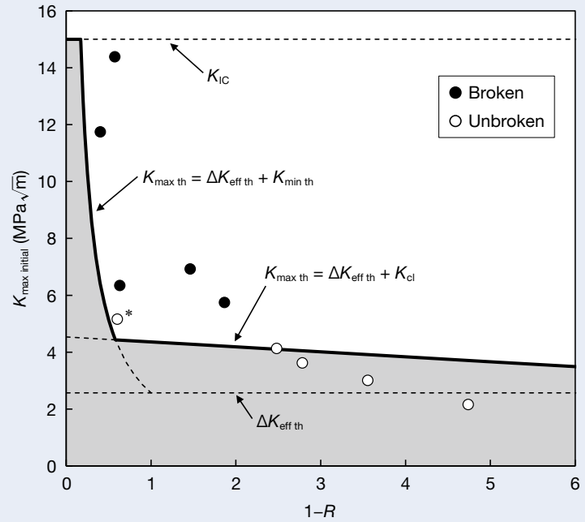

Fig. 12 Results of the bearing fracture-test, in comparison with the maximum stress intensity factor at threshold and fracture toughness

4. Conclusions

In order to establish some criteria for the fatigue fracture of rolling bearings influenced by defects, fatigue tests of rolling bearings with various artificial defects were performed at different stress ratios, as well as stress analyses via FEM and measurements of crack-closure behaviour at fatigue crack-growth thresholds. Some central conclusions are summarized as follows:

1. A simple method was established to reproduce fatigue fracture from defects in rolling bearings.
2. Based on FEM stress analyses, it was manifested that the SIF range and stress ratio vary in a complicated manner, depending on the fitting-gap and crack-size in the bearing.
3. The bearing fracture-threshold originated from its raceway was quantitatively evaluated by considering the crack-closure effect on the fatigue crack-growth threshold. Some novel criteria were thus proposed to establish a failure map to reflect the influence of defects.

Nomenclature

a	half crack-length
a_s	initial crack-length in crack-growth test
a_{th}	threshold crack-length in crack-growth test
$\sqrt{area}$	square root of the defect area
E	Young's modulus
h	depth of defect
J	J-integral
K_I	Mode I stress intensity factor (SIF)
K_{cl}	starting point of crack-closure in the crack-closing process
$K_{I\,max}$	Mode I maximum SIF
$K_{max\,initial}$	maximum SIF for initial defect in the test bearing
$K_{max\,th}$	threshold maximum SIF
$K_{I\,min}$	Mode I minimum SIF
$K_{min\,initial}$	minimum SIF for initial defect in the test bearing
$K_{min\,th}$	threshold minimum SIF
l	half of the difference between short and long span
P	load
R	stress ratio
$R_{initial}$	stress ratio for initial defect in the test bearing
t	specimen thickness
W	specimen width
ΔK	SIF range
ΔK_{eff}	effective SIF range
$\Delta K_{eff\,th}$	effective threshold SIF range
$\Delta K_{initial}$	SIF range for initial defect in the test bearing
ΔK_{th}	threshold SIF range
$\Delta\sigma$	stress range
$\Delta\sigma_{eff\,th}$	stress range at effective threshold
$\Delta\sigma_{eff}$	effective stress range
θ	angle at a notch-tip
ν	Poisson's ratio
σ_0	remote stress
σ_a	stress amplitude
σ_{eff}	effective stress
σ_{max}	maximum stress
σ_{min}	minimum stress
σ_{cl}	crack-closure stress

References

1) R. L. Widner and W. E. Littmann, "Bearing damage analysis," Proceeding of the 20th Meeting of the Mechanical Failures Prevention Group, NBS Special Publication, 423 (1976), pp. 67–83.
2) NSK, "New Bearing Doctor," (2008) NSK Ltd.
3) F. Sadeghi, B. Jalalahmadi, T. S. Slack, N. Raje, and N. K. Arakere, "A review of rolling contact fatigue," *Journal of Tribology*, 131–4 (2009) 041403.
4) G. Lundberg and A. Palmgren, "Dynamic capacity of rolling bearings," IVA Handlingar, (1947) 196.
5) T. A. Harris, "Rolling bearing analysis, 2nd edn." (1984) Wiley.
6) K. L. Johnson, "Contact mechanics," (1987) Cambridge University Press.
7) N. Mitamura, "Rolling Contact Fatigue of Rolling Bearings and the Research Trend," *Journal of Japanese Society of Tribologists*, 53–10 (2008), pp. 641–646.
8) M.-H. Evans, A. D. Richardson, L. Wang, and R. J. K. Wood, "Effect of hydrogen on butterfly and white etching crack (WEC) formation under rolling contact fatigue (RCF)," Wear, 306.1–2 (2013), pp. 226–241.
9) A. A. Walvekar and F. Sadeghi, "Rolling contact fatigue of case carburized steels," *International Journal of Fatigue*, 95 (2017), pp. 264–281.
10) K. Furumura, T. Abe, and Y. Murakami, "Progress in Through-Hardening Bearing Steels: User's Experience," Bearing Steels: Into the 21st Century, (1998) ASTM International.
11) H. K. D. H. Bhadeshia, "Steels for bearings," *Progress in Materials Science*, 57–2 (2012), pp. 268–435.
12) K. Tsubota, "High Carbon Chromium Bearing Steels," Sanyo Technical Report, 5–1 (1998), pp. 105–112.
13) A. Adachi, "Heat treatment of rolling bearings," *Journal of the Japan Society for Precision Engineering*, 46–10 (1980), pp. 1,242–1,247.
14) H. Komata, J. Yamabe, Y. Fukushima, and S. Matsuoka, "Proposal of Rolling Contact Fatigue Crack Growth Test Using a Specimen with a Small Artificial Hole," *Trans Jpn Soc Mech Eng A*, 78–793 (2012), pp. 1,250–1,265.
15) H. Komata, J. Yamabe, H. Matsunaga, Y. Fukushima, and S. Matsuoka, "Effect of Size and Depth of Small Defect on the Rolling Contact Fatigue Strength of a Bearing Steel SUJ2," *Trans Jpn Soc Mech Eng A*, 79–803 (2013), pp. 961–975.
16) S. Hashimoto, H. Komata, S. Okazaki, and H. Matsunaga, "Quantitative Evaluation of the Flaking Strength of Rolling Bearings with Small Defects as a Crack Problem," *International Journal of Fatigue*, 119 (2019), pp. 195–203.
17) M. Goto, "Development of Long Life Case-Hardened Bearing Steel with Rust Resistance," *JTEKT Engineering Journal*, 1004 (2007), 22–26.
18) Y. Hiratsuka, K. Yamamoto, and Y. Minamino, "Technological development of high-toughness hyper-eutectoid steel," Sanyo Technical Report, 24–1 (2017), pp. 52–54.
19) X. Lu, D. Qian, W. Li, and X. Jin, "Enhanced toughness of bearing steel by combining prior cold deformation with martensite pre-quenching and bainite transformation," Materials Letters, 234 (2019), pp. 5–8.
20) K. Shiozawa, L. Lu, and S. Ishihara, "S–N curve characteristics and subsurface crack initiation behaviour in ultra-long life fatigue of a high carbon-chromium bearing steel," *Fatigue & Fracture of Engineering Materials & Structures*, 24–12 (2001), pp. 781–790.
21) E. Kerscher, K.-H. Lang, and D. Löhe, "Increasing the fatigue limit of a high-strength bearing steel by thermomechanical treatment," *Materials Science and Engineering A*, 483 (2008), pp. 415–417.
22) T. Karsch, H. Bomas, H. W. Zoch, and S. Mändl, "Influence of hydrogen content and microstructure on the fatigue behaviour of steel SAE 52100 in the VHCF regime," *International Journal of Fatigue*, 60 (2014), pp. 74–89.
23) Y. Murakami, "Material defects as the basis of fatigue design," *International Journal of Fatigue*, 41 (2012), pp. 2–10.
24) S. Fujita, S. Matsuoka, Y. Murakami, and G. Marquis, "Effect of hydrogen on mode II fatigue crack behavior of tempered bearing steel and microstructural changes," *International Journal of Fatigue*, 32–6 (2010), pp. 943–951.
25) K. Mori, M. Enomoto, and H. Yoshinari, "Effects of microstructure on fatigue crack growth of bearing steel," Proceedings of the JSMS Annual Meetings, 43 (1994), pp. 17–18.
26) H. S. Cheng, L. M. Keer, and T. Mura, "Analytical modelling of surface pitting in simulated gear-teeth contacts," *SAE Transactions*, (1984), pp. 987–995.
27) Y. Murakami, M. Kaneta, and H. Yatsuzuka, "Analysis of surface crack propagation in lubricated rolling contact," ASLE TRANS, 28–1 (1985), pp. 60–68.
28) A. F. Bower, "The influence of crack face friction and trapped fluid on surface initiated rolling contact fatigue cracks," *J Tribol-T ASME*, (1988), pp. 704–711.
29) M. Ozen, "Analysis of a surface crack subject to a rolling/sliding contact," *SAE Transactions*, (1989), pp. 1,375–1,382.
30) K. Furumura, Y. Murakami, and T. Abe, "Case-hardening medium carbon steel for tough and long life bearing under severe lubrication conditions," *Bearing Steels: Into the 21st Century*, (1998), ASTM International.
31) D. P. Townsend, R. J. Parker, and E. V. Zaretsky, "Evaluation of CBS 600 carburized steel as a gear material," (1979).
32) D. P. Townsend and E. V. Zaretsky, "Endurance and Failure Characteristics of Modified Vasco X-2, CBS 600 and AISI 9310 Spur Gears," *Journal of Mechanical Design*, 103–2 (1981), pp. 506–513.
33) J. M. Beswick, "Fracture and fatigue crack propagation properties of hardened 52100 steel," *Metallurgical Transactions A*, 20–10 (1989), pp. 1,961–1,973.
34) T. H. Kim, A. V. Olver, and P. K. Pearson, "Fatigue and fracture mechanisms in large rolling element bearings," *Tribology Transactions*, 44–4 (2001), pp. 583–590.
35) K. Hirakawa, N. Ikeda, S. Okita, and A. Kiuchi, "Inner Ring Fracture Characteristic under Rolling Contact," *NSK Technical Journal*, 658 (1994) 1.
36) T. A. Harris, "Rolling bearing analysis," (2001) John Wiley and sons.
37) "Rolling Bearing Engineering," (1975) Yokendo.
38) J. Okamoto, "Ball Bearing Design Calculation Introduction," (2011) Yokendo.

39) Y. Murakami, “Metal fatigue: effects of small defects and nonmetallic inclusions,” (2019) Academic Press.
40) K. Wada, A. Abass, S. Okazaki, Y. Fukushima, H. Matsunaga, and K. Tsuzaki, “Fatigue Crack Threshold of Bearing Steel at a Very Low Stress Ratio,” *Procedia Structural Integrity*, 7 (2017), pp. 391–398.
41) W. Elber, “The significance of fatigue crack closure,” Damage tolerance in aircraft structures, (1971) ASTM International.
42) Y. Kondo, C. Sakae, M. Kubota, and T. Kudou, “The effect of material hardness and mean stress on the fatigue limit of steels containing small defects,” Fatigue Fract Eng M, 26–8 (2003), pp. 675–682.
43) Marc® “2014.1 Volume A: Theory and User Information,” (2015) MSC Software Corporation.
44) T. L. Anderson, “Fracture mechanics: fundamentals and applications,” (2005) CRC Press.
45) Y. Murakami, “Stress intensity factors,” (1987).
46) Y. Murakami, “Introduction to Stress Concentration,” (2005).
47) K. Tanaka, “The Propagation of Small Fatigue Cracks,” *J Soc Mater Sci Japan*, 33–371 (1984), pp. 961–972.
48) M. D. Chapetti, T. Tagawa, and T. Miyata, “Ultra-long cycle fatigue of high-strength carbon steels part II: estimation of fatigue limit for failure from internal inclusions,” *Materials Science and Engineering A*, 356.1–2 (2003), pp. 236–244.
49) M. Åman, K. Wada, H. Matsunaga, H. Remes, and G. Marquis, “The influence of interacting small defects on the fatigue limits of a pure iron and a bearing steel,” *International Journal of Fatigue*, 135 (2020), p. 105,560.
50) R. O. Ritchie, “Near-threshold fatigue crack propagation in ultra-high strength steel: influence of load ratio and cyclic strength,” (1976).
51) Y. Nakai, K. Tanaka, and R. Kawashima, “Stress-Ratio Effect on Fatigue Crack Growth Threshold in Steels,” *J Soc Mater Sci Japan*, 33–371 (1984), pp. 1,045–1,051.
52) M. Kikukawa, M. Jono, and Y. Kondo, “Study on Test Method of Fatigue Crack Growth Threshold,” *J Soc Mater Sci Japan*, 30–330 (1981), pp. 276–282.
53) P. K. Liaw, T. R. Lea, and W. A. Logsdon, “Near-threshold fatigue crack growth behavior in metals,” Acta Metallurgica, 31–10 (1983), pp. 1,581–1,587.
54) R. O. Ritchie, “Mechanisms of fatigue-crack propagation in ductile and brittle solids,” *International Journal of Fracture*, 100–1 (1999), pp. 55–83.

Daisuke Watanuki

Masako Tsutsumi

Hideyuki Hidaka

Kentaro Wada

Hisao Matsunaga

Enhancement of Weldline Strength by Applying a Reservoir to the Plastic Cage of a Rolling Bearing

Yoshikazu Kuramoto, Takayuki Hiramoto, and Nariaki Aihara
Core Technology R&D Center, Technology R&D Office 2
Keisuke Yokoyama
Core Technology R&D Center

Abstract

In order to enhance the weldline strength of the plastic cage for rolling bearings, the specification of the reservoir embedded in the cage injection mold was investigated by using resin flow analysis. In this study, the plastic flow distance on the weldline has been found as the evaluation index for the simulation. With the ring-shaped test pieces, the threshold of the evaluation index was determined by comparing the calculated plastic flow distance on the weldline with the measured weldline strength. Also revealed was that the weldline strength values of the crown-type and the machined-type plastic cages are significantly enhanced by applying the threshold to resin flow analysis.

1. Introduction

Various machine parts incorporate rolling bearings for the purpose of high functionality and to save energy. Rolling bearing cages are conventionally made of metal, but cage resinification has become more common in recent years because it provides advantages such as light weight, low noise, ease of molding into various shapes, and ease of maintaining grease cleanliness within the bearing because there is no generating metallic abrasion powder. In general, resin materials are inferior in strength and elastic modulus compared to metal materials, so plastic cages are often made of resins reinforced with glass fibers or carbon fibers. However, at the joint portion (weldline) of the resin that forms when the annular plastic cage is manufactured by injection molding, the fibers are not oriented in a circumferential direction and there is no reinforcing effect. Such manufacturing weaknesses pose a problem in the resinification of such cages. Our theory is that strengthening the weldline of plastic cages will lead to the expansion of their applicability.

As a means to strengthen the weldline, one option is a reservoir placed in an injection mold. Generating a circumferential flow toward the reservoir in the resin around the weldline orients the fibers of the weldline in a circumferential direction, thus strengthening the weldline. Researchers have conducted studies in relation to the influence of the position of the reservoir on the weldline strength of the dumbbell test piece[1)] and making the weldline stronger by compressing the resin with the core pins provided in the reservoir[2)]. These studies have verified the effect of strengthening the weldline experimentally; however, until now they had not conducted a study to simulate and verify this phenomenon and its effects.

In this study, we applied resin flow analysis to confirm whether we can simulate and predict the effect of strengthening the weldline with a reservoir. First, using a ring-shaped test piece, we verified the effect of the capacity and position of a reservoir on weldline strength in experiments. Next, we carried out resin flow analysis on the ring-shaped test piece to confirm whether the experimental results can be simulated, and we defined an index that showed the influence of the capacity and position of a reservoir on the weldline strength in analysis. Then we confirmed whether this index could be applied to crown-type and machined-type cages to determine the appropriate capacity and position of the reservoir. Our report on the results of these efforts follows.

2. Verification of Weldline Strengthening Effect by Applying a Reservoir

2.1 Experimental method

Figure 1 shows the ring-shaped test piece used in the experiment. The size is ϕ66 mm in outer diameter, ϕ58 mm in inner diameter, and 5 mm in width, and the material is polyamide 66 containing 25 wt% glass fiber. The capacity of the reservoir is set to four types, 1.3%, 2.1%, 4.3%, and 6.5% of the capacity of the ring-shaped test piece. The position of the reservoir is set to four types 0°, 30°, 60°, and 135°, from the weldline. We adjusted the size of the resin flow path from the main body of the ring-shaped test piece to the reservoir so that the resin would flow into the reservoir after the weldline was formed in the annular part.

We measured the strength using the precision universal testing machine AUTOGRAPH AG-X (manufactured by Shimadzu Corporation) by applying a load to the weldline located in the center of the test piece cut into a semicircle, as shown in Figure 2. The load at the time of breakage of the test piece was considered to be the strength.

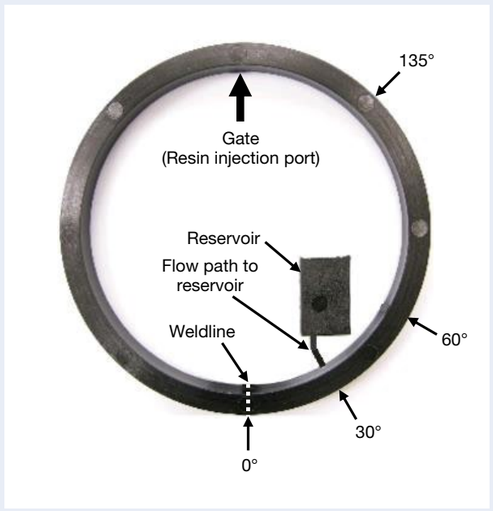

Fig. 1 Ring-shaped test piece

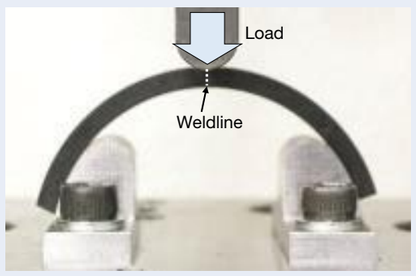

Fig. 2 Apparatus for test piece strength measurement

2.2 Experimental results and discussion

Figure 3 shows the results of confirming the resin filling behavior with a short-shot sample in which the mold was half filled with resin. We confirmed that the resin flowed into the reservoir after the weldline was formed in the annular part.

Figure 4 shows the results of observing the fiber orientation around the weldline for three types of test pieces with different capacities and positions of the reservoir. We observed the fiber orientation using the X-ray CT device TOSCANER-32251 μhd (manufactured by Toshiba IT & Control Systems Corporation). In the test piece (c) where we placed a reservoir with a capacity of 6.5% at the 30° position, observation results showed that the fibers around the weldline were oriented in a circumferential direction. On the other hand, in test piece (a) without a reservoir and test piece (b), installed a reservoir at the 0° position, we confirmed that fibers not oriented in a circumferential direction remained in the weldline.

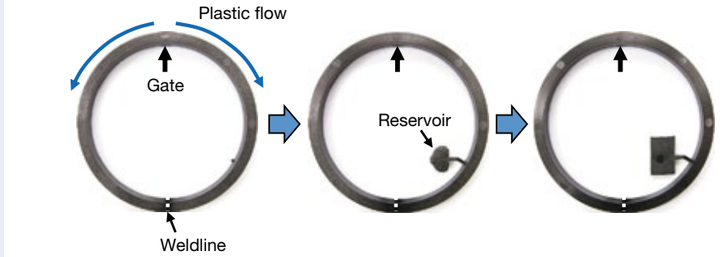

Fig. 3 Filling behavior of melt plastic in the test piece

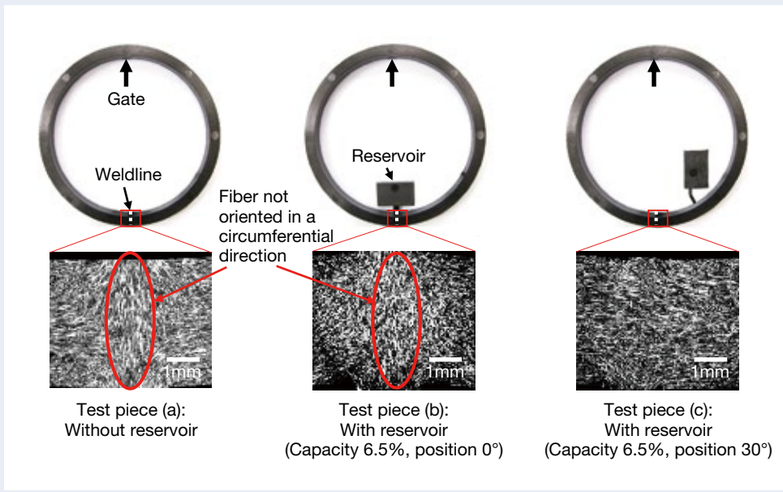

Fig. 4 Fiber orientation around the weldline in the test piece

Figure 5 shows the results of measuring weldline strength when we changed the combination of the capacity and position of the reservoir. When we applied the reservoir, the fibers around the weldline were oriented in a circumferential direction, strengthening the weldline. Furthermore, we confirmed the following two tendencies regarding the effect of strengthening the weldline.

1) The larger the capacity of the reservoir, the higher the weldline strength. We believe this is because the flow time of the resin around the weldline becomes longer when we increase the capacity of the reservoir, which makes it easier to orient the weldline fibers in a circumferential direction.
2) The closer the reservoir is to the weldline, the higher the weldline strength. We believe this is because the flow rate of the resin around the weldline and the flow velocity increase by shortening the path from the gate (resin injection port) to the reservoir via the weldline, which makes it easier to orient the weldline fibers in a circumferential direction.

However, when the position of the reservoir was 0°, i.e., when it coincided with the weldline, we saw almost no strengthening of the weldline. In this case, even when the resin around the weldline flowed into the reservoir, the flow did not orient the fibers in a circumferential direction. We therefore believe it did not strengthen the weldline.

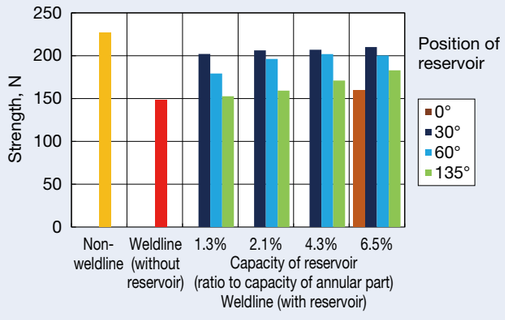

Fig. 5 Test piece strength

3. Confirmation of Weldline Strengthening Effect in Analysis

The above results demonstrated that we could strengthen the weldline by generating resin flow in a circumferential direction around it, thus orienting the fibers around the weldline in a circumferential direction. To simulate the flow behavior of this resin by resin flow analysis, we created an analysis model of the ring-shaped test piece and calculated the resin filling behavior using the resin flow analysis software 3D TIMON (manufactured by Toray Engineering D Solutions Co., Ltd.) To demonstrate in the analysis the results of the above experiment, i.e., that strengthening the weldline depends on the flow time and flow velocity of the resin around the weldline, we introduced an evaluation index called "plastic flow distance," defined by the product of flow time and flow velocity of resin. The plastic flow distance is the amount corresponding to the moving distance obtained by dividing the volume of resin that has passed through a specific cross section of the flow path by that cross-sectional area (Figure 6).

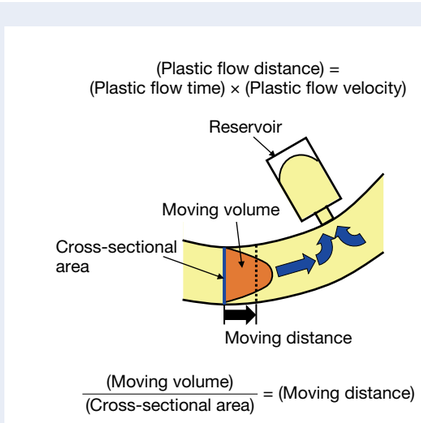

Fig. 6 Definition of plastic flow distance

Figure 7 shows a comparison of the experimental results and the analysis results regarding the resin filling process. As with the experimental results, we found that the resin flows into the reservoir after the weldline is formed in the annular part.

Regarding the three types of test pieces with different capacities and positions of the reservoir, Figure 8 shows the results of analyzing the fiber orientation around the weldline. As with the observation results in the experiment (Figure 4), in test piece (c), in which we installed a reservoir with a capacity of 6.5% at the 30° position, the analysis results showed the weldline fibers to be oriented in a circumferential direction. On the other hand, in test piece (a), without the reservoir, and test piece (b), installed reservoir at the 0° position, the analysis results showed that fibers not oriented in a circumferential direction remained in the weldline.

Fig. 7 Comparison of filling behavior between experiment and analysis

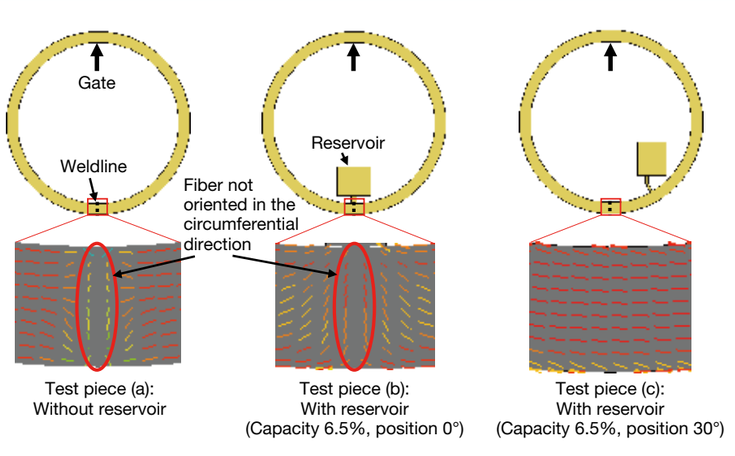

Fig. 8 Simulated fiber orientation around the weldline in the test piece

Furthermore, with the capacity of the reservoir set to four types (1.3%, 2.1%, 4.3%, and 6.5% of the capacity of the ring-shaped test piece), and the positions set to three types (30°, 60°, and 135° from the weldline), we calculated the plastic flow distance for all combinations. Figure 9 shows the results. Our calculation results corresponded with the experimental results and discussions, i.e., the larger the capacity of the reservoir and the closer the position to the weldline, the larger the plastic flow distance.

With this method, we achieved a result where the analysis corresponded well with the experiment. We also further verified the relationship between the plastic flow distance of the weldline and weldline strength. Figure 10 shows the relationship between the plastic flow distance obtained in the analysis and the weldline strength obtained in the experiment. The result was that the weldline strength increased with the increase of the plastic flow distance and became saturated when the plastic flow distance reached 2.7 mm or more. We therefore set the threshold for determining the effectiveness of the reservoir to strengthen the weldline in the resin flow analysis to 2.7 mm of plastic flow distance, and we tested whether we could determine the appropriate capacity and position of the reservoir with an actual cage.

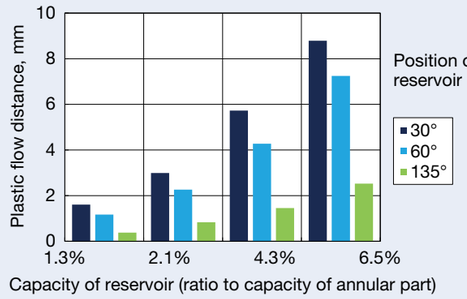

Fig. 9 Calculated plastic flow distance on the weldline of the test piece

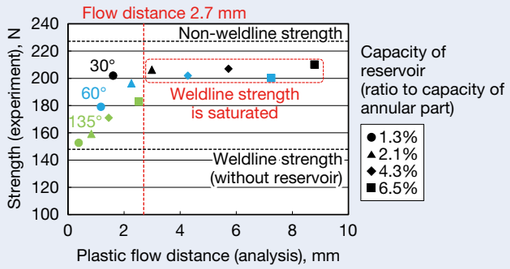

Fig. 10 Comparison of measured weldline strength and calculated flow distance on the weldline

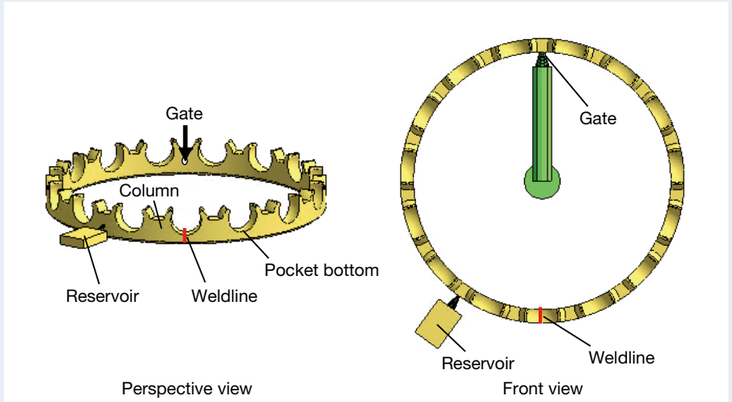

Fig. 11 Crown-type plastic cage

4. Applying Analysis to Crown-Type Cages

We applied the findings obtained from the verification of the ring-shaped test piece to crown-type plastic cages for rolling bearings, as shown in Figure 11, and measured the effect. We performed resin flow analysis using a model in which we installed a reservoir in the cage with an outer diameter of ϕ 59.3 mm, inner diameter of ϕ 53.7 mm, width of 7.25 mm, 15 pockets. The material of the cage is polyamide 46 containing 25 wt% glass fiber. We calculated the plastic flow distance of the weldline. In most crown-type cages, the gate is approximately in the center of the column. For this reason, in a cage with an odd number of pockets, the weldline forms at the bottom of the pocket. We installed the reservoir on the column at the 36° position from the weldline. The reservoir capacity was set to 2% or 5% of the cage capacity, and the flow path to the reservoir was provided almost in the center of the column as in the above-mentioned gate.

Figure 12 shows the calculation results. When the capacity of the reservoir was 2%, the plastic flow distance

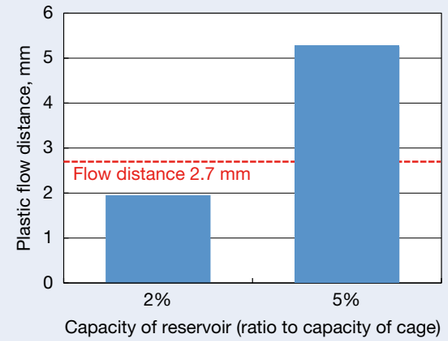

Fig. 12 Calculated plastic flow distance on the weldline of the crown-type plastic cage

did not exceed 2.7 mm, but when the capacity was 5%, the plastic flow distance exceeded 2.7 mm. We therefore prototyped a cage with a mold provided with a reservoir with a capacity of 5% and measured the weldline strength. When measuring the strength, we applied a tensile load using the precision universal testing machine AUTOGRAPH AG-X (manufactured by Shimadzu Corporation), as shown in Figure 13, and set the load at the time of breakage of the cage as the strength. Figure 14 shows the results. By applying a reservoir, we strengthened the weldline of the crown-type cage to almost the same level as sections other than the weldline.

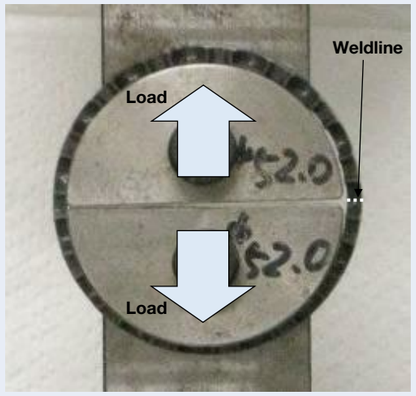

Fig. 13 Apparatus for strength measurement of the crown-type plastic cage

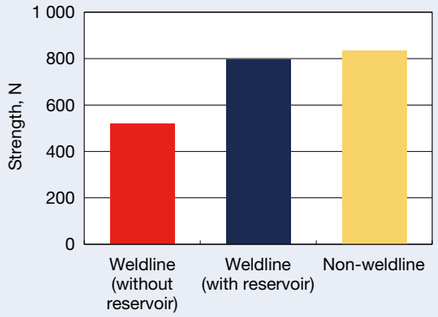

Fig. 14 Strength of the crown-type plastic cage

5. Applying Analysis to Machined-Type Cages

We applied the findings obtained from the verification of the ring-shaped test piece to the machined-type cages shown in Figure 15 and tested the effect. We performed resin flow analysis using an analysis model in which we installed a reservoir in the cage with an outer diameter of ϕ 93.5 mm, inner diameter of ϕ 86.9 mm, width of 13.5 mm, 25 pockets. The material of the cage is polyphenylene sulfide containing 30 wt% carbon fiber. We calculated the plastic flow distance of the weldline. We installed the gates at five locations at equal intervals on the columns, referring to the cages used for the current bearings. With this gate arrangement, the multiple weldlines shown in Figure 15 were formed. Of these weldlines, our aim was to strengthen them at the bottom of the pockets, which would be damaged first in a bearing rotation test. We installed the reservoirs on the column at the 7.2° positions from the weldlines. The reservoir capacity was set to 2% or 4% of the cage capacity. Furthermore, we provided the flow path to the reservoirs at positions shifted in the axial direction from the center of the column due to restriction in machining mold.

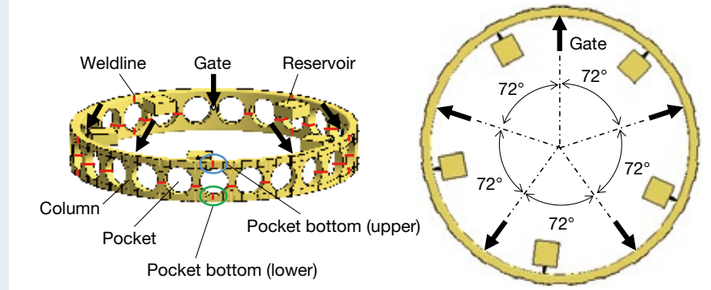

Fig. 15 Machined-type plastic cage

Figure 16 shows the calculation results. The plastic flow distance of the weldline at the bottom of the pocket (upper), which was closer to the flow path to the reservoir, was larger than that of the weldline at the bottom of the pocket (lower), which was away from the flow path to the reservoir. We believe this is because the resin flow velocity of the weldline at the bottom of the pocket (upper), which was closer to the flow path, was higher than that of the weldline at the bottom of the pocket (lower). When the capacity of the reservoir was 2%, the plastic flow distance of the weldline at the bottom of the pocket (upper) did not exceed 2.7 mm, but when the capacity was 4%, the plastic flow distance of both weldlines at the bottom of the pocket (upper and lower) exceeded 2.7 mm. We therefore prototyped a cage with a mold provided with reservoirs with a capacity of 4% and measured the weldline strength. When measuring the strength, we cut out the pocket where the weldline is formed from the cage, applied a tensile load to the cage using the precision universal testing machine AUTOGRAPH AG-X (manufactured by Shimadzu Corporation), as shown in Figure 17, and set the load at the time of breakage of the cage as the strength. Figure 18 shows the results. We found that the weldline strength decreased to 47% of the non-weldline portions without reservoirs, but increased to 85% of the non-weldline portions when equipped with appropriate reservoirs. In summary, we proved that we can use resin flow analysis to determine the proper capacity and positions of the reservoirs to strengthen the weldline of machined-type cages.

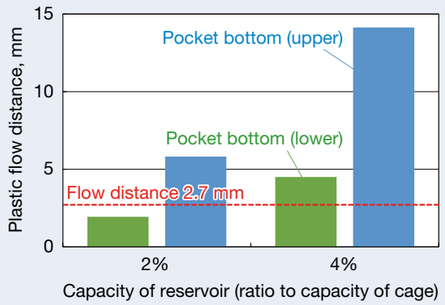

Fig. 16 Calculated plastic flow distance on the weldline of the machined-type plastic cage

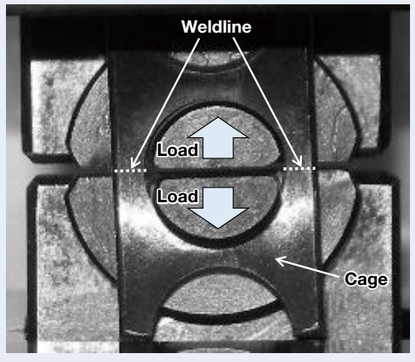

Fig. 17 Apparatus for strength measurement of the machined-type plastic cage

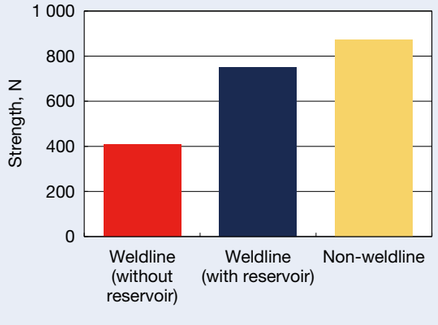

Fig. 18 Strength of the machined-type plastic cage

6. Conclusion

We achieved the following results in this study.

1) By making a prototype of the ring-shaped test piece and measuring the strength, we showed that we can strengthen the weldline by applying a reservoir and that the effect of strengthening the weldline changes depending on the capacity and position of the reservoir.
2) We showed that the effect of strengthening the weldline by applying a reservoir can be calculated in resin flow analysis. As an evaluation index of strength in the analysis, we defined the plastic flow distance by calculating the product of resin flow time and resin flow velocity.
3) Using resin flow analysis, we could successfully determine the proper capacity and positions of the reservoirs to strengthen the weldline of both crown-type and machined-type cages.

In the future, by applying this technology to expand the scope of application of plastic cages, we would like to promote weight reduction of rolling bearings and thereby contribute to reductions of CO_2 and fuel consumption.

This article is a compilation of papers previously published in the proceedings of the 29th to 32nd Annual Meetings of the Japan Society of Polymer Processing, edited and modified into a single journal article[3, 4, 5, 6].

References

1) T. Takayama, H. Ito, N. Sato, A. Suino, and K. Kitamura, "Effects of Resin Reservoir on the Weld Strength of Carbon Fiber Reinforced Polymer Composites," Preprints of Seikei-Kakou Annual Meeting 2015, (2015), pp. 325–326.
2) T. Hishida, A. Motegi, and Y. Murata, "Improvement of Weld line Generated in Injection Molded Products by In-Mold Core Pin Drive Method IV," Preprints of Seikei-Kakou Annual Meeting 2017, (2017), pp. 303–304.
3) Y. Kuramoto, T. Hiramoto, N. Aihara, and K. Yokoyama, "Enhancement of Weldline Strength by Applying Reservoir to Plastic Cage of Rolling Bearing," Preprints of Seikei-Kakou Annual Meeting 2018, (2018), pp. 269–270.
4) Y. Kuramoto, T. Hiramoto, N. Aihara, and K. Yokoyama, "Enhancement of Weldline Strength by Applying Reservoir to Plastic Cage of Rolling Bearing (Part 2): Reservoir Specification Determined by Resin Flow Analysis," Preprints of Seikei-Kakou Annual Meeting 2019, (2019), pp. 229–230.
5) Y. Kuramoto, T. Hiramoto, N. Aihara, and K. Yokoyama, "Enhancement of Weldline Strength by Applying Reservoir to Plastic Cage of Rolling Bearing (Part 3): Deploying to the Cage Used for Machine Tools," Preprints of Seikei-Kakou Annual Meeting 2020, (2020), pp. 235–236.
6) Y. Kuramoto, T. Hiramoto, N. Aihara, and K. Yokoyama, "Enhancement of Weldline Strength by Applying Reservoir to Plastic Cage of Rolling Bearing (Part 4): Deploying to the Cage Used for Machine Tools (Part 2)," Preprints of Seikei-Kakou Annual Meeting 2021, (2021), pp. 157–158.

Yoshikazu Kuramoto

Takayuki Hiramoto

Nariaki Aihara

Keisuke Yokoyama

Keisuke Yokoyama

SuperLimbs for Sit-to-Stand Support and Fall Prevention

Seiichi Teshigawara
New Field Products Development Center, Technology Development Department 1
John Bell, Emily Kamiensky, and Haruhiko Harry Asada
Massachusetts Institute of Technology, Mechanical Engineering

Abstract

Here we introduce a new eldercare robot design concept that can seamlessly assist older adults with balancing, walking, and moving from a sitting to a standing position. The system consists of a pair of supernumerary limbs (SuperLimbs) that attach to the user. As an initial challenge, we performed an analysis to confirm the requirements of actuators at each joint. To provide sit-stand support, we found that SuperLimbs must generate significant force to gently elevate the user's body. Additionally, SuperLimbs must react to the user's movement rapidly for balancing and fall prevention. To meet these bimodal requirements, we propose the use of dual-motor actuators that incorporate two brushless DC motors with diverse gear ratios into a single joint.

1. Introduction

In Japan, the percentage of people aged 65 and over is 28.8%[1] as of October 1, 2020, making the nation what demographers call a super-aging society. In many cases, those aged 65 or over have no major health problems; however, if they fall or have some other accident, they may end up bedridden or even in a wheelchair since injuries are often more serious at their age than they are for younger people. In the U.S., the number of people aged 65 and over has increased rapidly since 2020, and the incidence of reported falls has also been increasing. The main reason for people aged 65 and over being taken away in ambulances is falling, and about three million people aged 65 and over are treated in emergency rooms every year[2] in the U.S. Since the insurance paid by Medicare, the public health insurance system in the U.S., is only about $29 billion[3] (excluding fatal accidents), this is an urgent social and economic problem.

A survey of the locations of falls showed that the rate of occurrence in residences is higher than that outdoors and in public facilities (including hospitals), at about 48%[4] in Japan and about 47%[5] in the U.S. The study also found this is common in other countries such as Canada and the U.K. The risk of falling is present in various situations, but it is most likely to occur when standing or sitting on a bedside or sofa and when stumbling while walking. Devices that help to support people in such situations are therefore necessary.

Assist tools often used indoors include canes and walkers, which are inexpensive and widely available. On the other hand, only their proper use ensures the safety of such passive devices, and there have been reports of cases in which a fall was caused due to their improper use or faulty operation[6].

Focusing on these problems, companies have developed active devices for people aged 65 and older that support walking, standing, and sitting. For example, AIST's fall-prevention robot looks like a walking vehicle but is actually not; it supports the user under the armpits to prevent falls[7]. Another example is Fuji Corporation's Hug[8], which supports standing and sitting and helps to realize optimum posture and trajectory during sit-to-stand motions using several actuators. However, after completing the sit-to-stand motion, the user entrusts himself or herself to the robot, which does not perform voluntary walking motions, so a caregiver must help the user to move. In other words, these devices are independent for each motion, such as assisting walking or standing only, and using Hug requires the assistance of a caregiver.

On the other hand, those aged 65 and older who receive care tend to want to move independently of their own will to any place at any time, and most do not want to rely on a caregiver. Therefore, in this report, focused on those aged 65 and older, we propose leg-shaped robotic limbs (SuperLimbs) that people can use by themselves, as SuperLimbs seamlessly assists in standing, sitting, walking, and preventing falls while walking.

2. Basic Concept

Below we present the definition of the target market and basic concept and also clarify our objectives.

The target market should satisfy the following conditions.

- People aged 65 or over (rough guideline)
- People without cognitive impairment
- People who require support (e.g., canes, handrails) when standing or sitting
- People who require support (e.g., walkers, canes) when walking

The target market should be people aged 65 or over who are generally healthy but need some support when

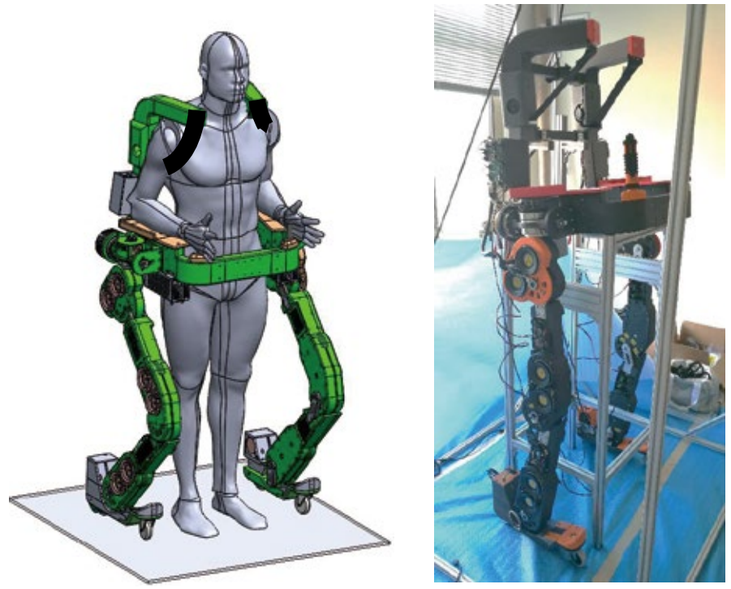

Fig. 1 SuperLimbs robot CAD model (left) and prototype (right)

standing, sitting, or walking. In addition, we believe that there are two factors in terms of needing support: one is the physical aspect due to muscle weakness, and the other is the psychological aspect such as worrying about falling. In nursing facilities, caregivers provide a wheelchair when they think that the risk of falling while walking is high, but once the user uses a wheelchair, motivation for walking tends to decrease due to the comfort and security of the device. As a result, their muscles weaken, and eventually the individual is unable to walk steadily and safely, or even at all.

Considering the above, we developed a support device that reduces the fear of walking, raises people's motivation to walk, and includes rehabilitation elements such as function maintenance and recovery.

3. Design Concept and Outline of Leg-Shaped Robots

Assuming barrier-free indoor use, we developed SuperLimbs to seamlessly aid in standing, sitting, walking, and fall prevention. Below we outline the basic concept on which the robot limb was based and designed as well as how it behaves in each movement. We have established the functions below as required for the SuperLimbs.

① Assist people when standing or sitting
② Behave like a walker while people are walking
③ Detect falls and actively prevent them
④ Seamlessly achieve ①–③
⑤ Limit interference with the user's motion
⑥ Make easy to attach and detach
⑦ Feature two-way voice communication
⑧ Include obstacle recognition (environmental recognition)
⑨ Make able to travel autonomously except when being used
⑩ Monitor the user's physical state

3.1 Assisting in walking and preventing falls

From the viewpoint of biomechanics, the positional relationship between the human body's center of gravity (COG, with COG being synonymous with COM in this report) and the support base (BOS) is of critical importance[9]. When a human stands on both feet, the BOS refers to the sides of the feet in contact with the ground and the surfaces generated by connecting the heels of the feet and by connecting the toes of the feet into a straight line (Figure 2, left). With both feet spread, the BOS expands, thus improving stability, and with the heels in contact with each other, the BOS narrows, thus reducing stability. In addition, the center of gravity line passing through the inside of the BOS provides statical stability, which prevents falling. On the other hand, the center of gravity line falling outside the BOS due to lost balance will reduce stability, which may cause falling without acts such as quickly moving the positions of the feet (Figure 2, center). Use of canes and walkers will improve stability because the BOS expands while such tools are in contact with the ground, and thus the stable area increases. When the position of the cane moves, however, the BOS momentarily narrows while the cane is in the air, so the user could fall by losing balance at that time. Compared to a cane, a walker seems to be safer because of its enclosed shape, but there is a risk of tripping over the walker and of falling due to improper use.

As shown in Figure 3, each leg of SuperLimbs has five degrees of freedom, and the limb can change the leg position like humans do. For this reason, when the user loses balance, the robot's legs move quickly to support the body and thereby prevent falling (Figure 2, right). The soles of SuperLimbs are equipped with casters in the front and active wheels in the rear, which function like a walker with tires during normal walking, and the user can also walk with the robot as a support. Moreover, the limb can assist the force to go forward using the active wheel.

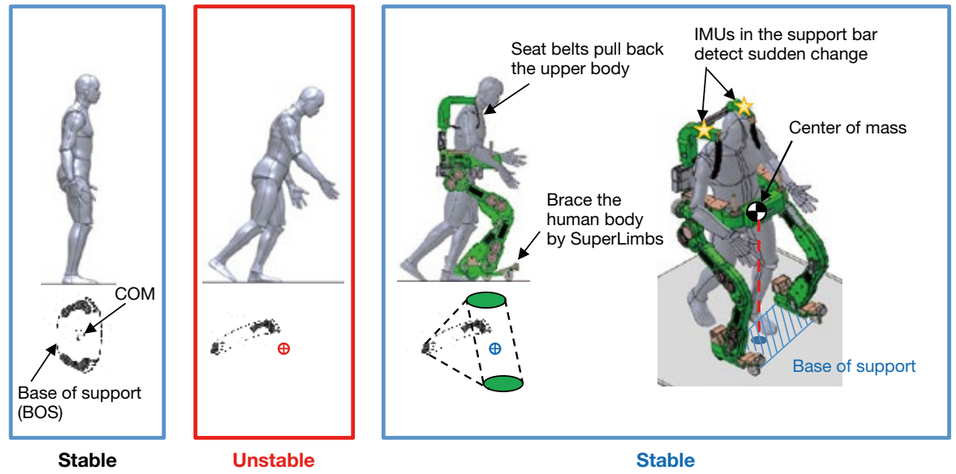

Fig. 2 Fall prevention using SuperLimbs

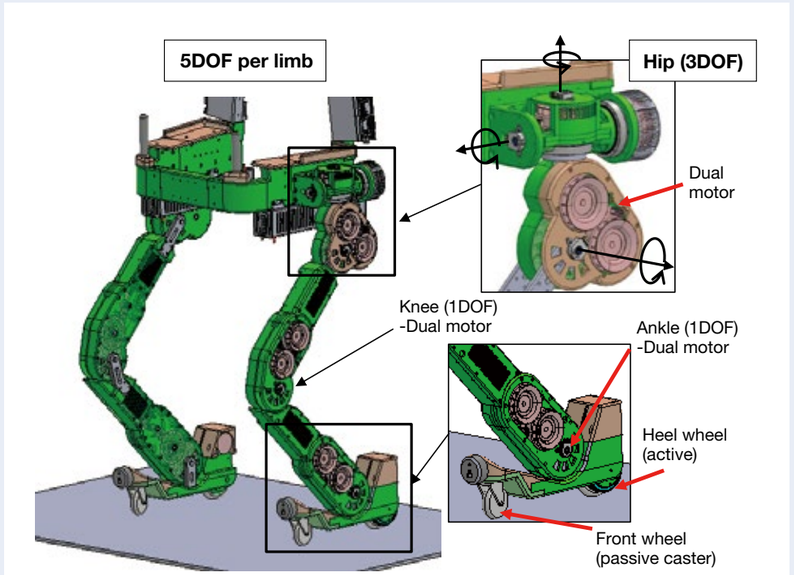

Fig. 3 Degrees of freedom in each SuperLimb

3.2 Assisting in standing and sitting

The relationship between the COG and BOS is also very important for assisting in standing and sitting. Normally, a human's center of gravity is around the navel, and when sitting, the BOS includes the part where the buttocks are in contact with the chair. When performing sit-to-stand motions, unless the COG is on the BOS generated from two feet at the moment when the buttocks are separated from the chair, the user will not be able to stand up and will be forced to sit again. At this point, there are two ways to stand up from the sitting posture. One is to use inertial force (momentum) to move the COG to the BOS of both feet at the moment when the buttocks are separated from the chair. Young people are highly adept at this method and thus can stand up quickly. The other method is to bring the COG close to the BOS of both feet before the buttocks leave the chair, which is best for older and injured people. The sit-to-stand motion is a combination of these two methods. The robot limbs we developed are supposed to perform the latter smoothly in order to provide support.

As shown in Figure 4, as a preliminary movement before standing up, the user is guided to take a forward-leaning posture with his or her back pressed. This movement to take a forward-leaning posture enables support to lift the buttocks after moving the position of the COG to the vicinity of the heel as much as possible so that the user can stand up smoothly. By providing such support and gradually reducing the support load of the robot limbs, the limbs have a secondary effect: rehabilitation.

3.3 Other functions

One of the easiest user interfaces for those aged 65 and older is voice. With recent developments in AI technology, it is now possible to accurately recognize human voices. Voice input, such as waking up in the morning and calling SuperLimbs to the bedside, instructing the robot attachment or detachment, starting support for standing, and giving instructions on where the user wants to go when walking, is highly effective because it can be done without using hands. In addition, if the robot is able to convey information to the user by voice, it can give alerts when he or she is approaching a step, mat, or some other obstacle on the floor surface that has been mapped in advance. Since older people may not be able to raise their legs as they intended, even if they are aware of steps, and may stumble or fall in unexpected places, we believe that we can reduce the risk of falls by calling their attention with alerts such as, "There is a step in front of you, so please raise your legs and walk carefully." In the future, we hope SuperLimbs will be able to refer to a large amount of elderly fall patterns and caregiver voice data in the cloud, predict danger in advance, and speak using the most understandable and natural vocabulary.

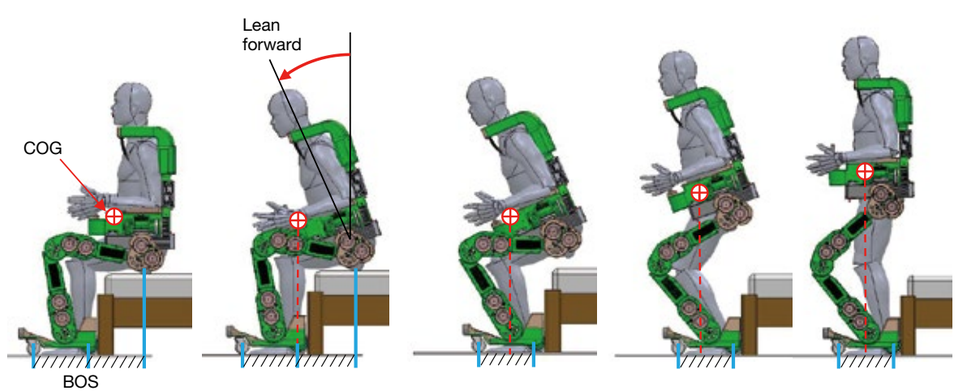

Fig. 4 Sit-to-stand support

When attaching and detaching SuperLimbs, a user who is sitting, as shown in Figure 5, is covered from above by an attachment. At this point, the robot identifies the posture of the user using a 3D camera and then attaches itself to the person while notifying him or her vocally of its action..

4. Actuator Requirements and Dual Motors

Based on the above concept, a compact and lightweight actuator was indispensable in developing SuperLimbs. To calculate the torque required for each joint of the robot during the sit-to-stand motion, we modeled a human body based on anthropometry and performed static analysis simulation. Below are the results.

4.1 Actuator requirements

We modeled the human body to calculate the load torque applied to the robot joints during the sit-to-stand motion. Anthropometry is a study related to the method of measuring the length ratio of each portion to the human height H (e.g., shin, thigh, body, head), the weight ratio of each portion to the weight W, and the COG position, and it is applied to the study of physical differences and ergonomics. In this case, we created a two-dimensional model of the human body based on the parameters shown by Dempster[10] (Figure 6). In this model, given the height H and weight W, we can also calculate the length, weight, and COG position for each portion. Furthermore, the angle data at the time of rising operation was generated with reference to the literature[11], and this was used as the input for the simulation (Figure 7). This data shows the motion capture of the sit-to-stand motion and time changes in the angles of the ankle joint, knee joint, and hip joint, which makes it possible to trace the changes in the position and posture as well as the COG position for each joint during the sit-to-stand motion in this simulation.

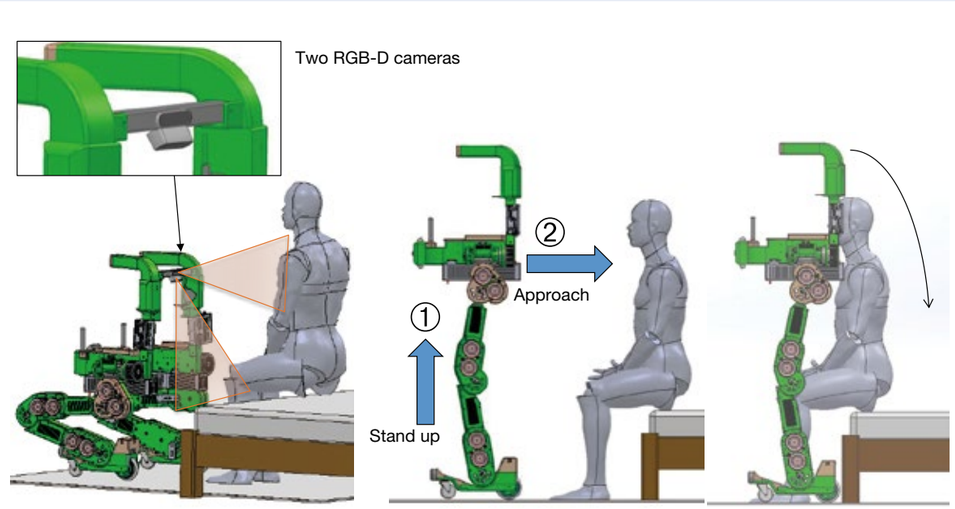

Fig. 5 Attachment and detachment

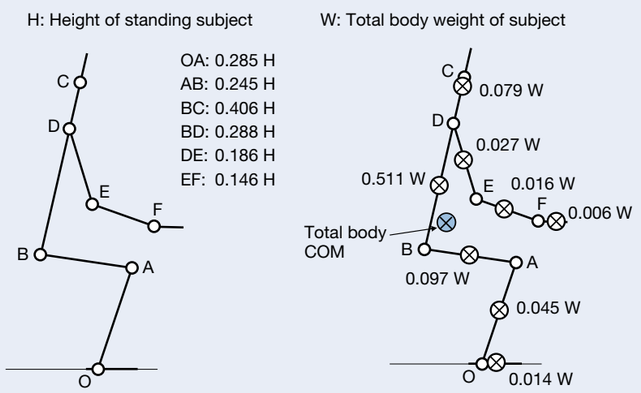

Fig. 6 2DOF model of a human body

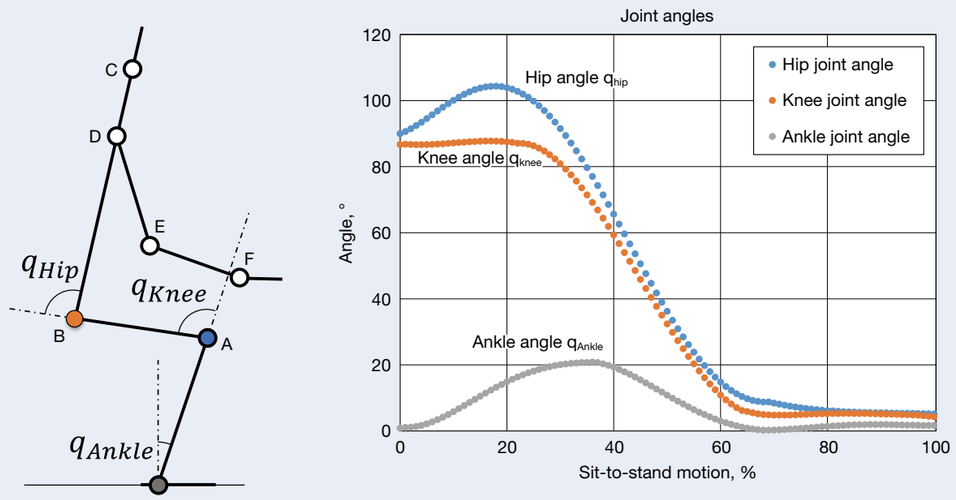

Fig. 7 Angle data for each joint

However, we based the position and posture of the arm on the shoulder joint, so it faces vertically downward from beginning to end. Figure 8 shows the results of simulating the sit-to-stand motion with a height of 175 cm and weight of 80 kg. The red line shows the calculated time changes in COM.

Next, we modeled SuperLimbs, as shown in Figure 9. For the sake of simplicity, we made the calculations assuming that the COG position (W_COM) calculated by the above human body model was supported by the position connected to the Rb joint of SuperLimbs in a straight line. We performed the simulation according to the following conditions.

i) Ro ankle joint of SuperLimbs matches a human ankle joint
ii) Both ankle joints of a human and SuperLimbs are fixed without moving back and forth
iii) Positions of the hip joints of a human and SuperLimbs are the same
iv) Weight of the structure above Rb of SuperLimbs is the concentrated load of point Rb

Figure 10 shows the results of this simulation. From left to right, the data are for the ankle joint, knee joint, and hip joint. The horizontal axis is the COG position of the human body (mm), and the vertical axis is the torque (Nm) calculated from the balance of forces. This simulation

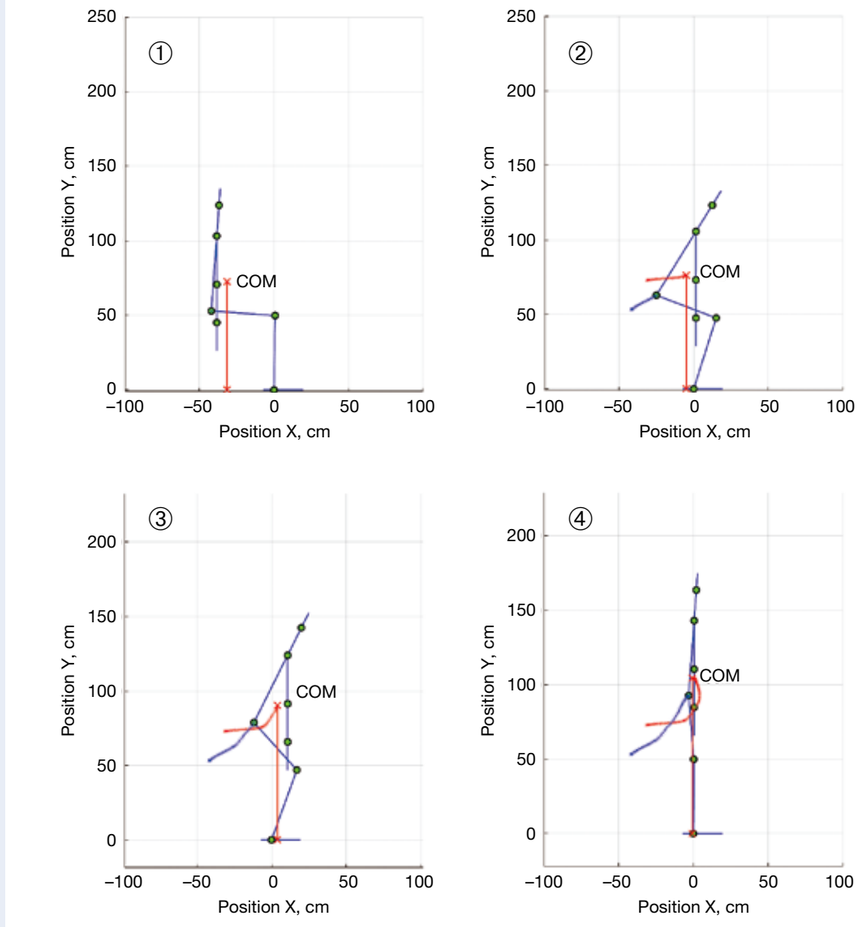

Fig. 8 Simulation result for sit-to-stand motion

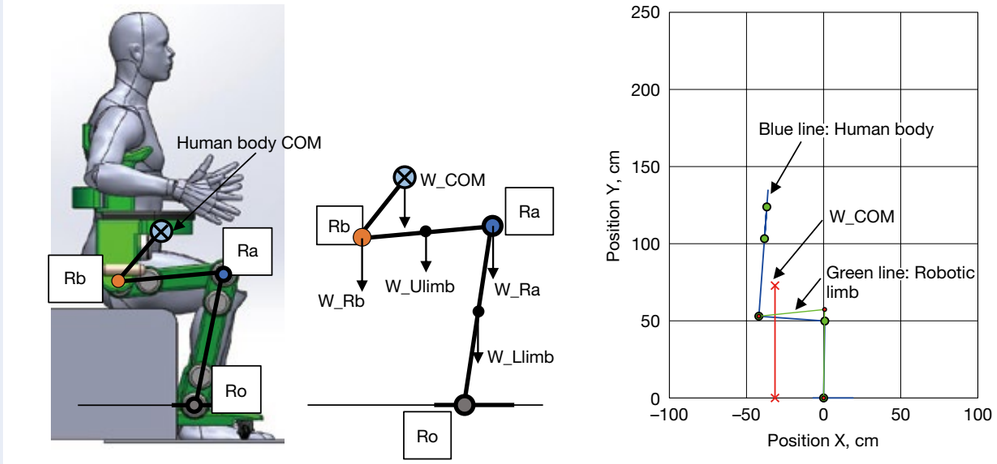

Fig. 9 Simulation model with SuperLimbs

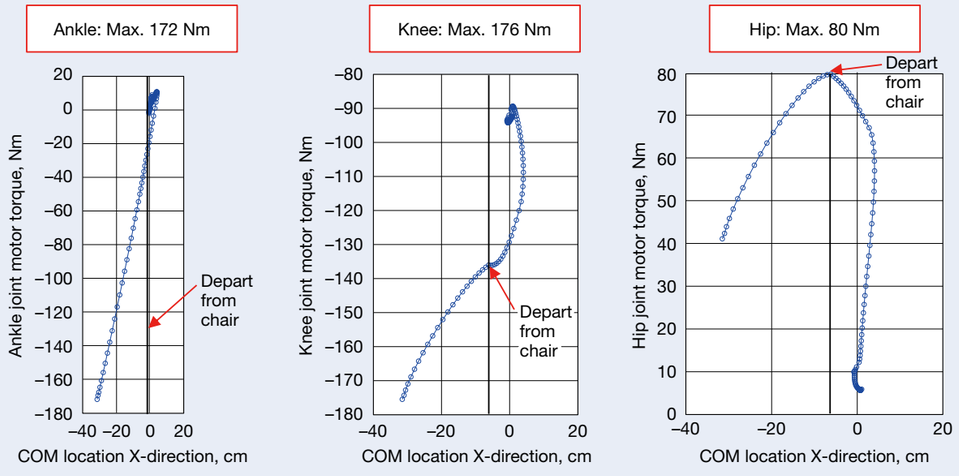

Fig. 10 Torque requirements for each joint during sit-to-stand motion

result found that the knee joint requires the largest torque, with the maximum being 176 Nm. We also found that a maximum rotation speed of 10 rpm is required when 4 seconds is assumed, with reference to Tomomitsu Kotake's paper[12], showing that the sit-to-stand motion of the elderly takes 3 to 4 s. That is, assuming that a leg robot supports all the human weight of 80 kg, a low-speed, high-torque actuator with a maximum of 176 Nm and 10 rpm is required.

On the other hand, when considering fall prevention, the characteristics required for an actuator are considered to be high-speed, low-torque operating points. Although this requires kinetic analysis, we recommend referring to the paper by Bell et al[13].

4.2 Dual-motor actuator

Based the above, the actuator has the following two operating points.

① Low speed and high torque (sit-to-stand motion assistance)
② High speed and low torque (quick movement of legs to prevent falls)

Meeting these two operating points simultaneously requires a very large motor, so in order to employ the two opposite specifications at the same time, we used a dual-motor actuator. Although many research groups have already developed dual-motor actuators[14, 15, 16, 17, 18] most operate with mechanical switching, which tends to complicate the switching mechanism. In contrast, our research group adopted a method of electrical switching[19] in three places, the hip joint, knee joint, and ankle joint, and we made prototypes according to each form (Photo 1).

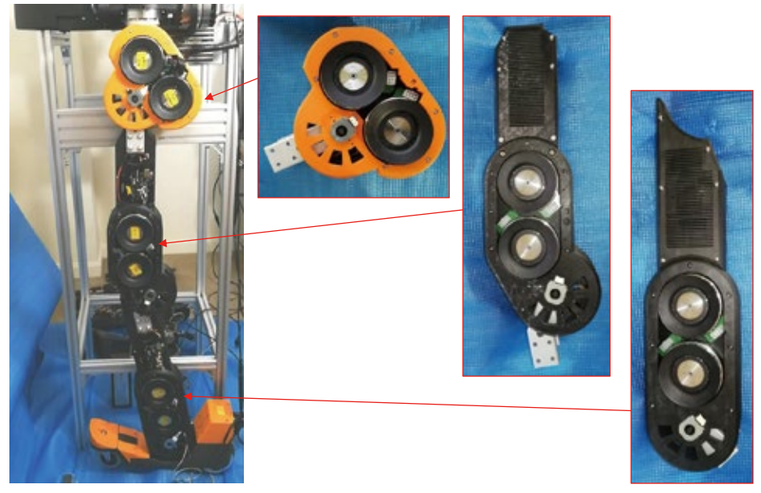

Photo 1 Prototypes of the dual-motor actuator

5. Conclusion

We have discussed the basic concept and design of the robot in the first half of this report, and the idea behind the design of the leg-shaped robot in the second. In the process, we explained the torque required for the robot actuator using a simple simulation. To meet the gap between the actuator requirements required for the sit-to-stand motion and the actuator requirements required for rearranging human legs, we selected a dual motor, and we presented a prototype of a leg-shaped robot equipped with that motor.

Although we have only just started development of this project, we believe this technology is essential not only in Japan but all over the world. To bring our robot to fruition, we must have an actuator such as a small, lightweight dual motor that can operate at both low speed and high torque and at high speed and low torque. In addition, the technology must include various development elements such as system control technology, environment recognition technology, autonomous driving technology, human monitoring technology, and AI technology, and we can maximize the robot's functionality by integrating all of these. We hope that more people will understand the technology by reading this report and contact us with any inquiries.

References

1) Cabinet Office, Annual Report on the Ageing Society 2021: https://www8.cao.go.jp/kourei/whitepaper/w-2021/zenbun/03pdf_index.html
2) Web-based injury statistics query and reporting system. Accessed Oct. 17, 2020 (online). Available at: https://www.cdc.gov/injury/wisqars/
3) C. Florence, G. Bergen, A. Atherly, E. Burns, J. Stevens, and C. Drake, "Medical costs of fatal and nonfatal falls in older adults," *Journal of the American Geriatrics Society*, vol. 66, no. 4, pp. 693–698, 2018.
4) Consumer Affairs Agency, news release on October 8, 2020: https://www.caa.go.jp/policies/policy/consumer_safety/caution/caution_040/assets/consumer_safety_cms204_201008_01.pdf
5) Lava R. Timsina, Joanna L. Willetts, Melanye J. Brennan, Helen Marucci-Wellman, David A. Lombardi, Theodore K. Courtney, and Santosh K. Verma, "Circumstances of fall-related injuries by age and gender among community-dwelling adults in the United States: https://doi.org/10.1371/journal.pone.0176561, May 4, 2017.
6) J. Stevens, K. Thomas, L. Teh, and A. Greenspan, "Unintentional fall injuries associated with walkers and canes in older adults treated in U.S. emergency departments," J*ournal of the American Geriatrics Society*, vol. 57, no. 8, pp. 1,464–1,469, 2009.
7) "Developed a fall prevention robot walking vehicle (aist)," 2019. Accessed Oct. 31, 2020 (online). Available at: https://www.aist.go.jp/aist_j/press_release/pr2019/pr20191209/pr20191209.html
8) "Fuji hug L1." Accessed Oct. 31, 2020 (online). Available at: https://www.fuji.co.jp/en/items/hug/hugl1
9) Egoyan, Alexander & Moistsrapishvili, Karlo. (2013). "Equilibrium and Stability of the Upright Human Body," *General Science Journal*.
10) Dempster, "Space requirements of the seated operator," WADC Technical report, pp. 55–159, 1955.
11) Jim Richards, *The Comprehensive Textbook of Clinical Biomechanics 2nd Edition*, Elsevier, pp. 242–245, 2018, ISBN: 9780702054907.
12) Tomomitsu Kotake, MD, et al. "An Analysis of Sit-to-Stand Movements, *Arch Phys Med Rehabil Vol 74*. October 1993.
13) J. Bell, E. Kamienski, S. Teshigawara, H. Itagaki, and H. H. Asada, "Gear Ratio Optimization of a Multifunctional Walker Robot Using Dual-Motor Actuation," 2021 IEEE/RSJ International Conference on Intelligent Robots and Systems (IROS), 2021, pp. 9,339–9,346.
14) B.-S. Kim, J.-B. Song, and J.-J. Park, "A Serial-Type Dual Actuator Unit With Planetary Gear Train: Basic Design and Applications," IEEE/ASME Transactions on Mechatronics, vol. 15, no. 1, pp. 108–116, Feb. 2010.
15) H. Lee and Y. Choi, "A New Actuator System Using Dual-Motors and a Planetary Gear," IEEE/ASME Transactions on Mechatronics, vol. 17, no. 1, pp. 192–197, Feb. 2012.
16) A. Girard and H. H. Asada, "A two-speed actuator for robotics with fast seamless gear shifting," in 2015 IEEE/RSJ International Conference on Intelligent Robots and Systems (IROS), Sept. 2015, pp. 4,704–4,711.
17) A. Girard and H. H. Asada, "A practical optimal control approach for two-speed actuators," in 2016 IEEE International Conference on Robotics and Automation (ICRA), May 2016, pp. 4,572–4,577.
18) A. Girard and H. H. Asada, "Leveraging Natural Load Dynamics With Variable Gear-Ratio Actuators," *IEEE Robotics and Automation Letters*, vol. 2, no. 2, pp. 741–748, Apr. 2017.
19) J. Bell and H. H. Asada, "Design and Time-Optimal Control of a High-Speed High-Torque Dual-Motor Actuator," in 2020 American Control Conference (ACC), July 2020, pp. 1,017–1,024, ISSN: 2378-5861.

Seiichi Teshigawara

John Bell

Emily Kamiensky

Haruhiko Harry Asada

ROBUSTDYNA™ High Load Capacity Ultra-High-Speed Angular Contact Ball Bearings

Machine tools such as machining centers have in recent years been required for improved productivity, support of heavy cutting against the background of the increase in difficult-to-cut materials such as titanium alloys, and support of highly versatile machining (Figure 1) from roughing to finishing. In addition, for maintenance-free operation, demand has increased for long-term stable operation, such as extending the life of parts and avoiding unexpected operation stoppage due to collision. To meet these needs, a main shaft of a machine tool is required to have both high-speed and heavy cutting performance as well as high reliability.

Here we introduce the new ROBUSTDYNA (Photo 1) for main shaft bearings in machine tools, which resolves the above issue.

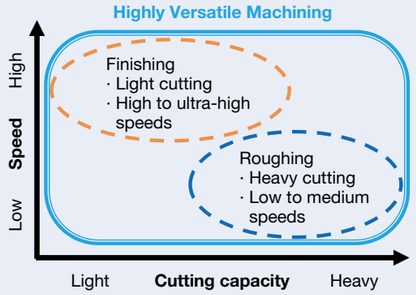

Fig. 1 Relationship between high speed and cutting ability in roughing and finishing

1. Configuration, Structure, and Specifications

For ROBUSTDYNA, we optimized the internal design such as adoption of a large-diameter ball to support high-speed rotation, as well as high load capacity and high impact resistance. We also adopted high-performance materials, such as ceramic balls for the rolling elements and NSK's proprietary heat-resistant steel for ultra-high-speed operation (SHX) for the inner and outer rings (Figure 2).

Photo 1 ROBUSTDYNA

		Conventional product	ROBUSTDYNA
Structure		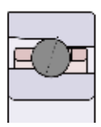	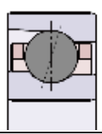
Portion	Ball	Ceramic	Ceramic (larger diameter)
	Inner ring/ outer ring	SHX	SHX

Note: The conventional product refers to the current NSKROBUST Series X Type.

Fig. 2 ROBUSTDYNA specifications

2. Features

2.1 High load capacity

By increasing load capacity by about 15% and dynamic load rating by about 40% compared to conventional products, the fatigue life has been extended by up to three times (Figure 3). This contributes to the heavy cutting of machine tools.

2.2 High impact resistance

By increasing impact resistance (static load rating) by about 15% compared to conventional products, the risk of bearing damage in the event of a collision has been reduced (Figure 4). This contributes to the long-term, stable operation of spindles.

2.3 Ultra-high-speed performance

Generally, $d_m \cdot n$, a pitch diameter of a rolling element (d_m) multiplied by rotational speed per minute (n) of a rotating shaft, is often used as an indicator of the high-speed performance of bearings. ROBUSTDYNA is compatible with the top-class $d_m \cdot n$ 300 × 10^4 as main shaft bearings in machine tools (Figure 5). This enables both heavy cutting and high-speed rotation, allowing for highly versatile machining.

3. Applications

This product is suitable for machine tools that perform heavy cutting and high-speed finishing, such as machining centers for aircraft and automobile parts.

4. Summary

This product has both high load capacity and high impact resistance while at the same time achieves high-speed rotation of $d_m \cdot n$ 300 × 10^4. This enables highly versatile machining by delivering excellent performance across both roughing and finishing machining operations, thereby contributing to the improvement of productivity and long-term stable operation. Moving forward, we will continue to expand the lineup of the ROBUSTDYNA Series.

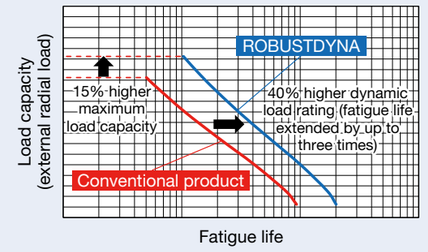

Fig. 3 Improvement of load capacity and life

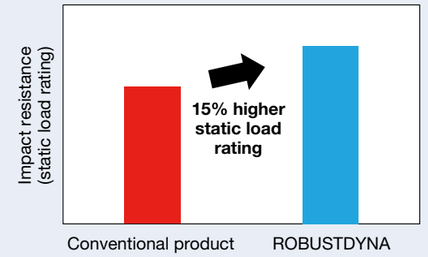

Fig. 4 Improvement of impact resistance

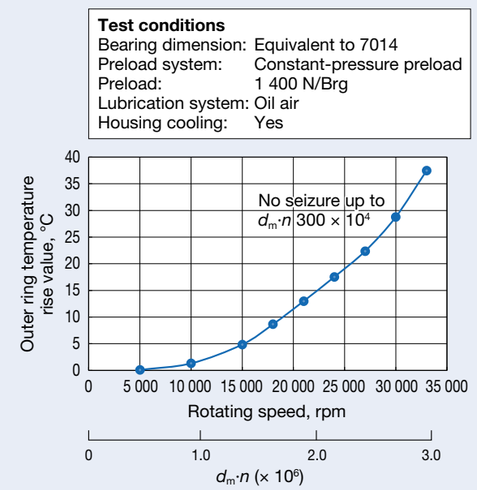

Fig. 5 High speed rotation test results for ROBUSTDYNA

Large Spherical Roller Bearings with Smearing Preventative (NSK DLC Coating)

Paper manufacturers recycle by collecting used paper and planting trees with the aim of realizing a carbon neutral society. Productivity improvement and CO_2 reduction are key issues for papermakers, so bearings are required to last longer and be reused through regular maintenance.

Depending on the location of a paper machine line that continuously manufactures paper, water infiltration may cause poor lubrication, and the slippage between the raceway surfaces of the inner and outer rings and the rolling surfaces may cause a small seizure called “smearing,” a type of surface damage (Photo 1). When such damage occurs, so does bearing vibration, which significantly lowers the quality of the paper. This may cause further damage, such as peeling and cracking, which could result in a shutdown of production equipment, so countermeasures based on bearings are essential.

To prevent smearing, NSK has developed a DLC* coating (hereinafter referred to as “NSK DLC coating”) that provides significantly improved adhesion and durability using NSK’s original coating technology. DLC is a hard coating made of the carbon located between diamond and graphite and is composed of a composite carbon layer and foundation layer. In bearing applications where a high surface pressure of several GPa is applied, improving the adhesion between the coating layers has been problematic. Therefore, using its proprietary technology, NSK has created a mechanism that substantially improves adhesion.

Conventionally, a spherical roller bearing with NSK DLC coating specifications has an outer diameter of 260 mm or less for the inner bearings of suction rolls. In recent years, however, smearing has been confirmed even for large bearings for press rolls having an outer diameter of 1 000 mm. In order to meet the demand for countermeasures, we have developed a large spherical roller bearing with NSK DLC coating that prevents smearing, as detailed below.

*Diamond-like carbon

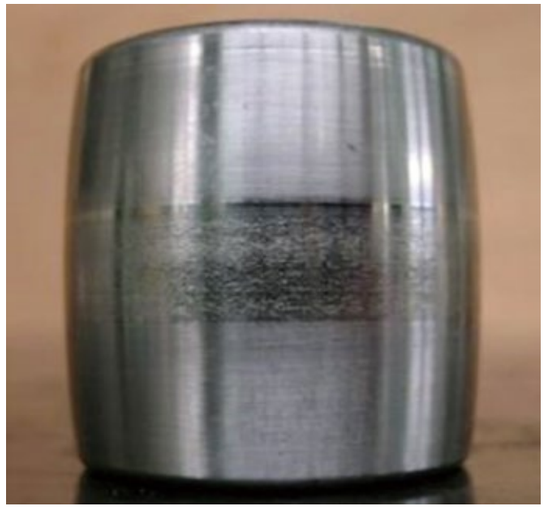

Photo 1 Smearing of roller rolling surface

1. Configuration, Structure, and Specifications

Photo 2 shows a large spherical roller bearing with NSK DLC coating on rolling elements. We have expanded the applicable size to an outer diameter of 1 000 mm, which can be applied to almost any size of spherical roller bearing used in paper machines.

Photo 2 Large spherical roller bearing with NSK DLC coating

2. Features

2.1 Improved adhesion between the DLC multilayer coating layers

For the foundation layer, we used a component with an atomic structure similar to that of the substrate. We also included an intermediate layer between the foundation and composite carbon layers and developed a DLC coating treatment technology in which the atomic structure gradually changes from the foundation layer to the composite carbon layer. This substantially improves adhesion between the coating layers, thus allowing for its application to rolling bearings on which there is high surface pressure (Figure 1).

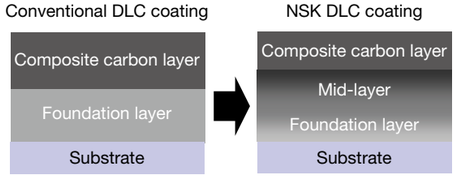

Fig. 1 Structure of NSK DLC coating

2.2 Application to large bearings

Optimizing the rolling element (roller) placement method and the coating condition setting in equipment for coating manufacturing has enabled a uniform DLC coating thickness to be applied to the surface of large rolling elements.

3. Applications

For roll support in paper machine lines with large spherical roller bearings, we recommend that the product be used in applications where smearing is the result of poor lubrication.

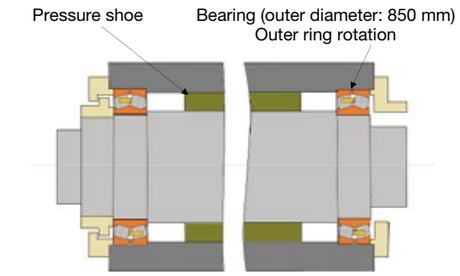

Fig. 2 Example of the structure of the Press Section CC Roll

4. Summary

Paper manufacturers dealing with smearing problems have confirmed that a large spherical roller bearing with NSK DLC coating is effective against long-term wear in actual machines (see Figure 2 for the Press Section CC Roll). We intend to continue meeting the technical needs of paper manufacturers and promoting the development of bearings that are environmentally friendly toward the realization of a carbon neutral society, thereby contributing to the paper manufacturing industry as a whole.

Low-Maintenance High-Reliability Gearbox Bearings for Railways

A drive unit (gear reducer) is a device used to transmit the output of a traction motor that drives the body of a railway vehicle to the axle. Due to the large vibrations generated between the railway track and wheels, the bearings that support the gear shafts must be highly reliable so they can be used for an extended period without damage, even under harsh conditions. Regular maintenance is essential to ensure such reliability.

Recently, the need for higher reliability and reduced maintenance for equipment and parts has increased due to higher demand for life-cycle cost reductions in the railway industry. NSK has developed highly reliable cylindrical roller bearings and four-point contact ball bearings (Photo 1) for pinion gears in a drive unit to meet these needs, as described in this article.

1. Configuration, Structure, and Specifications

Our highly reliable cylindrical roller bearings and four-point contact ball bearings have a high-strength cage that follows the design concept of tapered roller bearings for pinion gears in a drive unit with significant benefits and reduced maintenance when mounted.

2. Features

(1) Application of the high-strength cage

Since bearings for a drive unit are used for an extended period and must bear large vibrations and shocks from the railway track, they need to be highly reliable, so cage strength is particularly important. For the developed cylindrical roller bearing, we have introduced a high-strength cage design that optimizes the shape of the cage and reduces the stress generated in it by up to 75% compared to conventional models, according to our estimations. We will make further improvements to reliability in order to contribute to the safety and security of railway vehicle operation (Figure 1).

Photo 1 High-reliability gearbox cylindrical roller bearings and four-point contact ball bearings

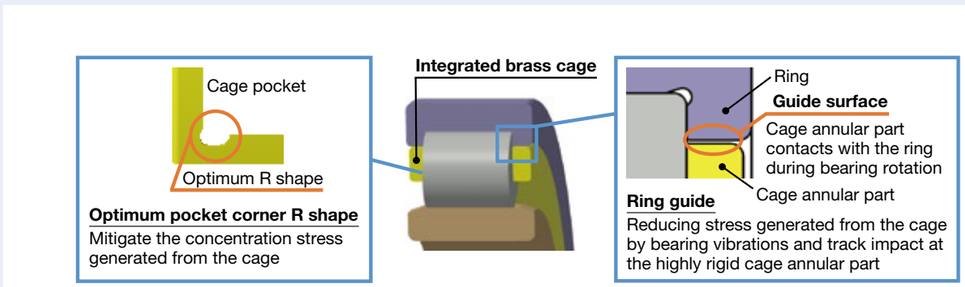

Fig. 1 Features of the cylindrical roller bearings (developed product)

(2) Improvement of maintainability

The tapered roller bearings primarily used in drive units in Japanese vehicles require axial clearance adjustment when mounting the bearings, necessitating the use of advanced technology and a substantial time investment. We ship our newly developed four-point contact ball bearings with the bearing clearance adjusted in advance, so the final product does not require clearance adjustment work when mounting the bearing, thus reducing the life-cycle cost by saving labor for maintenance (Figure 2).

3. Applications

This product can be used for pinion gear shafts in a drive unit for railway vehicles traveling at all speeds, from high-speed vehicles such as bullet trains to medium- and low-speed vehicles such as for subways and conventional railway lines.

4. Summary

By introducing this product, we are contributing to the safety and security of railway vehicles and reducing their life-cycle costs by reducing drive unit maintenance.

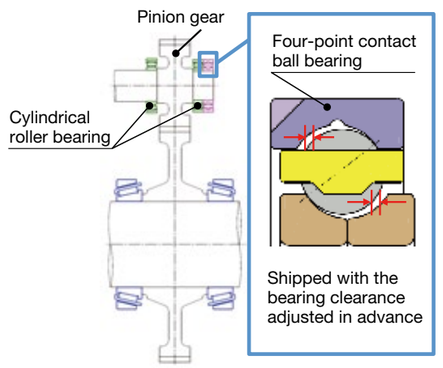

Fig. 2 Features of the four-point contact ball bearings (Developed product)

NSK Linear Guides™ Long-Life Series: DH/DS Models

NSK linear guides are used in a wide range of applications, including production equipment. Due to increased development of smart factories in recent years, and subsequent demand for continuous day and night operation as well as higher levels of productivity, improving the reliability of linear guides and increasing their life has become crucial.

We have achieved high load capacity in standard series NH/NS models by optimizing the often used raceway groove shape design. Long life series DH/DS models (Photo 1) introduced in this article have inherited the features of standard series NH/NS models but with double the life.

Photo 1 NSK Linear Guides™ Long-Life Series: DH/DS Models

1. Specifications

The long-life DH model has a larger ball diameter and the world's highest level of dynamic load rating, whereas the DS model has a compact shape with a reduced assembly height. The available sizes and ball slide shapes are the same as those of the standard series; 13 sizes are available, 15 to 65 for the DH model and 15 to 35 for the DS model. This enables support for various configurations (Table 1). Each has dimensions and accuracy that are completely compatible with standard NH/NS models, and replacing standard NH/NS models with DH and DS models easily allows for greater life.

Table 1 Range supported by long-life DH/DS linear guides

Model (size)		Ball slide shape	
		Square	Flanged
High load	DH15	AN	EM
	DH20	AN	EM
	DH25	AL, AN	EM
	DH30	AL, AN	EM
	DH35	AL, AN	EM
	DH45	AL, AN	EM
	DH55	AL, AN	EM
	DH65	AN	EM
Ultra-high load	DH15	BN	GM
	DH20	BN	GM
	DH25	BL, BN	GM
	DH30	BL, BN	GM
	DH35	BL, BN	GM
	DH45	BL, BN	GM
	DH55	BL, BN	GM
	DH65	BN	GM

Model (size)		Ball slide shape	
		Square	Flanged
High load	DS15	AL	EM
	DS20	AL	EM
	DS25	AL	EM
	DS30	AL	EM
	DS35	AL	EM
Medium load	DS15	CL	JM
	DS20	CL	JM
	DS25	CL	JM
	DS30	CL	JM
	DS35	CL	JM

2. Features

2.1 Twice the life of conventional products

In order to improve the reliability and increase the life of DH/DS models, we applied NSK's original TF "Tough" (heat treatment) technology, which is the result of bearing development. Through many durability tests, we have verified that linear guides with TF technology applied have longer life, and we have been marketing the products as having twice the life of conventional products. In addition to doubling the life, this process reduces the size of the equipment (Figure 1).

TF technology, originated by and proprietary to NSK, is a heat treatment application that allows for a longer life in rolling elements by controlling the amount of retained austenite in steel. Optimizing the amount of retained austenite softens the contours of indentations at the ball groove formed when a ball rolls over a contaminant. This technology suppresses flaking from the contours of indentations, thereby improving fatigue life (Figure 2).

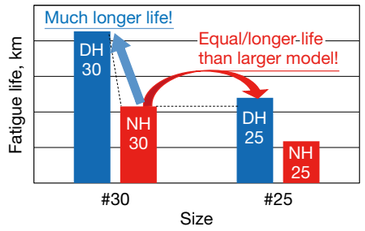

Fig. 1 Examples of improved reliability and size reduction

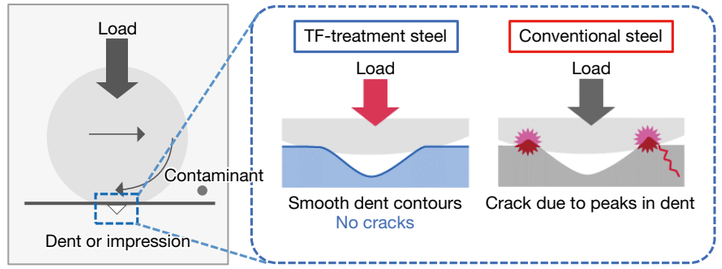

Fig. 2 Principle of extended life by TF processing

2.2 Wide range of options

Similar to standard series NH/NS models, DH/DS models offer a wide range of options. These include the lubricating unit NSK K1-L, which allows for long-term, maintenance-free usage by gradually supplying lubricating oil that seeps out from a porous resin, and highly dust-resistant side seals with a multi-lip structure that substantially improve dustproof performance. Long-life series users can therefore apply the linear guides to various types of equipment or devices in a number of different environments.

3. Applications

DH/DS models have a longer life and contribute to a reduction in the size of various equipment such as that used for semiconductor and liquid crystal manufacturing, automobile manufacturing, conveyance robots, and platform doors.

4. Summary

NSK Linear Guides™ Long-Life Series: DH/DS Models are more reliable and allow for increased productivity, with significantly extended life in addition to being lighter in weight, generating less friction, and contributing to energy savings due to reduction of equipment size. NSK will continue to make efforts toward extending the life of linear guides in order to improve the reliability and productivity of machines and other equipment.

Wireless Vibration Diagnostic Device Model D-VibA10

Rolling bearings are relatively simple mechanical elements used in a variety of rotating machines, but loss of their function due to damage often leads to functional loss of the entire mechanical system. For this reason, condition monitoring during bearing operation is one of the most important tasks to ensure stable operation of the mechanical system as a whole.

Typically, such condition monitoring relies on veteran maintenance personnel determining the condition of a machine by using advanced vibration analysis devices in accordance with tactile and auditory sensations. However, sometimes that method creates problems due to differing judgments between personnel or hesitation in making such determinations.

To solve such problems, NSK has developed the Wireless Vibration Diagnostic Device Model D-VibA10 incorporating ACOUS NAVI for Bearings, an application of the Condition Monitoring and Diagnosis Software (ACOUS NAVI™) series based on vibration diagnosis technology for bearings and linear motion products, on which NSK has been working for many years. Here we introduce this product.

1. Configuration, Structure, and Specifications

This product, despite its compact body being equivalent to the size of a human palm, is a vibration diagnostic device consisting of a vibration pickup equipped with vibration detection, analysis calculation, and battery functions as well as a dedicated application that users can install on their Android smartphone from a Google Play store (Photo 1). By connecting the vibration pickup to a smartphone via Bluetooth and attaching it to a rotating machine while operating, users can diagnose vibration measurement and damage, such as bearing flaking, on the spot.

Each vibration measurement datum saved in the smartphone can be transferred to a computer installed management software, and users can manage the vibration state in chronological order for each machine and piece of equipment.

In addition, users can set the measurement and analysis conditions using the management software for each walk-around check route and the equipment to be inspected, so maintenance efficiency improves since users can transfer such conditions to a smartphone in advance.

Table 1 shows the specifications of the D-VibA10 model.

2. Features

To quantify the vibration phenomena and causes that rotating machines generate, this product is equipped with a diagnostic solution that automatically extracts and determines specific vibration components caused by bearing damage, in addition to measurement and analysis functions such as vibration meters, FFT analyzers, and oscilloscopes.

We have taken the following measures in terms of functionality, operability, and data management to ensure suitability for inspections of machinery and equipment.

Figure 1 shows the functions of this product.

(1) Instant diagnostic device

Once the user attaches the vibration pickup to the rotating equipment, they can identify damage, such as bearing flaking and scratches, on the spot and simply by setting the bearing number and rotation information, even if there is no previous vibration data.

Photo 1 Wireless Vibration Diagnostic Device Model D-VibA10

Table 1 Specifications

Component	Item		Specifications
Common	Wireless communication		Bluetooth
	Dedicated application startup OS		Android 8 or later
	Management software startup OS		Windows 10
Vibration value	Measuring frequency band	Displacement	10 Hz – 1 kHz
		Velocity	10 Hz – 1 kHz
		Acceleration	10 Hz – 20 kHz
Vibration pickup	System		Piezoelectric acceleration
	Dimension		ϕ48 × 81 (H) mm
	Weight		170 g
	Operating temperature range		+5°C – +50°C
	Dustproof and waterproof environment		IP 65
	Operating power supply		Rechargeable lithium-ion battery
	Material		SUS, aluminum alloy, composite resin
USB dongle	Data management		Management software

(2) Re-diagnosis function

Since users can re-diagnose the stored data by changing the bearing damage judgment level and bearing conditions, re-measurement is unnecessary.

(3) Measurement mode tailored to the applications

Measurement mode has two options: manual and automatic. Manual measurement mode is suitable for spot measurement because users can arbitrarily select the measurement and analysis functions. Automatic measurement mode is suitable for walk-around checks because it can collectively process the measurement and store the information by associating the equipment with the measurement and analysis conditions.

(4) Applicable to components other than bearings

The vibration value analysis uses three types of measurement functions: displacement, velocity, and acceleration. The measurement function for velocity conforms to the vibration severity evaluation standard of ISO 10816, and the rank of unbalance and misalignment of the rotating part is automatically determined. The measurement function for acceleration analyzes the general mechanical vibration, removes disturbance by filtering, and converts vibration into sound.

(5) Management software

When users transfer the saved data from a smartphone to the computer, it creates a folder for each measured machine and displays the trend graph of vibration values and each waveform. In addition, to re-diagnosis under the changed-bearing, damage judgment level and bearing conditions, users can output each waveform as a file in CSV format. Also, since users can automatically create an equipment diagnosis report (Figure 2) based on various measurement data, they can transmit and share information quickly. Furthermore, since users can set the measurement and analysis conditions and walk-around check route in the automatic measurement mode and transfer them to a smartphone, efficient operation is possible without the assistance of maintenance personnel.

(6) Installation of dedicated application

The application is available at Google Play stores, which can be accessed simply by connecting an Android smartphone or tablet to the Internet.

3. Applications

This product is suitable for general-purpose rotating machines such as motors, fans, pumps, and spindles that operate at a constant velocity.

4. Summary

This product is an all-in-one diagnostic device equipped with a bearing damage diagnostic function in addition to a function to measure, analyze, and trace the vibration of machinery. We hope this product can contribute to improving efficiency and reducing labor in equipment maintenance while also serving as a tool to prevent failures.

For more information, go to:
https://www.acousnavi.nsk.com/en/lp-a10.html

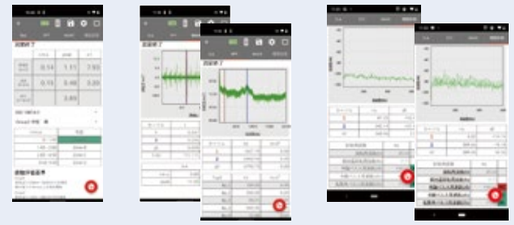

(1) Vibration measurement (2) FFT Analysis/Time domain wave (3) Bearing diagnosis

Fig. 1 Functions

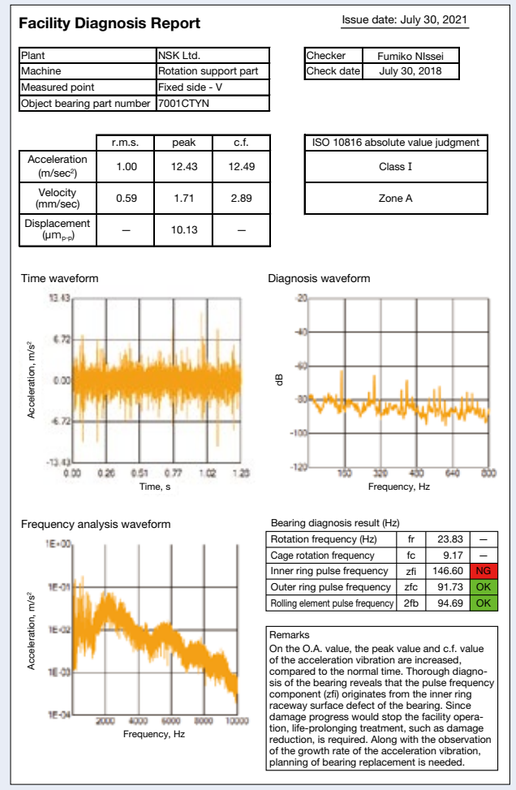

Fig. 2 Equipment diagnosis reports

Condition Monitoring Application Software ACOUS NAVI™ (FIELD System)

The FIELD System is an IoT platform for the manufacturing industry provided by FANUC Corporation. It allows users to easily build customized IoT systems for production equipment by downloading various application software (apps) from a dedicated online store on the network, such as monitoring the operation of production lines and predictive maintenance of equipment (Figure 1). The FIELD System also allows for the purchase of various apps from various developers via dedicated online stores.

NSK has been advancing technology for diagnosing bearing and ball screw conditions, and we have incorporated our technical developments into our bearing and ball screw condition diagnostic app ACOUS NAVI. Here we introduce this app for the FIELD System because it is currently available in online stores.

Fig. 1 Conceptual diagram of the FIELD System (cited from FANUC Corporation's homepage)

1. Configuration, Structure, and Specifications

The condition diagnostic app ACOUS NAVI for the FIELD System runs on the dedicated hardware FIELD System BOX, provided by FANUC Corporation. The system creates a file for vibration data measured with a vibration sensor, which is installed near the bearing and ball screw. Next, it transfers the file to the FIELD System BOX using PLC or another device, and the user can then download Acous Navi into the FIELD System BOX from a dedicated online store (Figure 2). Users can confirm the analysis results of ACOUS NAVI using a browser on a PC connected to the FIELD System BOX via the network, which displays the results of the bearing and ball screw conditions as well as the trend graph of the vibration values. At the time of this report, ACOUS NAVI for Bearings (app for bearings) and ACOUS NAVI for Ball Screws (app for ball screws) had been uploaded to an online store.

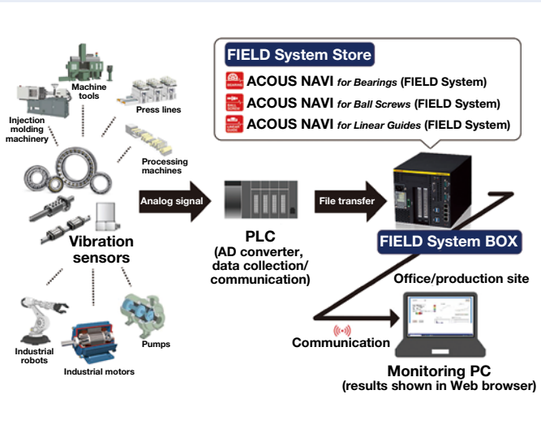

Fig. 2 System configuration

2. Features

Users can configure a bearing and ball screw diagnostic system with the following features by using the FIELD System and this product.

(1) Unique bearing diagnostic algorithm
The system features a unique diagnostic algorithm developed by NSK as a specialist bearing manufacturer, and the system registers vibration pulse frequency due to bearing defects in a database. System users can automatically detect bearing scratches and flaking and diagnose them at an early stage by selecting the bearing number to be diagnosed and inputting the rotation information (Figure 3).

(2) Unique ball screw diagnostic algorithm
The system features a unique diagnostic algorithm developed by NSK as the specialist ball screw manufacturer. By regularly monitoring the index of wear deterioration of the ball screw, users can detect damage deterioration at an early stage and prevent mechanical problems caused by wear deterioration (Figure 4).

(3) Diagnosis of a maximum of 32 parts
The system can collectively diagnose up to 32 parts for multiple bearings or ball screws in equipment (Figure 5).

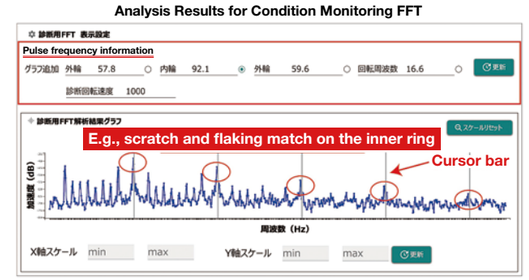

Fig. 3 Analysis results graph from ACOUS NAVI for Bearings (bearing diagnostics app)

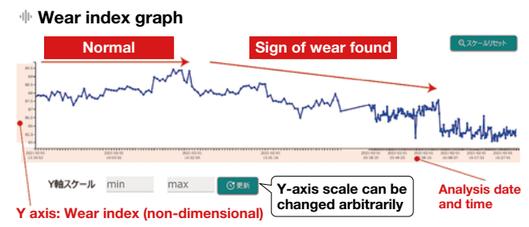

Fig. 4 Analysis results graph from ACOUS NAVI for Ball Screws (ball screw diagnostics app)

3. Applications

This product is suitable for equipment in which abnormalities in bearings and ball screws have a large effect on downtime, from general-purpose rotating machines such as motors, pumps, and spindles in production plants to system products such as compressors and machine tools.

4. Summary

Manufacturers use bearings and ball screws in mechanical systems in various environments and operating conditions, and early detection of bearing and ball screw abnormalities contributes to reducing downtime in production equipment and improving factory productivity.

This product incorporates an automatic diagnostic algorithm that can determine defects in bearings and ball screws without specialized skills. We are introducing it in anticipation of widespread use of IoT platforms and increased factory productivity, and we hope it will contribute to raising that level of productivity.

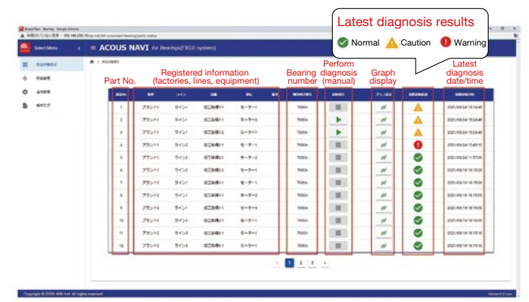

Fig. 5 List of analysis results

High Efficiency Tapered Roller Bearings for Powertrains

With the recent tightening of global environmental regulations and increasing environmental awareness of consumers, there is strong demand to reduce CO_2 emissions and improve the fuel efficiency of automobiles. In addition, demand is increasing for lower friction rolling bearings used in automotive powertrains.

Various types of rolling bearings are used for powertrains, but tapered roller bearings are widely used in areas requiring high support rigidity and high load capacity (Photo 1).

Given the above, NSK has been developing tapered roller bearings with lower friction since 1980. In 2017, we announced the development of sixth-generation low-friction tapered roller bearings for automotive transmissions that contribute to higher fuel economy. In this article, we introduce the effects of the reduced friction achieved through that development.

Photo 1 High efficiency tapered roller bearings for powertrains

1. Configuration, Structure, and Specifications

Friction in tapered roller bearings consists of (1) rolling friction produced between the roller and raceway surface, (2) sliding friction produced between the roller end face and the inner ring large rib, and (3) lubricating oil agitation loss when the bearing rotates. We focused on each friction factor and, by making improvements, have gradually reduced the friction of the bearings in the first to sixth generations (Figures 1 and 2).

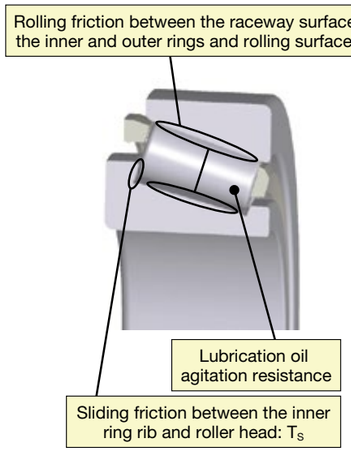

Fig. 1 Friction factors for TRBs

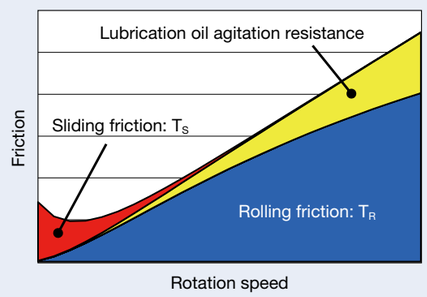

Fig. 2 Relationship between rolling friction T_R and sliding friction T_S

Each of the first to third generations improved sliding parts, optimized internal specifications, and miniaturized using life-extension technology, thus achieving a total friction reduction of about 35%. The characteristics of the fourth to sixth generations are explained as follows.

2. Features

· Fourth generation

By changing the shape of the inner and outer ring raceway surfaces from a single or compound arc shape (standard crowning shape) to a special barrel shape (special crowning shape), we made the raceway surface uniform through distribution of the contact surface pressure generated on the roller, and we significantly suppressed the edge load generated at both ends.

This reduced rolling friction by about 30% while also further reducing the size and weight of the bearing (Figure 3).

· Fifth generation

We have conventionally used a press-molded iron cage, but by adopting a specially shaped resin cage that controls the amount of lubricating oil flowing into the bearing, we significantly reduced lubricating oil agitation loss. This reduced friction by about 20% in the high-speed rotation range (Figure 4).

· Sixth generation

By significantly improving the roughness of the large rib face of the inner race and the roller end face, which are both sliding parts, and compared to the base specifications, we were able to reduce sliding friction by up to 60% in the low-speed range and up to 20% on average for all rotation speeds (Figure 5).

3. Applications

We can apply the friction reduction technology used in this example to areas other than automotive powertrains, e.g., tapered roller bearings used in other automotive applications and various industrial machinery fields.

4. Summary

Currently, the base specification of tapered roller bearings for automotive powertrains is the third generation, but by applying the fourth to sixth generations, we can reduce friction by an additional 45%.

Going forward, NSK will continue to contribute to improving the fuel efficiency of automobiles by promoting the development of new products that meet market demand.

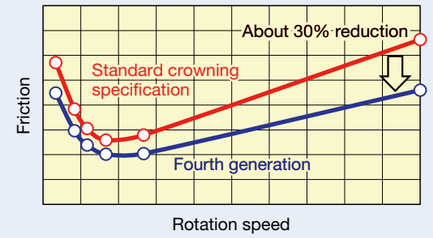

Fig. 3 Friction measurement results for fourth generation TRBs

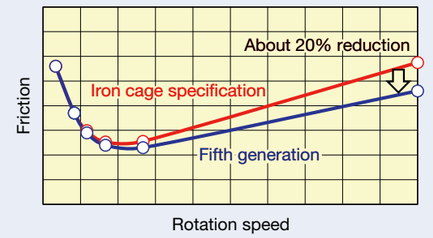

Fig. 4 Friction measurement results for fifth generation TRBs

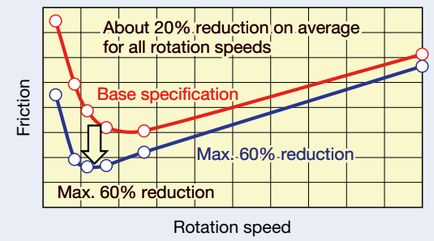

Fig. 5 Friction measurement results for sixth generation TRBs

Pressed Angular Contact Ball Bearings for Electric and Hybrid Vehicles

Due to rising concern for the environment in recent years, automobile manufacturers have been shifting from conventional internal combustion engine vehicles to electric vehicles such as HEVs and EVs in an effort to reduce CO_2 emissions. As a result, automobile-related companies are rushing to develop products with lower torque and lower fuel consumption in order to reduce those emissions by improving fuel consumption.

In response, NSK has developed a pressed angular contact ball bearing, the main purpose of which is to contribute to the development of EVs. Here we introduce this new product.

Photo 1 Pressed angular contact ball bearings

1. Applications

The bearing is mainly applied to applications with a built-in multi-plate friction material type of clutch, such as a P2 HEV (using a structure in which a motor is placed between the starter clutch and transmission) and a dedicated hybrid transmission (DHT).

In the clutch application for a P2 HEV (Figure 1), the multi-plate friction materials engage each other via the hydraulic piston when the gears change. Hydraulic pistons are classified into the rotary hydraulic chamber type and fixed hydraulic chamber type, and the latter simplifies oil passage by reducing the number of oil seals in the piston, thus reducing oil pump loss and improving fuel efficiency.

At this point, we place the pressed angular contact ball bearing between the hydraulic piston and the multi-plate friction material in order to eliminate the need of directly transmitting the rotation of the multi-plate friction material to the hydraulic piston when the materials are engaged.

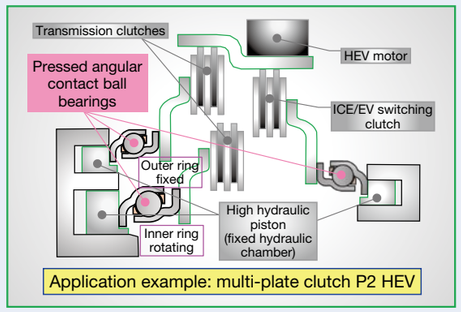

Fig. 1 Application example: multi-plate clutch P2 HEV

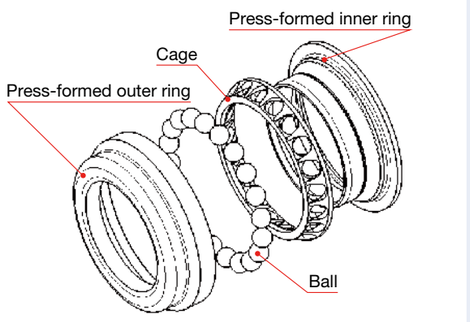

Fig. 2 Exploded view of a pressed angular contact ball bearing

2. Configuration, Structure, and Specifications

Whereas manufacturing the inner and outer rings of conventional angular contact ball bearings requires forging and shaving, the inner and outer rings of pressed angular contact ball bearings are press formed precisely. Each component (e.g., bearing ring, ball) is inseparable, making assembly easier for customers (Figure 2). At the time of assembly, the inner ring and outer ring are not press-fitted into the peripheral parts but rather installed in a floating (loose) state in the radial direction. Therefore, when a load is applied, the axial load transmits rotationally on the ends of the inner and outer rings.

3. Features

3.1 Low torque

Ball bearings have lower rotational torque than needle bearings. Figure 3 shows typical rotational torque calculation results comparing a thrust needle bearing and a pressed angular contact ball bearing with the same rated load.

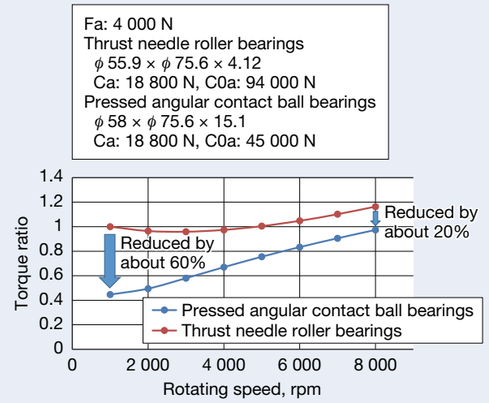

Fig. 3 Torque comparison of pressed angular contact ball bearing and thrust needle roller bearing

3.2 Robustness under a tilted environment

When the thrust needle bearing is in a tilted environment (Figure 4), the bearing ring follows the opposing tilt, so edge load (local excessive surface pressure) occurs between the rolling element and bearing ring, which can cause flaking (Figure 5). With a pressed angular contact ball bearing, however, we can avoid excessive localized surface pressure even in cases where it follows the opposing tilt because the rolling element is a ball.

3.3 Self-alignment action

In the clutch application for a P2 HEV, assemblers install a bearing in a floating (loose) state, and due to the responsiveness when changing gears, that bearing requires a function that allows it to perform self-alignment from the loose state during operation (load + rotation). With a thrust needle bearing, when we apply a self-alignment action, it pinches the cage in a radial direction between the two bearing rings, which may lead to breakage. On the other hand, with a pressed angular contact ball bearing, the bearing ring is supported by balls, making cage breakage impossible (Figure 6). In addition, pressed angular contact ball bearings have excellent alignment responsiveness (Figure 7).

3.4 Ease of assembly

Use of a conventional angular contact ball bearing requires press-fitting the bearing ring into the opposing component. On the other hand, pressed angular contact ball bearings do not require press-fitting into other components, and each component is inseparable, so it is very easy to assemble.

4. Summary

We believe that our new pressed angular contact ball bearing will contribute to the development of EVs as an innovative product using precision press technology.

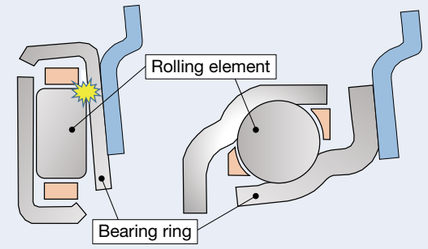

Fig. 4 Robustness in a tilted environment

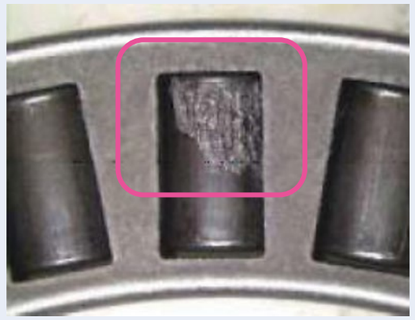

Fig. 5 Edge load spalling of thrust needle roller bearing under a tilted environment

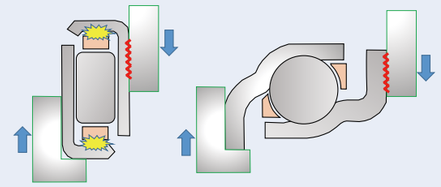

Fig. 6 Comparison of behavior during self-alignment

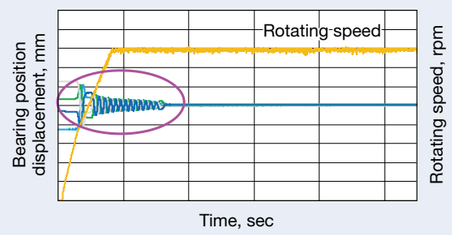

Fig. 7 Self-alignment test results

Thrust Needle Roller Bearings with Electrical Corrosion Resistance

In the midst of a major transformation in automobile manufacturing, electrified powertrains are rapidly becoming more common in fusions of transmissions and motors in various styles, as seen in electric vehicles (EVs) and hybrid electric vehicles (HEVs). It is likely that the bearings used in such powertrains will need to support not only conventional functional requirements but also the prevention of electrical corrosion, which is unique to electrified powertrains.

In response, NSK has developed a thrust needle roller bearing with electrical corrosion resistance (Photo 1), which features an insulating function within a conventional thrust needle roller bearing to provide electrical corrosion resistance. Here we introduce this product.

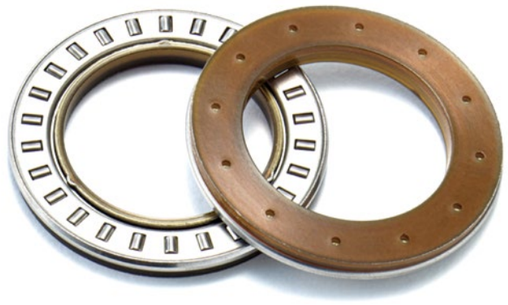

Photo 1 Thrust needle roller bearings with electrical corrosion resistance

1. Background

EVs and HEVs, especially “strong hybrid” vehicles, have electric transmissions that actively drive, generate, and regenerate electricity using a motor and have close combinations of gears and motors in the transmissions. When bearings used in the structure are on the energizing path, their performance may suffer due to electrical corrosion. This corrosion often occurs on bearings that support the rotor rotation of motors, but it may also occur if there is a needle bearing on the energizing path beyond that bearing.

Figure 1 shows an example of electrical corrosion on a thrust needle roller bearing where unevenness unique to electrical corrosion appears in a striped pattern or a ridge-mark.

Electrical corrosion of a thrust needle roller (striped pattern = ridge mark)

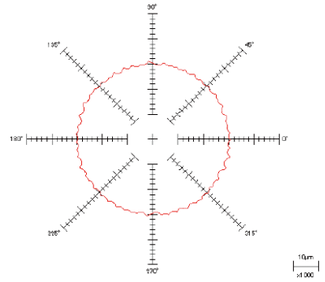

Unevenness on a thrust needle roller (indicated by ridge mark)

Fig. 1 Example of electrical corrosion on thrust needle roller bearings

2. Structure and Specifications

In this case, the resin integrates into the race, i.e., the bearing ring, of the thrust needle roller bearing to insulate the current supply to the bearing and prevent electrical corrosion.

To integrate the race and resin, we used insert molding, in which the resin is injection molded, with the race inserted in the injection mold.

Figure 2 shows the cross-sectional shape of the product and the insert-molded race.

When integrating the race and resin, it is necessary to fix the resin portion to the race and suppress the swell remaining in the race. Fixing the resin to the race requires molding the resin in the recess of the tab for preventing cage disassembly. We must suppress the swell to obtain a flat resin back face such that the race is flat at the time of injection.

With this product, we have accomplished all of the above by devising an innovative mold structure.

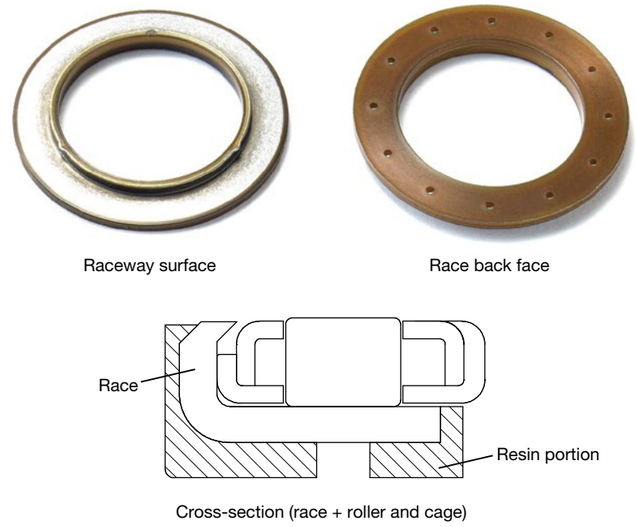

Fig. 2 Specifications and structure of product

3. Performance

Figure 3 shows the electrical resistance of resins as the insulation performance measure for this new product. To confirm the influence of changes in the physical properties of the resin, we measured the resin’s moisture state by using two types of products, one dry and the other moisture-absorbent.

The measurement of the dry product showed resistance values exceeding 1.0×10^{10} Ω, while the measurement of the moisture-absorbent product (water content equivalent to 7%) showed resistance values exceeding 1.0×10^{6} Ω. Insulation performance of 1.0×10^{6} Ω or more is sufficient according to an index of general insulators.

However, in the actual bearing usage environment, the resistance value is likely to decrease due to the temperature rise, so we must confirm the insulation performance in the actual machine or in the actual bearing usage environment.

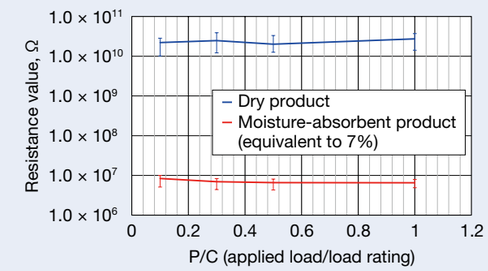

Fig. 3 Results of electrical resistance measurement

4. Applications

The new product can be applied not only to EV and HEV transmissions but also in places that require a “current cutoff + rotational support of thrust load” function.

In addition to preventing electrical corrosion of the thrust needle bearing, this product also insulates the energizing path. Therefore, by applying the product, we can contribute to improvements in structural designs requiring electrical measurements.

5. Summary

There is widespread demand for countermeasures against electrical corrosion, and we expect this demand to increase even further in the future. Since bearings are indispensable for mechanical transmission mechanisms, we are confident that demand for this new product will increase dramatically.

Worldwide Sales Offices

P: Phone F: Fax ☆: Head Office

NSK LTD.-HEADQUARTERS, TOKYO, JAPAN

Nissei Bldg., 1-6-3 Ohsaki, Shinagawa-ku, Tokyo 141-8560, Japan

INDUSTRIAL MACHINERY BUSINESS DIVISION-HEADQUARTERS
P: +81-3-3779-7227 F: +81-3-3779-7432

AUTOMOTIVE BUSINESS DIVISION-HEADQUARTERS
P: +81-3-3779-7189 F: +81-3-3779-7917

●Africa

South Africa:

NSK SOUTH AFRICA (PTY) LTD.

SANDTON 25 Galaxy Avenue, Linbro Business Park, Sandton 2146, South Africa
P: +27-011-458-3600 F: +27-011-458-3608

●Asia and Oceania

Australia:

NSK AUSTRALIA PTY. LTD.

MELBOURNE ☆ 100 Logis Boulevard, Dandenong South, Victoria, 3175, Australia
P: +61-3-9765-4400 F: +61-3-9765-4466

SYDNEY Suite A315, 20 Lexington Drive, Bella Vista, New South Wales, 2153, Australia
P: +61-2-9839-2300 F: +61-2-8824-5794

BRISBANE 1/69 Selhurst Street, Coopers Plains, Queensland 4108, Australia
P: +61-7-3347-2600 F: +61-7-3345-5376

PERTH Unit 1, 71 Tacoma Circuit, Canning Vale, Western Australia 6155, Australia
P: +61-8-9256-5000 F: +61-8-9256-1044

New Zealand:

NSK NEW ZEALAND LTD.

AUCKLAND Unit F, 70 Business Parade South, Highbrook, Business Park Auckland 2013, New Zealand
P: +64-9-276-4992 F: +64-9-276-4082

China:

NSK (SHANGHAI) TRADING CO., LTD.

JIANGSU No.8 NSK Rd., Huaqiao Economic Development Zone, Kunshan, Jiangsu, China (215332)
P: +86-512-5796-3000 F: +86-512-5796-3300

NSK (CHINA) INVESTMENT CO., LTD.

JIANGSU ☆ No.8 NSK Rd., Huaqiao Economic Development Zone, Kunshan, Jiangsu, China (215332)
P: +86-512-5796-3000 F: +86-512-5796-3300

BEIJING Room 1906, Beijing Fortune Bldg., No.5 Dong San Huan Bei Lu, Chao Yang District, Beijing, China (100004)
P: +86-10-6590-8161 F: +86-10-6590-8166

TIAN JIN Unit 4604, 46/F., Metropolitan Tower, 183 Nanjing Road, Heping District, Tianjin, China (300051)
P: +86-22-8319-5030 F: +86-22-8319-5033

CHANGCHUN Room 902-03, Changchun Hongwell International Plaza, No.3299 Renmin Street, Changchun, Jilin, China (130061)
P: +86-431-8898-8682 F: +86-431-8898-8670

SHENYANG Room 1101, China Resources Building, No. 286 Qingnian Street, Heping District, Shenyang Liaoning, China (110004)
P: +86-24-2334-2868 F: +86-24-2334-2058

DALIAN Room 1805 Xiwang Tower, No.136 Zhongshan Road, Zhongshan District, Dalian, Liaoning, China (116001)
P: +86-411-8800-8168 F: +86-411-8800-8160

NANJING Room A1 22F, Golden Eagle International Plaza, No.89 Hanzhong Road, Nanjing, Jiangsu, China (210029)
P: +86-25-8472-6671 F: +86-25-8472-6687

FUZHOU Room 1801-1811, B1#1A Class Office Building, Wanda Plaza, No.8 Aojiang Road, Fuzhou, China (350009)
P: +86-591-8380-1030 F: +86-591-8380-1225

WUHAN Room 1512, No.198Yuncai Road, Office Building, Oceanwide City Square, JiangHan, District, WuHan, China (400039)
P: +86-27-8556-9630 F: +86-27-8556-9615

QINGDAO Room 802, Farglory International Plaza, No.26 Xianggang Zhong Road, Shinan District, Qingdao, Shandong, China (266071)
P: +86-532-5568-3877 F: +86-532-5568-3876

GUANGZHOU Room 1011-16, Yuexiu Financial Tower, No.28 Zhujiang Road East, Zhujiang New Town, Guangzhou, Guangdong, China (510627)
P: +86-20-3817-7800 F: +86-20-3786-4501

CHANGSHA Room 3209, Huayuan International Center, No.36, Section 2, Xiangjiang Middle Road, Tianxin District, Changsha, Hunan, China (410002)
P: +86-731-8571-3100 F: +86-731-8571-3255

LUOYANG Room 955, HUA-YANG PLAZA HOTEL, NO.88 Kaixuan W.Rd., Jian Xi District, Luoyang,Henan Province, China (471003)
P: +86-379-6069-6188 F: +86-379-6069-6180

XI'AN Room 1007, B Changan Metropolls Center, No.88 Nanguanzheng Steet, Xi'an, Shanxi, China (710068)
P: +86-29-8765-1896 F: +86-29-8765-1895

CHONGQING Room 612, Commercial Apartment, Athestel Hotel, No.288, Keyuan Rd.4, Jiulongpo District, Chongqing, China (400039)
P: +86-23-6806-5310 F: +86-23-6806-5292

CHENGDU Room1117, Lippo Tower, No.62 North Kehua Road, Chengdu, Sichuan, China (610041)
P: +86-28-8528-3680 F: +86-28-8528-3690

NSK CHINA SALES CO., LTD.

JIANGSU No.8 NSK Rd., Huaqiao Economic Development Zone, Kunshan, Jiangsu, China (215332)
P: +86-512-5796-3000 F: +86-512-5796-3300

NSK HONG KONG LTD.

HONG KONG ☆ Suite 705, 7th Floor, South Tower, World Finance Centre, Harbour City, T.S.T, Kowloon, Hong Kong, China
P: +852-2739-9933 F: +852-2739-9323

SHENZHEN Room 624-626, 6/F, Kerry Center, Renminnan Road, Shenzhen, Guangdong, China
P: +86-755-25904886 F: +86-755-25904883

Taiwan:

TAIWAN NSK PRECISION CO., LTD.

TAIPEI ☆ 10F-A6, No.168, Sec.3, Nanjing East Rd., Zhongshan Dist., Taipei City 104, Taiwan
P: +886-2-2772-3355 F: +886-2-2772-3300

TAICHUNG 3F. -2, No. 540, Sec. 3, Taiwan Blvd., Xitun Dist., Taichung City 407, Taiwan
P: +886-4-2708-3393 F: +886-4-2708-3395

TAINAN Rm. A1, 9F., No.189, Sec. 1, Yongfu Rd., West Central Dist., Tainan City 700, Taiwan
P: +886-6-215-6058 F: +886-6-215-5518

India:

NSK BEARINGS INDIA PRIVATE LTD.

CHENNAI ☆ TVH Beliciaa Towers, 2nd Floor, Block I, No.71/1, MRC Nagar Main Road, MRC Nagar, Chennai-600 028,India
P: +91-44-2847-9600 F: +91-44-2847-9601

MUMBAI No.321, A Wing, Ahura Centre, 82, Mahakali Caves Road, Andheri (E), Mumbai-400 093, India
P: +91-22-2838-7787

JAMSHEDPUR 13/A, 2nd Floor, Circuit House Area, North West Layout, Road No.12, (Near Sai Baba Mandir), Sonari, Jamshedpur–831 011, Jharkhand, India
P: +91-657-2421144

GURGAON Unit No. 202, 2nd Floor, 'A' Block, Iris Tech Park, Sector – 48 (Sohna Road), Gurgaon–122018, Haryana, India
P: +91-124-4838000

Indonesia:

PT. NSK INDONESIA

JAKARTA Summitmas II, 6th Floor, Jl. Jend Sudirman Kav. 61-62, Jakarta 12190, Indonesia
P: +62-21-252-3458 F: +62-21-252-3223

Korea:

NSK KOREA CO., LTD.

SEOUL Posco Center (West Wing) 9F, 440, Teheran-ro, Gangnam-gu, Seoul, 06194, Korea
P: +82-2-3287-0300 F: +82-2-3287-0345

Malaysia:

NSK BEARINGS (MALAYSIA) SDN. BHD.

SHAH ALAM ☆ No. 2, Jalan Pemaju, U1/15, Seksyen U1, Hicom Glenmarie Industrial Park, 40150 Shah Alam, Selangor, Malaysia
P: +60-3-7803-8859 F: +60-3-7806-5982

PRAI No.24, Jalan kikik, Taman Inderawasih, 13600 Prai, Penang, Malaysia
P: +60-4-3902275 F: +60-4-3991830

JOHOR BAHRU 88 Jalan Ros Merah 2/17, Taman Johor Jaya, 81100 Johor Bahru, Johor, Malaysia
P: +60-7-3546290 F: +60-7-3546291

IPOH No.10&10A, Jalan Industri Paloh, Kawasan Perindustrian Ringan Paloh, 30200 Ipoh, Perak,Malaysia
P: +60-5-2555000 F: +60-5-2553373

Philippines:

NSK REPRESENTATIVE OFFICE

MANILA 8th Floor The Salcedo Towers 169 H.V. Dela Costa St.,Salcedo Villege Makati City, Philippines 1227
P: +63-2-893-9543 F: +63-2-893-9173

Singapore:

NSK INTERNATIONAL (SINGAPORE) PTE LTD.

SINGAPORE 238A, Thomson Road, #24-01/05, Novena Square Tower A, Singapore 307684
P: +65-6496-8000 F: +65-6250-5845

NSK SINGAPORE (PRIVATE) LTD.

SINGAPORE 238A, Thomson Road, #24-01/05, Novena Square Tower A, Singapore 307684
P: +65-6496-8000 F: +65-6250-5845

Thailand:

NSK BEARINGS (THAILAND) CO.,LTD.

BANGKOK 26 Soi Onnuch 55/1 Pravet Subdistrict, Pravet District, Bangkok 10250, Thailand
P: +66-2320-2555 F: +66-2320-2826

Vietnam:

NSK VIETNAM CO., LTD.

HANOI Techno Center, Room 204-205, Thang Long Industrial Park, Dong Anh District, Hanoi, Vietnam
P: +84-24-3955-0159 F: +84-24-3955-0158

NSK REPRESENTATIVE OFFICE

HO CHI MINH CITY Unit 609, The Landmark Building, 5B Ton Duc Thang Street,District 1, Ho Chi Minh City, Vietnam
P: +84-28-3822-7907 F: +84-28-3822-7910

Worldwide Sales Offices

P: Phone F: Fax ☆: Head Office

●Europe

United Kingdom:

NSK EUROPE LTD. (EUROPEAN HEADQUARTERS)

MAIDENHEAD Belmont Place, Belmont Road, Maidenhead, Berkshire SL6 6TB, U.K.
P: +44-1628-509-800 F: +44-1628-509-808

NSK UK LTD.

NEWARK Northern Road, Newark, Nottinghamshire NG24 2JF, U.K.
P: +44-1636-605-123 F: +44-1636-605-000

France:

NSK FRANCE S.A.S.

PARIS Quartier de l'Europe, 2 Rue Georges Guynemer, 78283 Guyancourt, France
P: +33-1-30-57-39-39 F: +33-1-30-57-00-01

Germany:

NSK DEUTSCHLAND GMBH

DUSSELDORF ☆ Harkortstrasse 15, D-40880 Ratingen, Germany
P: +49-2102-4810 F: +49-2102-4812-290

STUTTGART Liebknechtstrasse 33, D-70565 Stuttgart-Vaihingen, Germany
P: +49-711-79082-0 F: +49-711-79082-289

WOLFSBURG Tischlerstrasse 3, D-38440 Wolfsburg, Germany
P: +49-5361-27647-10 F: +49-5361-27647-70

Italy:

NSK ITALIA S.P.A.

MILANO Via Garibaldi 215, Garbagnate Milanese (Milano) 20024, Italy
P: +39-299-5191 F: +39-299-025778

Netherlands:

NSK EUROPEAN DISTRIBUTION CENTRE B.V.

TILBURG Brakman 54, 5047 SW Tilburg, Netherlands
P: +31-13-4647647 F: +31-13-4641082

Poland:

NSK REPRESENTATIVE OFFICE

WARSAW Ul. Migdalowa 4/73, 02-796, Warsaw, Poland
P: +48-22-645-1525 F: +48-22-645-1529

Spain:

NSK SPAIN S.A.

BARCELONA C/Tarragona, 161 Cuerpo Bajo, 2a Planta, 08014, Barcelona, Spain
P: +34-93-289-2763 F: +34-93-433-5776

Turkey:

NSK RULMANLARI ORTA DOGU TIC. LTD. STI.

ISTANBUL Cevizli Mahallesi. D-100 Güney Yanyolu, Kuriş Kule İş Merkezi No:2 Kat:4, P.K.: 34846, Cevizli-Kartal-Istanbul, Turkey
P: +90-216-5000-675 F: +90-216-5000-676

United Arab Emirates:

NSK BEARINGS GULF TRADING CO.

DUBAI JAFZA View 19, Floor 24 Office LB192402/3, PO Box 262163, Downtown Jebel Ali, Dubai, U.A.E
P: +971-(0)4-804-8200 F: +971-(0)4-884-7227

●North and South America

United States of America:

NSK AMERICAS, INC. (AMERICAN HEADQUARTERS)

ANN ARBOR 4200 Goss Road, Ann Arbor, Michigan 48105, U.S.A.
P: +1-734-913-7500 F: +1-734-913-7511

NSK CORPORATION

ANN ARBOR 4200 Goss Road, Ann Arbor, Michigan 48105, U.S.A.
P: +1-734-913-7500 F: +1-734-913-7511

NSK PRECISION AMERICA, INC.

FRANKLIN ☆ 3450 Bearing Drive, Franklin, Indiana 46131, U.S.A.
P: +1-317-738-5000 F: +1-317-738-5050

SAN JOSE 780 Montague Expressway, Suite 505, San Jose, California, 95131, U.S.A.
P: +1-408-944-9400 F: +1-408-944-9405

NSK LATIN AMERICA, INC.

MIAMI 11601 NW 107 Street, Suite 200, Miami Florida, 33178, U.S.A.
P: +1-305-477-0605 F: +1-305-477-0377

Canada:

NSK CANADA INC.

TORONTO ☆ 317 Rutherford Road South, Brampton, Ontario, L6W 3R5, Canada
P: +1-888-603-7667 F: +1-905-890-1938

MONTREAL 2150-32E Avenue Lachine, Quebec, Canada H8T 3H7
P: +1-514-633-1220 F: +1-800-800-2788

Argentina:

NSK ARGENTINA SRL

BUENOS AIRES Garcia del Rio 2477 Piso 7 Oficina "A" (1429) Buenos Aires-Argentina
P: +54-11-4704-5100 F: +54-11-4704-0033

Brazil:

NSK BRASIL LTDA.

SUZANO ☆ Av. Vereador João Batista Fitipaldi, 66, Vila Maluf, Suzano-SP-Brazil-CEP 08685-000
P: +55-11-4744-2500

JOINVILLE Rua Blumenau, 178, sala 910, Centro, Joinville-SC-Brazil-CEP 89204-250
P: +55-47-3422-2239

Peru:

NSK PERU S.A.C.

LIMA Calle Teniente Enrique Palacios 360 Oficina 311 Miraflores, Lima, Peru
P: +51-493-4385

Mexico:

NSK RODAMIENTOS MEXICANA, S.A. DE C.V.

SILAO, GUANAJUATO Circuito Mexiamora Oriente No. 331, Parque Industrial Santa Fe I, Puerto Interior. Silao, Guanajuato, Mexico. C.P. 36275
P: +52-472-500-9500 F: +52-472-103-9403

<As of August 2021>

For the latest information, please refer to the NSK website.

www.nsk.com

Motion & Control

No. 33 June 2022

Published by NSK Ltd.

Eco-awareness and reliability in motion
NSK

NSK used environmentally friendly printing methods for this publication.

CAT. No. ETJ-0033 2022 X-6 Printed in Japan